

Investigations of high speed neutral particle injection into KSTAR plasmas

Thesis submitted for the degree of
Doctor of Philosophy

Department of Physics
Technical University of Denmark

Galina Avdeeva

November 14rd 2019

Investigations of high speed neutral particle injection into KSTAR plasmas

Supervisor: Prof. Volker Naulin

Technical University of Denmark

Co-supervisors: Dr. Anders Henry Nielsen

Technical University of Denmark

Prof. Wonho Choe

KAIST

Examiners: Dr. Tuomas Tala

Hans Pecseli

Chairman: Anders Andersen

Technical University of Denmark

Abstract

This thesis is devoted to the investigation of one of the fuelling methods, namely the supersonic molecular beam injection (SMBI). A maintenance of a high density level and a compensation of the particle losses, caused by the radial transport, are required to fulfil the ignition condition. Therefore, refuelling of plasma while a tokamak operates is essential for the realisation of a sustainable fusion reaction.

The overview of the experiments reveals the benefits of SMBI compared to the traditional gas puff injection (GP). In case of SMBI the plasma response on the injection is faster, penetration depth of neutrals is deeper and consequently the fuelling efficiency is higher. In addition, the suppression of edge localized modes (ELMs) and large amplitude fluctuations was observed in experiments with SMBI, but no consistent theory exists to explain this effect.

Calculations of the injection parameters of supersonic molecular beam corresponding to SMBI system on Korea Superconducting Tokamak Advanced Research (KSTAR) are performed for two operation regimes: with the working gas at the room temperature and the gas cooled under 105 K. The influence of SMBI on plasma depends on the operation regime is analysed based on the KSTAR experimental data.

The main focus of this thesis is the numerical investigation of the interactions of fusion plasma with the high speed molecular beam. Dynamical interactions of the molecules and atoms are implemented in a drift-fluid model, which describes the dynamics of the plasma at the outer mid-plane of a tokamak. The increase of the plasma density, decrease of the temperature and reduction of the fluctuation level of the plasma density fluctuations which were observed in experiments with SMBI, are reproduced in the numerical simulations. The dependency of those effects, as well as the fuelling efficiency, on the beam parameters is investigated and discussed in this work. The qualitative comparison of the numerical results with results of other models, with KSTAR experimental data and earlier experimental observations on other tokamaks is presented in this thesis.

Keywords: supersonic molecular beam injection (SMBI), Korea Superconducting Tokamak Advanced Research (KSTAR), plasma dynamics, drift-fluid model

Resumé

I denne afhandling undersøges 'supersonic molecular beam injection' (SMBI) som en af de mulige partikeltilførselsmetoder for tokamak plasmaer. Vedligeholdelse af en høj partikeltæthed, og kompenstation for partikeltab forårsaget af radiel transport, er nødvendigt for at opfylde betingelsen for antændelse. Derfor er en løbende genopfyldning af plasma i en tokamak essentiel, hvis vedvarende fusionsenergi skal realiseres.

En gennemgang af eksperimentelt opnåede resultater afslører fordelene ved SMBI frem for den traditionelle 'gas puff injection' (GPI) metode. Plasmaet reagerer hurtigere ved SMBI og de neutrale partikler penetrerer dybere ind i det indesluttede plasma, hvilket giver en højere partikeltilførselseffekt. Derudover er der i nogle eksperimenter observeret en dæmpende effekt på 'edge localized modes' (ELMs) og fluktuationer med høj amplitude som følge af SMBI, omend det teoretiske grundlag for denne effekt ikke er klarlagt.

Der er foretaget beregninger for injektionsparametrene for SMBI svarende til dem for 'Korean Superconducting Tokamak Advanced Research' (KSTAR) for to operationsregimer; ét hvor den neutrale gas er ved stuetemperatur, og ét hvor gassen er kølet ned til under 105 K. Der ef efterfølgende foretaget en analyse af hvorledes effekten af SMBI afhænger af det pågældende operationsregime baseret på eksperimentelle data fra KSTAR.

Afhandlingen hovedfokus er numeriske undersøgelser af vekselvirkningerne mellem fusionsplasmaet og partikelstrålen af hurtige molekyler. Dynamiske vekselvirkninger mellem plasmaet og neutrale molekyler og atomer er implementeret i en 'drift-fluid' model, som beskriver plasmadynamikken i det ydre midtplan af en tokamak. Forøgelsen af plasmatætheden og faldet i temperatur og fluktuationsniveauet for plasmatætheden, som er alle er observeret i eksperimenter med SMBI, er reproduceret i numeriske simuleringer. Hvorledes disse effekter, samt partikeltilførselseffekten, afhænger af partikelstrålens parametre undersøges og diskuteres. Derudover præsenteres en kvalitativ sammenligning af de numeriske resultater med resultaterne fra andre modeller, samt med eksperimentelle resultater fra KSTAR og tidligere eksperimentelle resultater fra andre tokamakker.

Contents

1	Introduction	1
1.1	Tokamak	1
1.2	Particle transport in tokamak	2
1.3	Plasma fuelling challenges	3
1.4	Fuelling methods	5
2	Previous research on the high speed neutral particle injection	7
2.1	Overview of experiments with high speed neutral particle injection	7
2.2	Modelling of SMBI	15
2.3	Thesis goals and outline of the thesis	17
3	SMBI on KSTAR	19
3.1	Characteristics of a supersonic beam	19
3.1.1	Laval nozzle	19
3.1.2	Exit nozzle velocity and mass flux	20
3.1.3	Isentropic flow equations	21
3.2	SMBI system on KSTAR	22
3.2.1	Calculations of the SMB parameters	22
3.2.2	Influence of SMBI on KSTAR plasma	25
4	Numerical simulation of plasma	32
4.1	Plasma transport equations	32
4.2	Drift-ordering and fluid motion	34
4.3	Coupling of HESEL and SMBI models	35
5	Investigation of SMBI by numerical simulations	38
5.1	Introduction to the numerical data of HESEL - SMBI simulations	38
5.1.1	HESEL data	38
5.1.2	SMBI data	44
5.1.3	Outline of the result section	52
5.2	Influence of neutral sources on the SMB penetration in self-consistent simulations	52
5.2.1	Investigation of the "self-shielding" effect in simulations with plasma dynamics	52
5.2.2	Neutral source terms in a plasma drift-fluid model	58
5.3	Scan of the beam parameters	71
5.3.1	Scan of the beam intensity	72
5.3.2	Scan of the beam velocity	82
5.3.3	Scan of the beam width	91

5.4	Influence of SMBI on a plasma turbulence transport	100
5.4.1	Dependence on a beam intensity	100
5.4.2	Dependence on the beam width	108
5.4.3	Dependence on the beam velocity	110
5.5	Influence of plasma fluctuations on SMB penetration	113
6	Conclusions	117

Chapter 1

Introduction

This chapter provides an introduction to fusion energy and thermonuclear plasma. Selected topics are briefly discussed to understand the motivation of the research presented in the thesis.

1.1 Tokamak

Fusion research is focusing on the producing the sustainable energy based on the nuclear reactions. Nuclear fusion reactions occur when two or more atomic nuclei are come close together and fuse into heavier nuclei. The difference in mass is released in the energy. In order to induce the fusion reaction atomic nuclei should overcome the Coulomb barrier. This can be achieved by heating them to high temperatures. Heated to fusion temperatures of 10 -20 keV [1], atomic nuclei are disassociate. The mixture of ions and electrons with a high degree of ionization is known as a plasma. The behavior of plasma is governed by collective effects due to long range Coulomb interactions between charge particles. Unlike electrically neutral atoms, the plasma is electrically conductive, and can be manipulated by electrical and magnetic fields. This principle is used in a tokamak, the device designed to confine the plasma and produce thermonuclear energy. A schematic view of the main components of tokamak is shown on Fig.1.1.

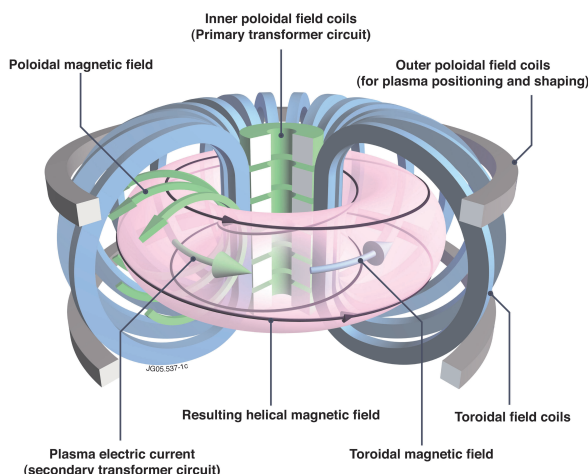


Figure 1.1: An illustration of the main components of tokamak. Figure are taken from [2].

A toroidal magnetic field in a tokamak is produced by a current in external toroidal coils. The maximum magnitude of the magnetic field and operation time is limited by

mechanical and heat loads in the coils. The strength of the magnetic field is inversely proportional to the distance from the center of the torus. Therefore, the maximum toroidal field appears at the inboard side of the tokamak. For a stable plasma configuration it is also necessary to have a poloidal magnetic field, otherwise charge particles will drift across the field and heat the wall of the torus. The poloidal magnetic field is produced by a current flowing in the toroidal direction in the plasma. The plasma current is driven by a toroidal electric field induced by the transformer action of a center solenoid [1]. The poloidal magnetic field is typically an order of magnitude smaller than the toroidal field. The resulting magnetic field has a helical trajectory around the torus and forms the nested closed surfaces (magnetic flux surfaces) as shown on Fig. 1.2a. Such configuration can be generated only within a restricted volume with a boundary determined by the Last Closed Flux Surface (LCFS) or separatrix. In order to prevent a contamination of the plasma by impurities and subsequent radiation losses, solid surfaces are moved some distance from the LCFS. Such configuration with open magnetic field lines directed toward the divertor target is shown in Fig. 1.2b. The region between the solid surfaces (wall of the vacuum vessel and divertor plates) and separatrix is referred as the Scrape-Off Layer (SOL).

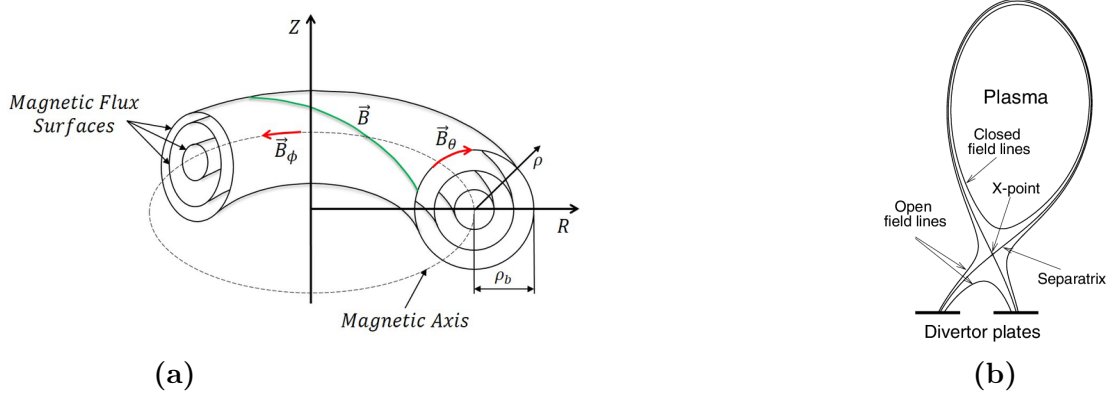


Figure 1.2: (a) Toroidal magnetic flux surfaces in a tokamak plasma. Figure are taken from [3]. (b) A schematic poloidal view of a magnetic configuration in a single-null divertor tokamak. Figure are taken from [4]

The requirement for the plasma burn to be self-sustained is given by the Lawson criterion

$$nT\tau_E > 3 \times 10^{21} \text{ m}^{-3}\text{keVs}, \quad (1.1)$$

where n is the plasma density, T is the plasma temperature and τ_E is the energy confinement time. This is a necessary, but not sufficient, requirement that the power produced by the reactor would be able to supply the applied heating [1]. **An optimization of the plasma parameters is essential to achieve a high performance plasma.** An efficiency of applied external particle and energy sources is determined by the particle and energy transport in tokamak.

1.2 Particle transport in tokamak

Charged particle motion in electric and magnetic fields is governed by the Lorentz force:

$$m \frac{d\vec{v}}{dt} = q(\vec{E} + \vec{v} \times \vec{B}), \quad (1.2)$$

where m , \vec{v} and q are the mass, velocity and charge of the particle respectively, \vec{E} and \vec{B} are the electric and magnetic field. A motion in a constant magnetic field consists of a circular cyclotron motion around the magnetic field line (gyromotion) and a motion of the center of the gyromotion (guiding center) along the magnetic field line. In a tokamak the guiding center undergoes slow spatial drifts in addition to the gyromotion. The additional drifts result from the inhomogeneity and curvature of magnetic field lines and the existence of electric fields. A single particle in tokamak is ideally confined around the closed field line. Due to poloidal variation of magnetic field a particle with a small velocity parallel to the magnetic field is trapped on the outer side of a tokamak. The trapped particle trajectory projected on the poloidal plane is shown on Fig. 1.3. A particle with sufficiently high parallel velocity does not get trapped and continually circulates around the torus. The poloidal projection of trajectory of such passing particle is shown on Fig. 1.3. Different particles in a tokamak interact

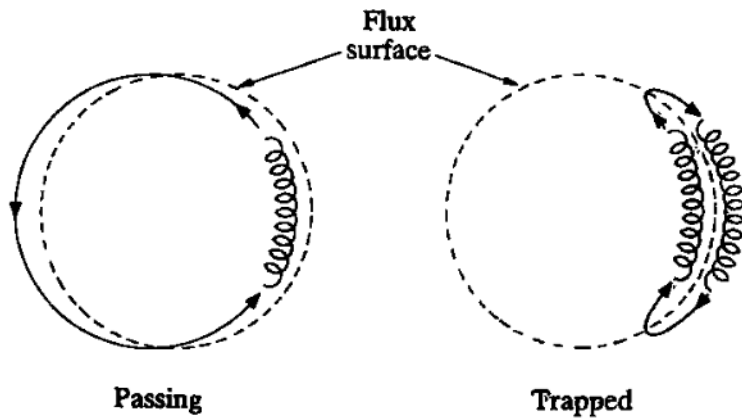


Figure 1.3: A sketch of a projection of particle trajectories on the poloidal plane of tokamak.
Figure are taken from [1].

through the collisions and move from one magnetic surface to another. This results in a diffusion radial transport. Due to specific trajectories of particles in tokamak, the collision cross section is higher and the diffusion process is called neoclassical, as it characterised by the higher diffusion coefficient compared to classical one.

If the plasma parameters are inhomogeneous instabilities can develop and drive fluctuations, which lead to a radial turbulent flux of particles and energy. Since the turbulent flux is much larger than the diffusion, the turbulence transport is the main mechanism of the particle and energy losses across the LCFS. Charged particles, which crossed the separatrix and left the confined region, move along open magnetic field lines to the divertor plates.

Particle losses caused by the radial transport should be compensated to fulfil the Lawson criterion. Thus, the refuelling of plasma while a tokamak operates is required.

1.3 Plasma fuelling challenges

Neutral particles are injected in plasma for fuelling purposes, as unlike the charge particles they do not affected by the electromagnetic field and do not follow the open

magnetic field lines in the SOL region. However, neutrals injected into fusion plasma are a subject to interactions with plasma particles and subsequent atomic processes. The rate coefficient $\langle\sigma v\rangle$ determines the efficiency of the corresponding atomic process. The rate coefficients for a number of common reactions between neutrals and plasma particles in fusion plasma are shown in Fig. 1.4. As seen from this figure, rate coefficients strongly depend on the energy of the thermal particles or in other words on the electron temperature of plasma.

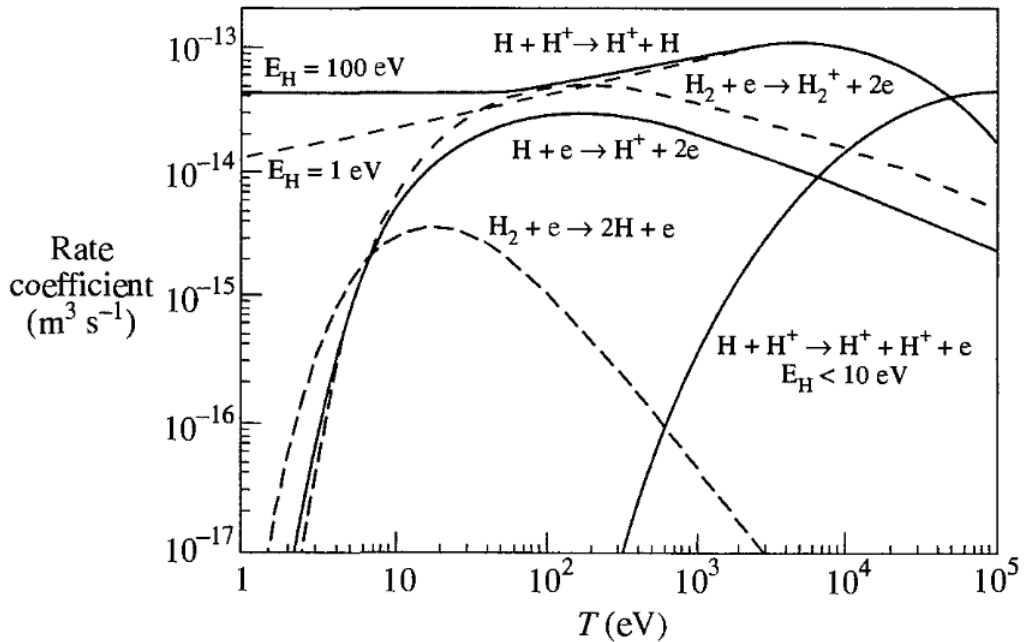


Figure 1.4: Rate coefficients $\langle\sigma v\rangle$ for hydrogen atoms and molecules for a number of common reactions in fusion plasma. Figure are taken from [1].

In plasma with high temperature and density **neutrals are ionized before they reach the confined region and ions are experience a parallel motion along the open magnetic filed lines and be absorbed on the divertor.** Large gas puffing therefore requires the high capacity pumping system.

If the plasma density and temperature profiles are known, in principle, it is possible to determine the penetration of neutral particles in plasma. However, ionization processes immediately modify the plasma density and temperature. The plasma temperature in the SOL region lies in the range of several eV to several tens of eV and as seen in Fig. 1.4 even a small variation in this range can lead to the significant change of the rate coefficient. In addition, the intermittent plasma transport, which is characterized by high amplitude fluctuations of density ant temperature in the SOL region, affect the penetration of neutral particles by irregular enchanting the atomic processes. This indicates the **necessity of a model with a self-consistent description of plasma-neutral interactions, include the plasma dynamics, to estimate the radial deposition profile of injected neutral particles.** Such approach is applied and discussed in the thesis.

An another issue in the plasma fuelling is the density limit. **An empirical limit**

to the maximum density is given by the Greenwald limit

$$n_{e,20} \leq \frac{I_p}{\pi a^2}, \quad (1.3)$$

where $n_{e,20}$ is the electron density in units of $10^{20} m^{-3}$, I_p is the plasma current in MA, and a is the minor radius of tokamak in m. This limit dictates the maximum density which can be achieved in tokamak. Exceeding of the density limit usually leads to the breakdown of the discharge. However, this is the boundary density limit and it is possible to extend this limit by operation with peaked density profile [5–8]. The physical mechanism of the density limit has not been understood, but the strong edge cooling and turbulence transport are possibly cause of the density limit.

In addition to the Greenwald density limit the **MHD stability imposed the operation limit on the density at the periphery of plasma**. The ballooning parameter [9]

$$\alpha_{sep} = \frac{R q_{cyl}^2}{B_{tor}^2 / 2\mu_0 \langle \lambda_p \rangle} \frac{p_{sep}}{\langle \lambda_p \rangle}, \quad (1.4)$$

where μ_0 is the magnetic vacuum permeability, p_{sep} is the plasma pressure, $\langle \lambda_p \rangle$ is the poloidal averaged pressure decay length at the separatrix position, B_{tor} is toroidal magnetic field, q_{cyl} is the cylindrical safety factor, I_p is the plasma current and R is the major radius. Increase of the ballooning parameter up to 2 - 2.5 leads to the confinement degradation. As shown in [9] this limit can be extended by increase the ration of the average plasma density to the density on separatrix. This can be accomplish by the core plasma fuelling.

From all above it follows that the core fuelling and peaking density profiles are desirable conditions for fuelling methods.

1.4 Fuelling methods

The main and commonly used fuelling method is called the **gas puffing (GP)**, where the gas is injected into the plasma through fast piezoelectric valves. Molecules are injected under room temperature and penetrate in all directions according to the diffusion process. Consequently, the penetration time is longer compared to the ionization time and likely neutrals will be ionized faster than they pass the distance equal to the width of the SOL region. As the main fraction of the injected neutrals is ionized in the SOL, charge-exchange processes play an essential role for this fuelling method. Atoms, created in charge-exchange processes, have a higher energy and might penetrate deeper into the confined region. The simplicity makes GP the main fuelling method on magnetic confinement devices, although the efficiency, which is the ratio of plasma density increment to the number of injected particles, usually does not exceed 20-30 % [10, 11]. Moreover this method is not convenient for the plasma density feedback control system as the plasma response time on the injection is a several tens of ms.

A high efficiency fuelling method is **pellet injection (PI)** [12], where a small, high density, cryogenic pellet is injected with a velocity around 500-1000 m/s. The shielding effect of a dense gas shell which surrounds the frozen pellet protects the core of the pellet from interaction with plasma particles. Ionization of the pellet in this case happens slower than the penetration of pellet into the plasma and the main part of injected neutrals is ionized inside the separatrix. The main restriction for this method is the

complexity and high cost of the pellet injection system, while high fuelling efficiency above 70 % was demonstrated in experiments.

Neutral beam injection (NBI) allows the injection of particles with an energy of tens keV [13]. Owing to high energy neutral particles reached the confined region and heat the plasma through the collisions with charged particles. Since the injected neutral flux is several orders lower than in case of GP or PI this method can not provide a sufficient density and is not considered as an efficient fuelling method.

Another fuelling method is **supersonic molecular beam injection SMBI**) [14]. This method is similar to GP injection apart from the using the Laval nozzle for acceleration of molecules to supersonic speeds. The high direct velocity provides the fast penetration of the high dense, narrowly localized neutral beam across the LCFS. The fuelling efficiency of SMBI lies in the intermediate position between GP and PI [11, 15–17], but technically this method is much simpler compared to PI. This method was widely used in different machines [15, 18–20], and mentioned as MBI, SPGI or SMBI. The latest notation will be used in this thesis also as a synonym to "high speed neutral particle injection".

The simplicity of the system and at the same time relatively high efficiency draws attention to SMBI as promising method for plasma fuelling. This motivated the investigation of SMBI in this work aiming to better understand which injection parameters provide the higher fuelling efficiency. The investigation starts from the literature review to highlight the main features of SMBI observed in experiments and the level of understanding of revealed effects.

Chapter 2

Previous research on the high speed neutral particle injection

This chapter gives an overview of the main results revealed in experiments with SMBI on different machines. The interpretation of the observed effects and the corresponding simulation results given in the source are presented as well. The two numerical model developed especially for simulation of SMBI which self-consistently describe the plasma-supersonic molecular beam interactions are particularly considered after review of experimental results. The literature review leads to the formulation of the thesis goals and the outline of the thesis finishes this chapter.

2.1 Overview of experiments with high speed neutral particle injection

The idea to use an intense hydrogen clusters, injected with the velocity about 500 m/s for fuelling of the thermonuclear plasma was proposed in 1972 by R. Klingelhofer and H.O.Moser [21]. The first demonstration of the pulsed high speed molecular beam injection was on **HL-1** tokamak in 1993 [22], where the ramp-up rate of the electron density at steady state was more than double the achieved with GP on HL-1. The penetration depth of deuterium molecular beam was around two times higher compared to GP.

HL-1M

As a new method of the gas fuelling SMBI was applied on HL-1M tokamak [23]. In order to reduce the injected gas reabsorption in the first wall, helium was selected as the working gas for SMBI and the beam was injected into the low target density ($\langle n_e \rangle = 4 \cdot 10^{18} \text{ m}^{-3}$) hydrogen plasma. The injection parameters were following: injection time 100 ms, injection velocity around 350 m/s, the working pressure 10^5 Pa, which corresponded to around $6 \cdot 10^{19}$ of injected molecules. A peaking electron density profile was observed during SMBI and the averaged plasma density increased from $4 \cdot 10^{18} \text{ m}^{-3}$ to $5.6 \cdot 10^{19} \text{ m}^{-3}$ [23]. In addition to the variations of the plasma density and temperature profiles, the enhanced energy confinement time was measured, which is over 30% longer than that of the GP results under the same operational conditions.

According to the work [23] the interpretation of the deep beam penetration is based on the collective motion of particles in a high density beam. Particles inside the beam

are protected from the incoming electron collisions by the surrounding neutrals and cold ionized particles. This effect was called the "beam effect" and this is analogy of the shielding effect for pellet injection.

Improvements of the beam features, like a reduction of the nozzle diameter and increase of the working pressure enhanced the neutral flux on HL-1M tokamak up to the cluster formation parameters [6]. The effect of the condensation of an expanding nozzle flow was observed under the low gas temperature and pressure. The **condensed molecular beams or cluster beams** are made up of clusters, i.e., microdroplets or -crystals, where the atoms or molecules are held together by Van der Waals forces [24]. Cluster beams are characterized by much higher mass fluxes and by highly uniform particle velocities [25]. Consequently such beam should provide a deeper penetration of neutrals inside the fusion plasma and behaves as pellets. The H_α emission register at the HL-1M tokamak at the beam injection port appeared as many separate peaks. This is considered as an indication of interactions of hydrogen clusters with plasma. The hydrogen particles penetrated up to 15 cm inside the plasma and ($\langle n_e \rangle = 8.2 \cdot 10^{19} m^{-3}$) the highest maximum density ever achieved on that tokamak was obtained [6]. The changes of Mach number of the parallel flow (M), the poloidal flow velocity (V_{pol}) and the electric field (E_r) induced by SMBI were measured on HL-1M. As seen in Fig. 2.1 the influence of SMBI on plasma, in terms of modification of plasma parameters, lies in between the gas puffing and pellet injection. In work [6] it is claimed, that the increase of the poloidal rotation velocity might decrease the level of the turbulence fluctuations, and the plasma confinement would be improved.

The strong particle convection or inward pinch after SMBI was observed on HL-1M in 2012 [26]. The inward particle propagation was revealed by comparing the the line averaged plasma density on the different channels of interferometer (Fig. 2.2). At the edge-most channels ($Z = -17.5$ cm and $Z = 24.5$ cm), the line-integrated density began to decrease several ms right after the sharp increasing phase. The density at the innermost channels ($Z = \pm 3.5$ cm) continuously increased for about 30 ms and then decreased. Different post-SMBI behaviour between edge and core density indicates that the inward particle pinch exists during the post-fuel phase of SMBI. The pinch velocity of 6 m/s was estimated by the phase delay. Experiments with ECRH heating showed that the inward transport is driven by the enhancement of the electron temperature gradient [26].

HT-7

The peaking density profile and the evidence of the center gas fuelling with SMBI injection were obtained on the superconducting tokamak HT-7 [5]. The penetration depth of the beam particles was around 12 cm. The fuelling efficiency of SMBI was 40-50 %, while for GP this value was 20-30 % and 70-80 % for PI [5].

Tore Supra

On the Tore Supra the first supersonic pulse gas injection (mentioned as SPGI) was performed from the high field side of the tokamak. Around 10^{20} atoms were injected within 1 ms into ohmic plasma with averaged density $\langle n_e \rangle = 1.7 \cdot 10^{19} m^{-3}$. Higher plasma density response on SMBI compared to GP with the same injection rate was demonstrated and the fuelling efficiency of SMBI was 3-4 times higher than than for

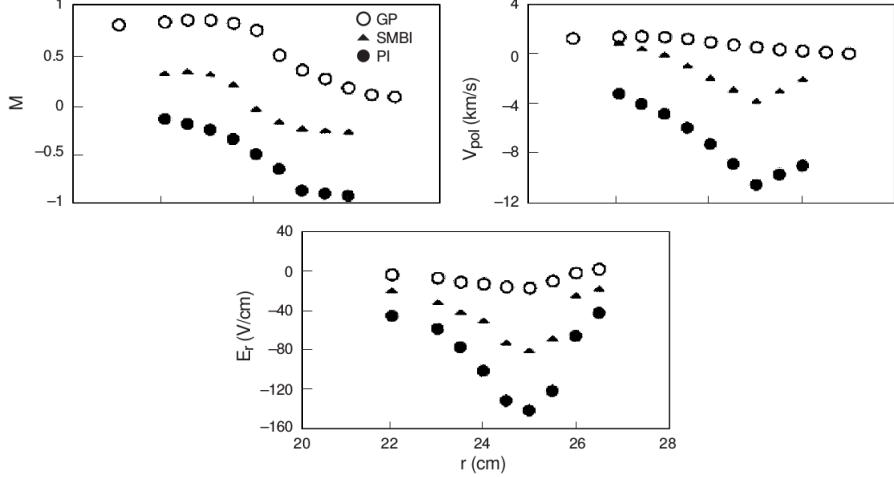


Figure 2.1: Radial profiles of Mach number of the parallel flow (M), the poloidal flow velocity (V_{pol}) and the electric field (E_r) during GP, SMBI and PI on HL-1M. Figures are taken from [6].

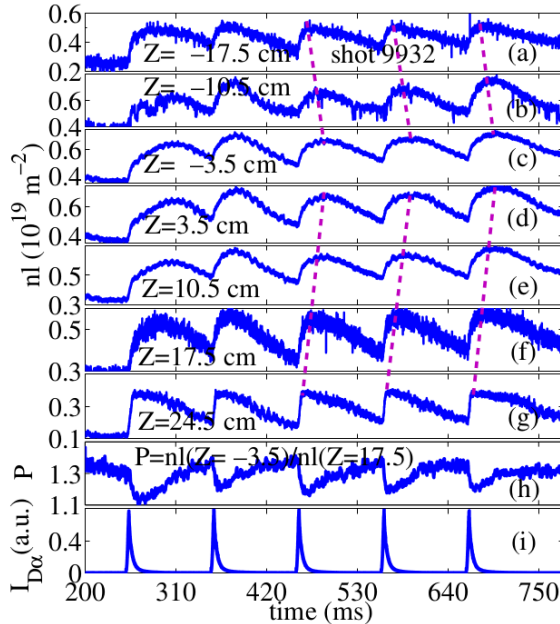


Figure 2.2: Phase delay of the line-integrated plasma density on different interferometer channels and the D_α monitoring of the fueling on HL-1M. $Z = 24.5\text{cm}$ and $Z = -17.5\text{cm}$ are the edge-most channels, $Z = \pm 3.5$ are the innermost channels. Figure is taken from [26].

traditional GP [18]. As seen from Fig. 2.3 the fuelling efficiency decreases with increase of the averaged plasma density. No clear dependency of the fuelling efficiency as function of the distance between nozzle and plasma surface was observed. The slight increase of the fuelling efficiency with increase of the molecular beam intensity was shown in [18].

The 1D diffusion model [18] with neutral code EIRENE was used for simulation of SMBI on Tore Supra. Results showed (Fig. 2.4) that the deposition of neutrals remained peripheral although the penetration depth of neutrals increased on the time of the maximum SOL cooling. The high fuelling efficiency of SMBI was explained by

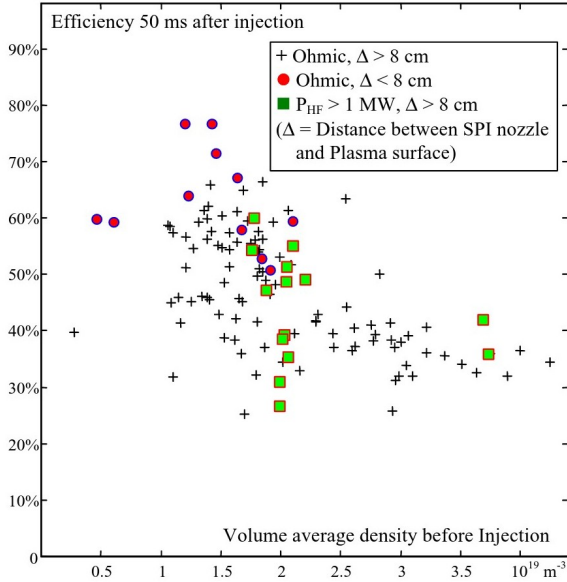


Figure 2.3: Fuelling efficiency of SMBI as a function of the density on Tore Supra. Figure is taken from [10].

the reduction of the plasma temperature and consequently increase of a probability of edge ions to diffuse radially inward and fuel the core. The plasma temperature and the parallel particle flux compared before and after SMBI are illustrated in Fig. 2.4.

The later experiments on Tore Supra illuminated additional effects observed after SMBI. The relaxation time of the plasma density after injection was around 10 times faster in the SOL region than in the edge [27]. It was explained by the different mechanisms of the particle transport in two regions. In the SOL region transport is given by the parallel flow of the plasma to limiter, while time scale in the edge is slower as it is defined by the diffusion time. The maximum of plasma density change compared to the level before injection was proportional to the amount of injected gas. Plasma density increased more with injection of the bigger amount of neutrals in those experiments. The decrease of the plasma temperature was about 40-50 % and did not depend on the injected gas amount. The values of temperature at the SOL region fell to 5-10 eV [27].

ASDEX Upgrade

SMBI identical to the Tore Supra was build for ASDEX Upgrade. Due to restrained space some modification was performed leading to somewhat reduced operational parameters [16]. Around $7 \cdot 10^{19}$ atoms were injected during 1-2 ms with velocity of 1.8 km/s. Fuelling efficiency was about 30 % in the low density L-mode with ELM-III and around 15 % in the high density H-mode with ELM-I [16]. Temperature drop observed on ASDEX Upgrade was smaller than a type-I ELM perturbations. Compared to the results from the Tore Supra the effect of SMBI on plasma on the ASDEX Upgrade is much weaker. The reason can be in smaller amount of injected particles compared to plasma amount, which was 10% on the ASDEX Upgrade and 50 % on the Tore Supra [16].

The possibility of using SMBI for pacing of ELM-I in H-mode plasma was investigated on the ASDEX Upgrade in 2005 [28]. Although no prompt (< 0.5 ms) ELM

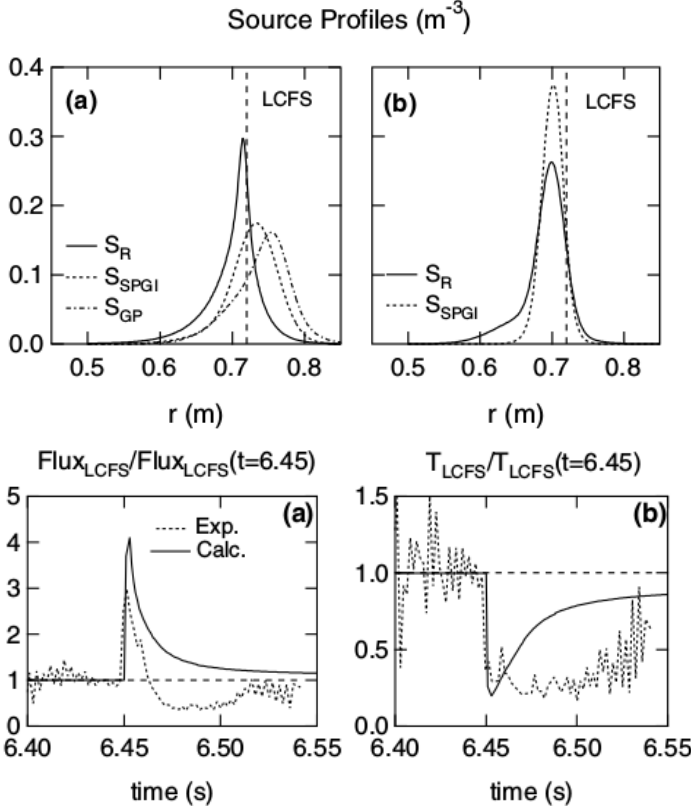


Figure 2.4: Top: source normalized profiles obtained by modeling on Tore Supra in the pre-injection conditions (a) and time of maximum SOL cooling (b). Bottom: ratio of the parallel particle flux (a) and the SOL temperature at the LCFS (b) during and before SMBI.

Figures are taken from [18].

triggering was achieved, the evidence of the delayed effect in the form of an inverse correlation of the gas pulse amplitude with the time interval between the gas pulse and the next ELM was observed. This delay effect was explained by increased pedestal pressure beyond the level obtained at this time after an intrinsic ELM and slow, approximately antisymmetric pedestal profile modification by SMBI [28]. Though the local transient efficiency (measured as the maximum of the density increment) of SMBI was around 50 % no significant impact of SMBI on the global discharge performance was observed. The fast particle loss a few ms after injection indicates that neutrals deposited outside of the separatrix. In case of the neutrals penetration inside the edge region the relaxation time of the plasma density after terminations of SMBI should be longer. Modelling and experimental results indicated that SMBI induced strong perturbations to the plasma but they are located too far out to affect on the H-mode pedestal. Comparison with pellet injection experiments lead to the conclusion that the radial position of the applied perturbations is a key parameter for ELM destabilization. ELMs can be easily triggered by strong perturbations near the pedestal top, but not by similar perturbations in the separatrix vicinity. Stopping of the beam at the LCFS is a result of so called "**self-shielding effect**" [28] which lies in the fact that the local high density plasmoid is formed in front of the beam on a microsecond time scale and effectively blocks further beam penetration. Simulations showed a pronounced density peak just outside the separatrix (Fig. 2.5), while the temperature profiles especially inside the separatrix are rather similar to the unperturbed case. Steep edge density profiles measured

by the lithium beam diagnostics (Fig. 2.6) supported this self-shielding hypothesis. Li-beam diagnostic on ASDEX located about 1.5 m away from SMBI in the toroidal direction, therefore, clearly missed the primary spot of fuelling, but should "see" the upper end of the halo region (reflected neutrals which returned to the plasma after few wall interactions with a time-of-flight delay in order of $100 \mu\text{s}$) [28].

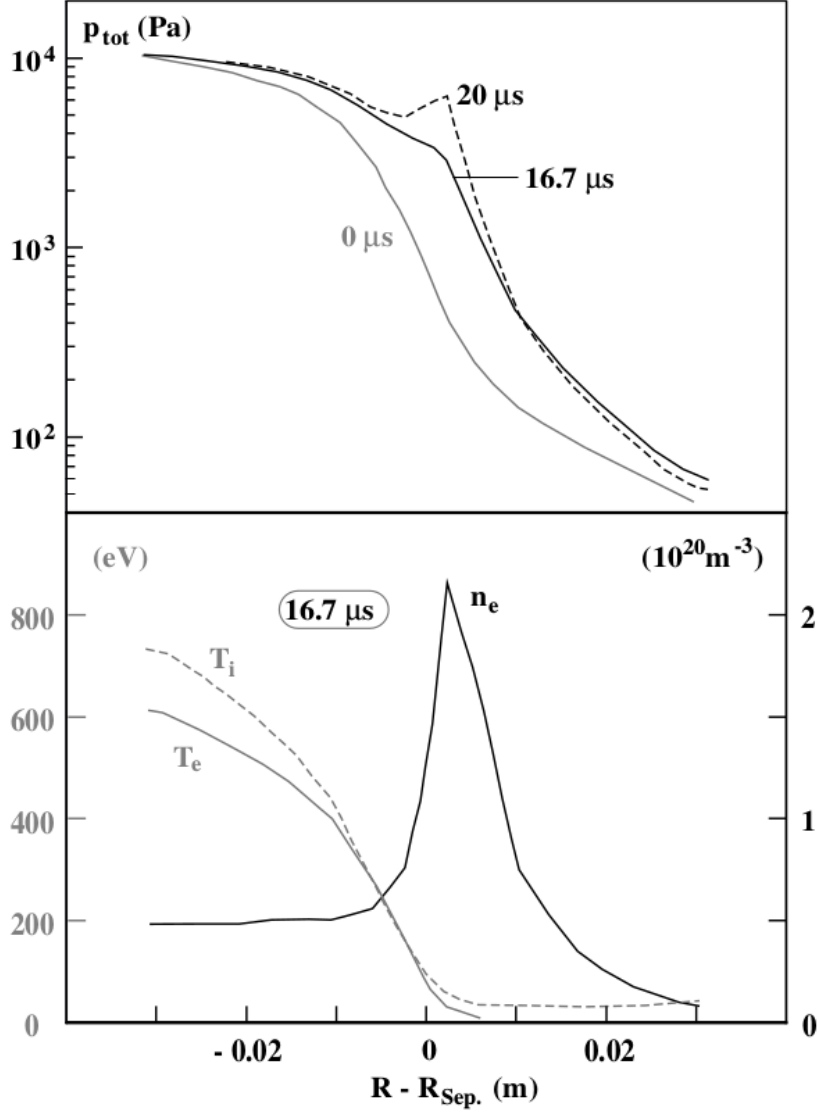


Figure 2.5: Simulation results on ASDEX Upgrade demonstrating the pronounced density peak due to ionization of injected molecules. Figure is taken from [?]

KSTAR and HL-2A

The signatures of ELM mitigation by SMBI, namely the ELM frequency increase and ELM amplitude decrease, were observed in the experiments on HL-2A and KSTAR tokamaks [29]. The influence of 4 ms SMBI pulses with the gas pressure of 2 MPa on HL-2A and 8 ms pulses with the gas pressure of 1 MPa on KSTAR were compared in terms of the influence on the ELM frequency. The deposition of neutrals within the pedestal in H-mode discharges was verified in both machines. The increase in ELM

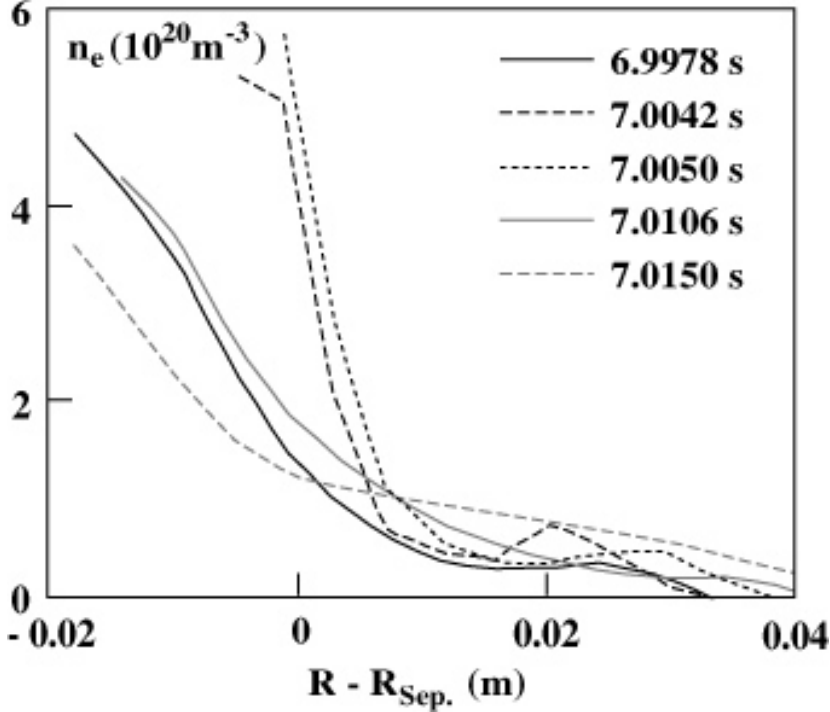


Figure 2.6: The radial electron edge density profiles measured by the Li-beam diagnostics on ASDEX Upgrade. Averaged over 400 μs data are taken at different time relative to the gas pulse 6.9978 s - before injection, 7.0042 s - middle of injection, 7.0050 s - end of injection, 7.0106 s and 7.0150 s - after injection. Figure is taken from [28]

frequency and decrease in the energy loss per ELM were achieved on both tokamaks as seen on the D_α signal in Fig. 2.7. The time interval from the D_α amplitude decrease or disappearance to the first D_α signal recovery is denoted as SMBI influence time τ_I . This time relates with SMBI pulse duration and working pressure. No mitigation effect was observed on HL-2A tokamak for the shorter SMBI pulses with lower working pressure. This indicates the existence of the critical minimum beam density when the ELM mitigation effect appears. Plasma parameters showed the following response on the SMBI: the density gradient relaxation following by the SMBI (Fig. 2.7), the decrease of the core toroidal rotation after injection, the decrease of the low-frequency content in the edge density fluctuations [29]. According to [29] the change in the frequency content suggests that ELM mitigation could result from an increase in higher frequency fluctuations and transport events in the pedestal. A simple phenomenological model, using a bi-stable cellular automata model, was used to elucidate the physics of influence of SMBI on ELMs. The trend indicated by this simplified model suggested that shallow SMBI deposition into the pedestal can mitigate ELMs by reducing the population of large avalanche transport events, while increasing the number of smaller one. SMBI does this by stimulating the localized fluctuations around the deposition point, "break up" large avalanches and convert them to smaller ones [29]. The importance of the understanding the relation between the turbulence and particle transport during SMBI was highlighted as the future research topic essential for understanding of the particle transport during the ELM mitigation phase.

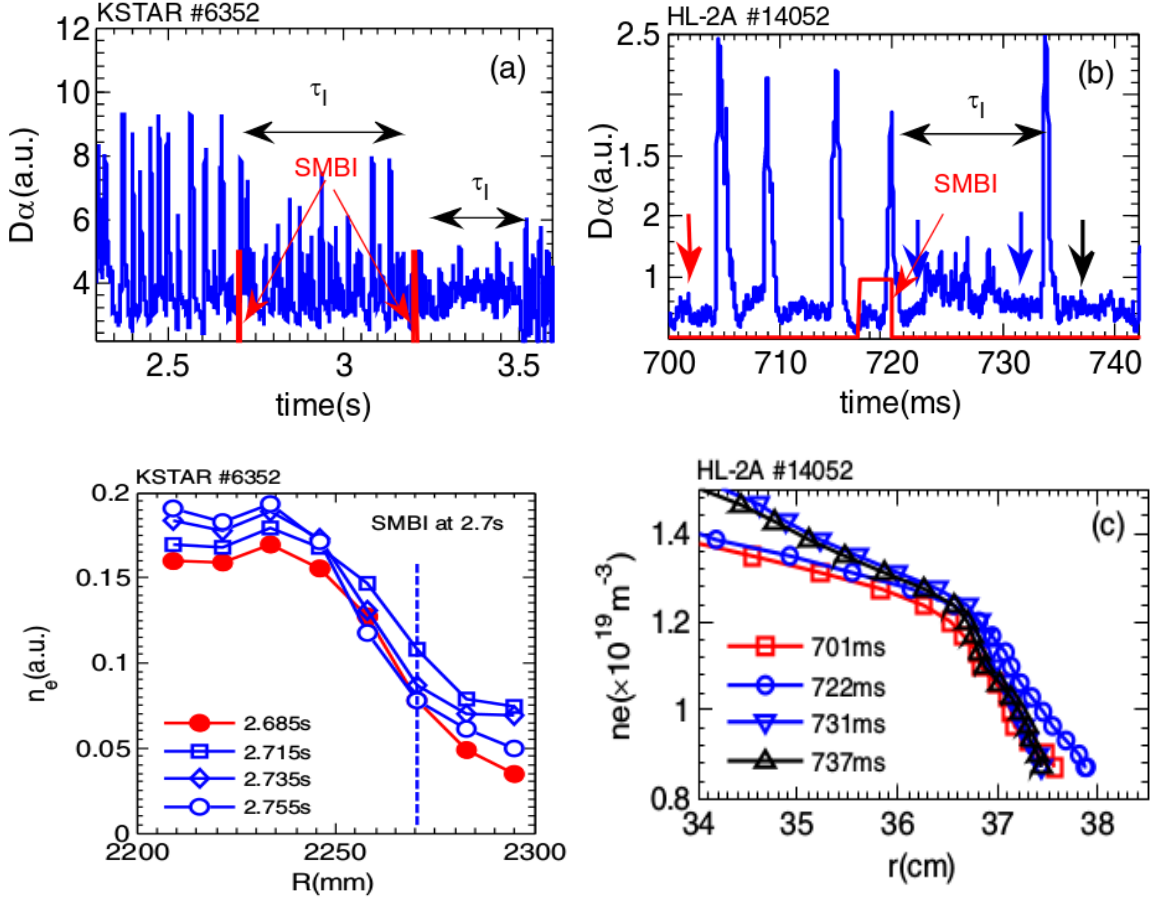


Figure 2.7: The top row shows the D_{α} emission during ELM mitigation by SMBI. Bottom row shows the plasma density profiles measured on KSTAR and HL-2A. Figure is taken from [29]

HL-2A

Comparison of SMBI from the high field side (HFS) and low field side (LFS) was performed on the HL-2A tokamak [20]. The experimental conditions were similar to the Tore Supra, where the density of SMBI is higher for HFS compared to LFS injection. The fuelling efficiency was around 35-55 % for LFS injection in limiter discharges and is around 40-50 % for HFS injection in divertor discharges [20]. The higher fuelling efficiency from HFS was observed in both ohmic and ECRF heated plasmas. Experiments on limiter and divertor configurations demonstrated noticeably higher efficiency on limiter configuration compare to divertor. This relates with high parallel losses of particles in divertor configuration [20]. Therefore the lower fuelling efficiency in the experiments with divertor configuration might indicate that the deposition of the injected neutrals is in the separatrix vicinity.

The suppression of the convection intermittent transport by SMBI is reported in [30]. The amplitude and the velocity of large filaments decreased after SMBI in experiments on HL-2A tokamak. The SMBI pulses duration of 0.6 ms with gas pressure of 4 MPa and temperature 108 K were injected from the LFS. The D_α emission indicated the maximum penetration depth of neutrals around 6 cm inside the LCFS, while the maximum of emission intensity is around 1 cm inside the LCFS. Filamentary

events were measured by the mid-plane probe array located near LCFS. Measurements indicated that when the amplitude threshold is less than 2.8σ (where σ is the standard deviation of the plasma density fluctuations), the filament burst rate after SMBI is bigger than the rate before SMBI, and when the amplitude threshold is greater than 2.8σ , the relation reverses [30]. Therefore the large amplitude filaments are suppressed by SMBI while the number of the small ones is increased. The filament radial velocity decreases by around 50 % after SMBI. A reduction of the correlation length between the midplane and divertor was also observed, indicating a role of electron-ion collisionality on the filament parallel current in the ELM mitigation time [30]. The transient particle and energy fluxes were reduced by 40-50 % and 50-60% respectively. These observations indicate that SMBI might be an effective method to reduce the intermittent convective transport.

EAST

On EAST and KSTAR SMBI is implemented in a feedback plasma density control system. Experiments on EAST [31] proved that SMBI is more promptly in the feedback control plasma experiments. Gas input was decreased about 30 % and the wall retention was reduced by 40% compared to GP feedback experiments. SMBI is the main fuelling method on EAST tokamak allowing obtaining the long pulse discharges. On KSTAR SMBI is used for the plasma density control in H-mode where the traditional GP is ineffective.

2.2 Modelling of SMBI

In addition to the simulation results already mentioned above two additional models of the SMBI are discussed here. Analysis of literature shown that only these two models have been developed especially for simulation of SMBI in fusion plasma and aimed to capture the main features of supersonic molecular beam.

trans-neut module of the BOUT++ code

The first is the *trans-neut* module of the BOUT++ code as it is mentioned in the source [32]. This 3D model couples plasma density, heat, and momentum transport equations together with neutral density and momentum transport equations for both molecules and atoms. Plasma neutral interactions include dissociation, ionization, recombination and charge-exchange reactions. Particle recycling is included in the model as well. Plasma dynamics are not included in this code. Simulations show the increase of plasma density and the decrease of the temperature during the SMBI (Fig.2.8).

The local increase of the plasma density leads to the decrease of the neutral penetration depth and backward beam penetration due to increase of dissociation and ionization rates (Fig.2.9) [32]. The investigation of the transport in the poloidal direction shows the propagation of plasma density blob (source) and ion temperature holes (sink) in upward and downward directions, while the electron temperature holes keep at the same location as no electron convection included. Various questions regarding SMBI were studied by using this code.

Simulations of the effect of density and temperature profiles on SMBI [33] suggested that SMBI is blocked by high density and temperature core plasma. The high plasma

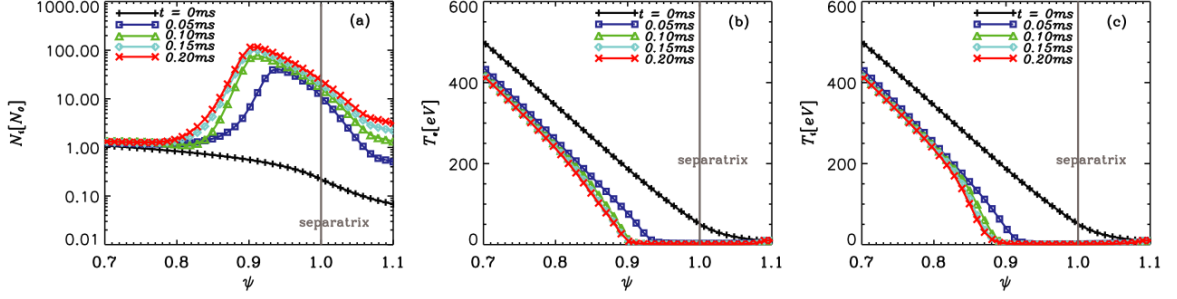


Figure 2.8: Time evolution of the radial profiles plotted at outer mid-plane during inward propagation of neutrals in simulations of SMBI. Figure is taken from [32]

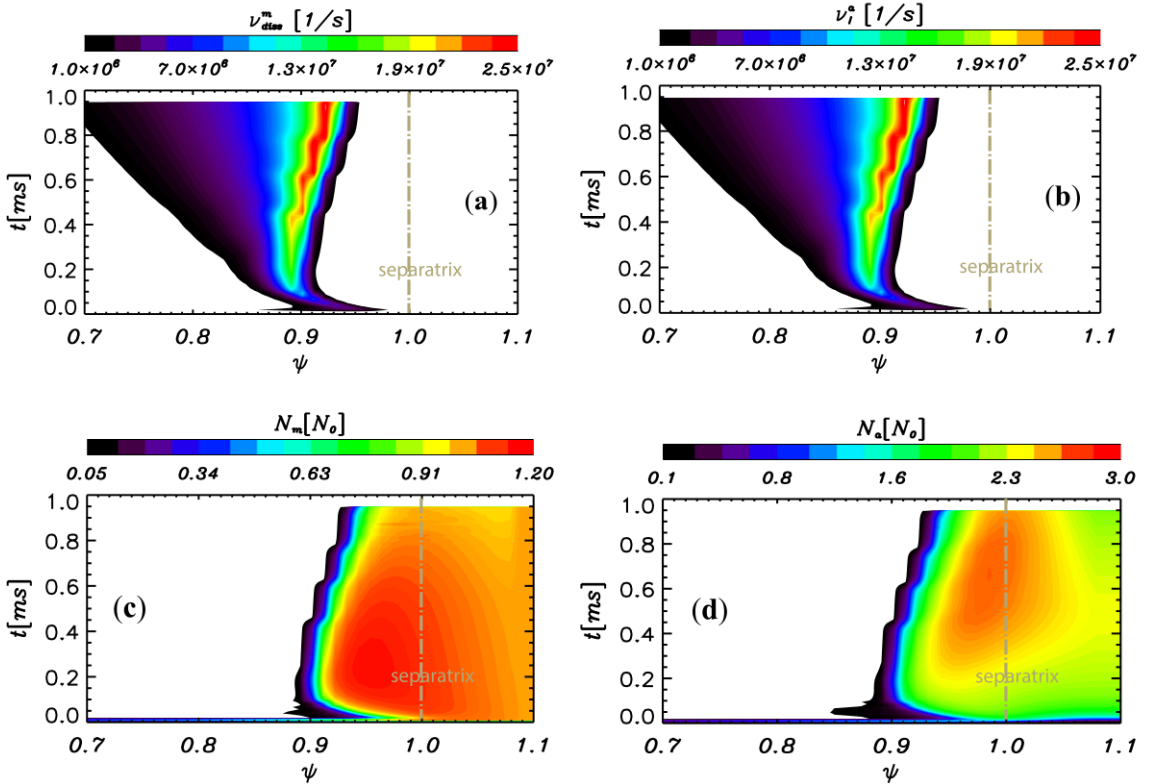


Figure 2.9: Time and spatial evolution of simulated parameters, plotted at outer mid-plane during the SMBI. Figure is taken from [32]

parameters increase the collision frequency and therefore slow down molecular beam penetration. As a result particles are ionized outside the separatrix.

Simulation of the fast and slow components of SMBI [34] was performed to reproduce the experimental observations on HL-2A tokamak, where the fast low dense component of the supersonic beam penetrated deeper into the plasma than the slow high dense component [35]. Simulation results demonstrated that the slow and fast components are distinguished in the simulations and although the injection velocity has some effect on the penetration depth, the penetration is different mainly due to self-blocking effect of the first ionized molecular beam [34].

Comparison between GP injection and SMBI [36] showed that neutrals can penetrate about four centimeters inside the LCFS during SMBI. In GP simulations all

neutrals deposited outside of the LCFS. The injection density were kept the same while the velocity for GP and SMBI were $V_{GP} = 5 \text{ m/s}$ and $V_{SMBI} = 1000 \text{ m/s}$ respectively. The radial convection and larger inflowing flux lead to the deeper penetration depth of SMBI and higher fueling efficiency compared to GP.

Investigation of the molecular penetration depth variation depends on the molecular injection flux [37] leaded to conclusion that the penetration depth increases with the increase of the injection velocity. The penetration depth does not vary much once the SMBI injection density is larger than a critical value which is ($N_{mol} = 0.5 \cdot 10^{19}$). With injection density smaller than the critical value, the molecular injection rate and the dissociation rate are much smaller than the parallel plasma density spreading rate. Thus the plasma continually spreads out in the parallel direction and does not accumulate in the fuelling path to terminate the inward molecular propagation. It was found that the penetration depth mainly depends on the injection velocity even for the same injection flux of SMBI. [37].

LLP code for SMBI

An another model developed by the group of Rozhansky is a MHD code similar to the LLP pellet code [38]. In this 1D model where the jet expansion, deceleration of the ambient electrons and ions by the jet, resulted self-consistent electric field and cooling of the ambient plasma are taken into account. It was shown that the ionization degree and beam penetration strongly depends on the jet density. The critical jet density was around $N_{mol} = 10^{24} \text{ m}^{-3}$ when the plasma electron able to reach the center of the jet and the beam is ionized in plasma quite quickly. Increase of the beam density over the critical value allows deeper penetration of the beam because the electrons can not reach the center of the beam , which remains cold, dense and neutral. In case of the high ionization degree the beam stops at the plasma periphery due to ∇B -induced drift. The small ionization degree is sufficient to stop the expansion across the magnetic field due to compensation of the neutrals pressure gradient by the Lorenz force. This model as well does not include the dynamic of plasma. Comparison of this two models indicates that the density of the molecular beam is essential parameter in description of SMBI in fusion plasma.

2.3 Thesis goals and outline of the thesis

As seen from the literature review, the SMBI is promising fuelling method providing the efficiency higher then traditional GP injection and beneficial in the long pulse operation regimes where the fast plasma response and reduced wall retention are required. In addition some experiments demonstrated the possibility to apply SMBI for the turbulence suppression, but this effect strongly depends on plasma conditions and has not been explained in the consistent way.

The model which describes the intermittent plasma transport self-consistently with dynamics of high speed molecular beam would help to better understand the physics behind interaction of supersonic molecular beam with thermonuclear plasma. In this thesis numerical investigations were performed to answer the following questions:

- how turbulence affects the supersonic molecular beam penetration
- can the "self-shielding" effect be observed in simulations with plasma dynamics

- how the fuelling efficiency depends on the beam velocity, density and width
- under which conditions turbulence suppression by SMBI can be observed

The outline of the thesis is as follows:

In Chapter 3 the main parameter of the supersonic molecular beam are calculated for the SMBI system on KSTAR. Two operation regimes of SMBI with the working gas at the room temperature and with the working gas cooled down to 105 K are considered. Experimental results demonstrating the influence of SMBI on KSTAR plasma are presented in this chapter.

The numerical model used in the thesis is described in Chapter 4. The coupling of the HESEL and SMBI models and description of the supersonic molecular beam in 2D geometry in terms of the HESEL model is presented in the chapter.

The numerical investigation of the SMBI in presented in Chapter 5. Each section of this chapter gives the answer on one the question listed in thesis goals. This chapter illuminates the influence of the neutral sources on the neutral propagation and the plasma in the self-consistent plasma-SMBI modeling, present analysis of the fuelling efficiency as function of the beam parameters. The influence of SMBI on plasma fluctuations and vise versa are discussed as well.

In Chapter 6 the main conclusions of the thesis are summarized.

Chapter 3

SMBI on KSTAR

This chapter focuses on the consideration of the flow through the Laval nozzle and calculations of the exit flow parameters. First section introduces the equations which are required for calculation of the main parameter of the supersonic molecular beam. After consideration of the main equations the calculations are performed for the working parameters of SMBI system on KSTAR (Korea Superconducting Tokamak Advanced Research). Experimental results demonstrating the influence of SMBI on KSTAR plasma are presented in this chapter.

3.1 Characteristics of a supersonic beam

3.1.1 Laval nozzle

By passing gas through a properly designed nozzle, the pressure energy can be converted to the kinetic energy. The nozzle consisting of the diverging and converging sections connected by the throat area provides a flow with a high supersonic speed. A schematic image of such nozzle is shown in Fig. 3.1. This nozzle was invented by the Swedish engineer Gustaf de Laval and therefore converging-diverging nozzles are often called Laval nozzles. The Laval nozzle is the main distinguishing feature of SMBI system from GP system. A nozzle flow can be approximated as an one-dimensional

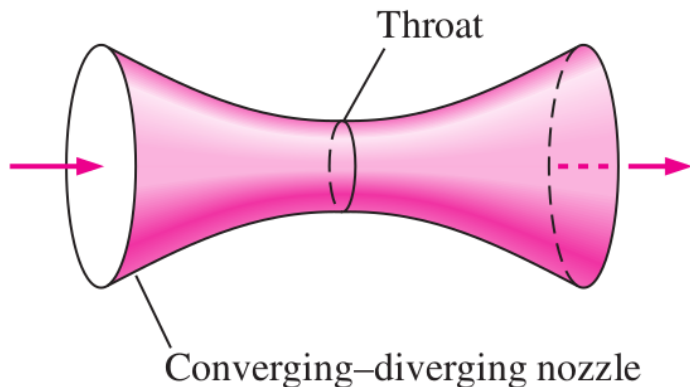


Figure 3.1: Sketch of the Laval nozzle. Figure are taken from [39].

isentropic flow with a good accuracy. A gas flow through the nozzle can be studied by

assuming that the flow parameters, namely gas pressure (P), density (ρ) and velocity (v) are constant at each cross-section(A) of the nozzle and vary only along the length in the direction of the flow [39].

An important parameter in analysis of the fluid flow is the Mach number. The Mach number is the ratio of the actual velocity of the fluid (u) to the speed of sound c in the same fluid

$$M = \frac{u}{c}, \quad (3.1)$$

where γ is adiabatic index. Adiabatic index equals to the ratio of the heat capacity of the gas at constant pressure (C_p) to the heat capacity at constant volume (C_v). Adiabatic index can be also write though the degree of freedom f .

$$\gamma = \frac{C_p}{C_v} = \frac{f+2}{f}. \quad (3.2)$$

The speed of sound in the fluid is

$$c = \sqrt{\gamma RT}, \quad (3.3)$$

where R is the gas constant and T is the temperature of the gas. The combination of the mass and energy conservation equations for the nozzle flow gives the area velocity ratio [39]

$$\frac{dA}{A} = \frac{dP}{\rho V^2} (1 - M^2). \quad (3.4)$$

This equation allows understanding the flow properties in the Laval nozzle. For the subsonic flow, when the Mach number is lower than one, the term $(1 - M^2)$ is positive and dP and dA should have the same sign. In supersonic flow with the Mach number bigger than one, the term $(1 - M^2)$ is negative, and thus dA and dP must have opposite signs. Therefore, at the Laval nozzle, the fluid first passes through a subsonic (converging) section, where the Mach number increases as the flow area of the nozzle decreases, and then reaches the value of unity at the nozzle throat. Then fluid continues to accelerate as it passes through a supersonic (diverging) section.

3.1.2 Exit nozzle velocity and mass flux

If the diameters of the nozzle at the exit and throat areas are know the Mach number can be found by solving the following equation [39]

$$\frac{A}{A^*} = \frac{1}{M} \left[\frac{2}{\gamma + 1} \left(1 + \frac{\gamma - 1}{M^2} \right) \right]^{\frac{\gamma + 1}{2(\gamma - 1)}}, \quad (3.5)$$

This equation has two solutions for supersonic and subsonic branch (Fig. 3.2).

The velocity at the exit of the nozzle is given by

$$u_{exit} = \sqrt{\frac{RT}{m_{gass}} \frac{2\gamma}{\gamma - 1} \left(1 - \left(\frac{P_{amb}}{P_0} \right)^{(\gamma-1)/\gamma} \right)}, \quad (3.6)$$

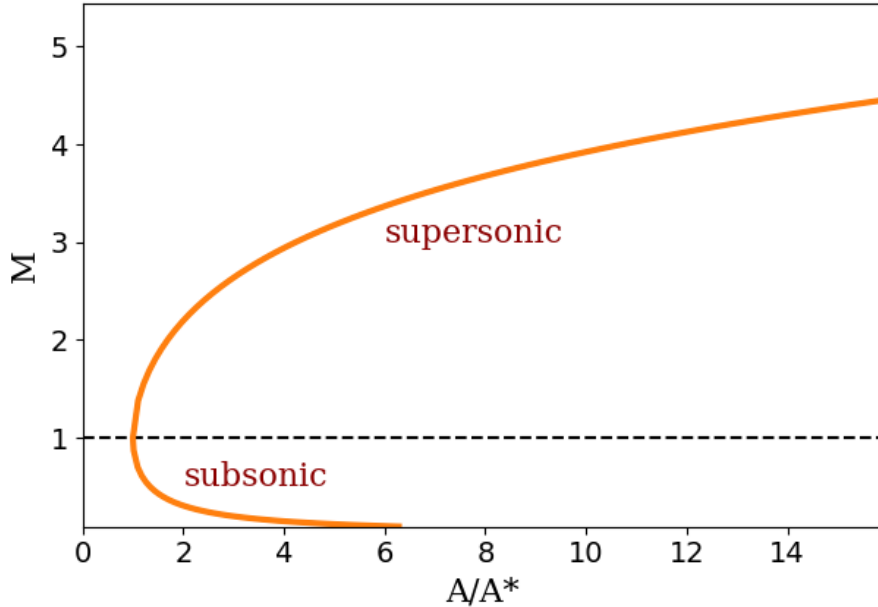


Figure 3.2: Solution of Eq. 3.5 which defines the Mach number as a function of the exit and throat area ratio. Calculation is performed for the diatomic gas with $\gamma = 1.4$.

where P_{amb} is the ambient pressure, P_0 is the stagnation pressure. The maximum possible velocity is obtained when the gas expands to the vacuum and $P_{amb} = 0$. This velocity is defined just by the inner energy of the gas

$$u_{max} = \sqrt{\frac{RT}{m_{gass}} \frac{2\gamma}{\gamma - 1}}. \quad (3.7)$$

The maximum mass flow rate through a nozzle with a given throat area is fixed by the stagnation pressure and the temperature of the inlet flow.

$$\dot{m} = \frac{AMP_0\sqrt{\gamma/RT_0}}{\left(1 + \frac{\gamma-1}{2}M^2\right)^{(\gamma+1)/(2(\gamma-1))}}. \quad (3.8)$$

3.1.3 Isentropic flow equations

The particular relations between upstream conditions (P_0, ρ_0, T_0) , throat (P^*, ρ^*, T^*) and at the nozzle exit (P_e, ρ_e, T_e) are given by the isentropic relations [39]. Once the Mach number is known, the corresponding variation of temperature, pressure, and density along the nozzle can be found from the following isentropic equations

$$\frac{T_0}{T} = 1 + \frac{\gamma - 1}{2}M^2, \quad (3.9)$$

$$\frac{P_0}{P} = \left(1 + \frac{\gamma - 1}{2}M^2\right)^{\frac{\gamma}{\gamma-1}}, \quad (3.10)$$

$$\frac{\rho_0}{\rho} = \left(1 + \frac{\gamma - 1}{2} M^2 \right)^{\frac{1}{\gamma-1}}, \quad (3.11)$$

For the isentropic flow, the distribution of Mach number and hence the resulting distribution of pressure, temperature and density through the nozzle depends only on the local area ratio A/A^* .

Using these equations the parameters of the supersonic molecular beam at the exit of the Laval nozzle can be calculated straightforwardly for the SMBI system on KSTAR.

3.2 SMBI system on KSTAR

3.2.1 Calculations of the SMB parameters

SMBI system on KSTAR can work with deuterium gas in two operational regimes: with a working gas at the room temperature and with gas cooled under 105 K. Therefore, different adiabatic indexes (Eq. 3.2) should be used in calculations. The adiabatic index equals 1.4 corresponds to the gas at the room temperature and the index is equal to 1.58 corresponds to the gas at low temperature 105 K.

The exit nozzle diameter at KSTAR is 3.2 mm and the throat diameter is 0.8 mm, therefore the area ratio is 15.8. According to these values and using Eq. 3.5 the Mach number $M = 4.44$ corresponds to the gas at the room temperature and $M = 5.44$ corresponds to the case of the low temperature. The cross section of the Laval nozzle and the distribution of the Mach number along the nozzle are shown in Fig. 3.3. The distribution of the pressure, temperature, and velocity along the nozzle are calculated by using Eqs. 3.9 - 3.11. The normalized flow parameters along the nozzle are shown in Fig. 3.3, which allows estimation of the exit gas temperature and pressure compared to the stagnation parameters. Only the stagnation flow parameters usually are known from experiments.

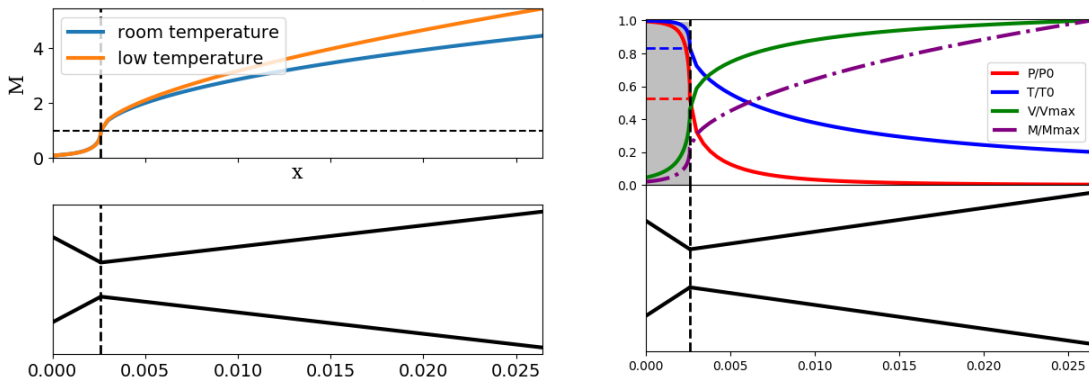


Figure 3.3: Left: mach number along the Laval nozzle. Right: normalized flow parameters along the nozzle for the gas at the room temperature. All parameters include the length of the nozzle (in mm) correspond to the SMBI system on KSTAR.

The exit velocity of hydrogen molecules is calculated from Eq. 3.6 and shown in the Fig. 3.4. The sound velocity corresponds to the thermal energy of molecules and varies along the nozzle due to decrease of the temperature. The direct exit velocity of

the beam is defined by the nozzle configuration and by working gas parameters, which are different on various tokamaks. However, the calculated values for KSTAR are in the same range with the mentioned in literature review in Chapter 2.1. It should be mentioned that even the Mach number is higher for the gas at the low temperature (Fig. 3.3), the exit direct velocity is higher in case of the gas at the room temperature. The increase of the working gas temperature can be one of the way of getting beam with higher exit velocity. The exit velocity on KSTAR is close to the maximum possible value (Fig. 3.4) for this nozzle configuration. However the increase of the working to the ambient pressure ratio would allow to obtain molecular beam with higher velocity.

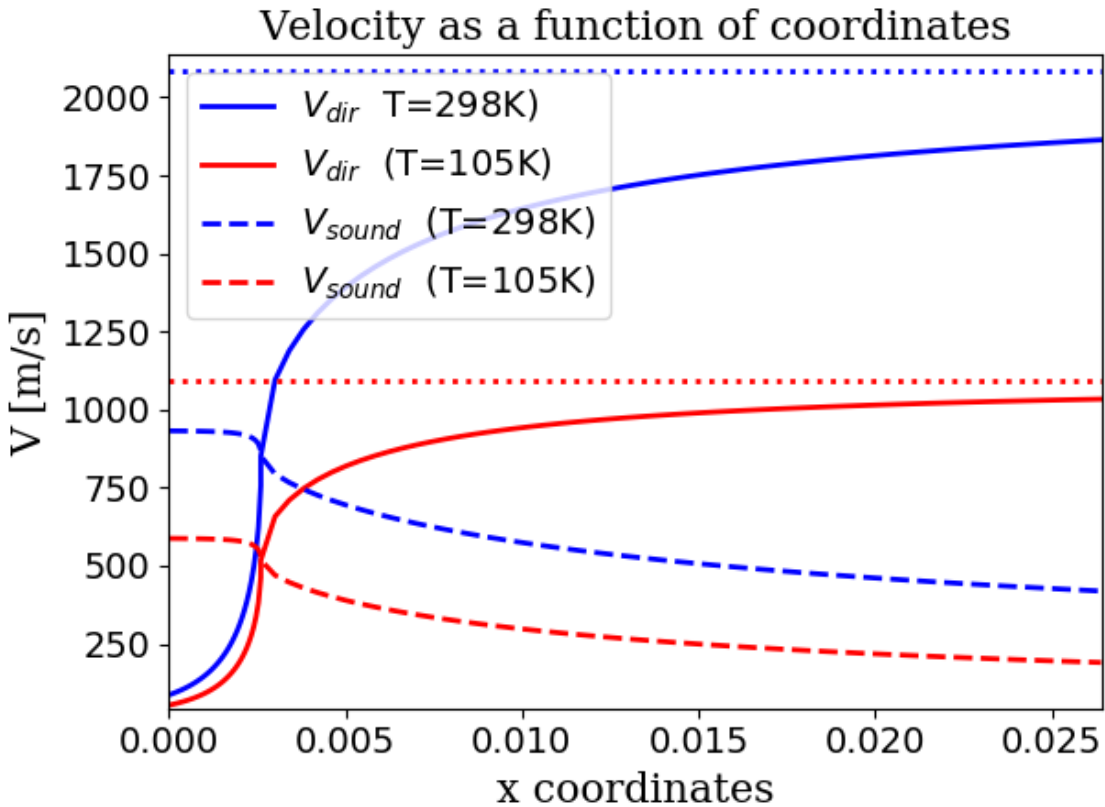


Figure 3.4: The exit nozzle velocity on KSTAR. V_{dirr} is the direct exit velocity, V_{sound} is the speed of sound in the fluid or thermal velocity of particles. Horizontal dotted lines show the maximum velocity which can be reach in this nozzle configuration.

As was mention in section 2.1 under the low pressure and temperature the expanding flow condensates forming the microdroplets or clusters. Clusters behave as micropellets and might improve the penetration characteristics of the beam. There are no comprehensive theory about cluster formation, but the onset of clustering can be described by an empirical scaling parameter [25]. The Hagena parameter Γ^* is

$$\Gamma^* = \frac{k(d/\tan(\alpha))^{0.85} P_0}{T_0^{2.29}}, \quad (3.12)$$

where d is the nozzle diameter in μm , α is the expansion half-angle, P_0 is the stagnation pressure in mbar, T_0 is the stagnation temperature in K, and k is the constant related to the gas species. If the Γ^* is higher than 100 then the conditions of cluster formation

are reached. Regarding to the SMBI system on KSTAR the gas at low temperature is characterized by the Hagena parameter higher the critical level.

As it appears from Eq. 3.8 the number of injected particles has a linear dependence on the working pressure. The dependence of the molecular flux on the working pressure is shown in Fig. 3.5. The working pressure on KSTAR is 8 bar. The comparison of calculated flux with the calibration data is shown in Fig. 3.5. The calculated and calibration values are at the same range. The exit flow parameters for the SMBI

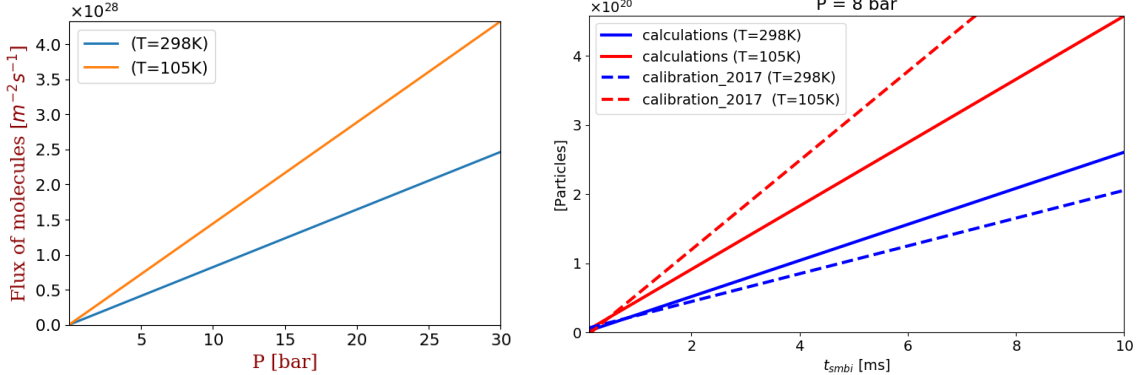


Figure 3.5: The molecular flux as a function of the working pressure (left). The comparison of calculated flux with calibration data (right).

system on KSTAR are summarized at the Table 3.1. As seen from the table the flow under the low working temperature have nearly three times higher density compared to the gas at the room temperature. The cluster formation parameter exceeds the critical value only for gas at low temperature. All of this should lead to the deeper beam penetration in plasma and higher fueling efficiency. At the same time the low temperature gas is characterized by the beam with smaller direct velocity. The analysis of the influence of density and velocity on the beam penetration is performed in Section 5.3.

values at the exit of the nozzle	room temperature (298 K)	low temperature (105 K)
T_e [K]	60	11
P_e [bar]	0.029	0.017
ρ_e [m^{-3}]	3.53×10^{24}	1.15×10^{25}
V [m/s]	1863	1033
Γ^*	23	283

Table 3.1: The flow parameters at the exit of the Laval nozzle. Correspond to the parameters of the Laval nozzle on KSTAR

The Laval nozzle on KSTAR is located at three centimeter away from the vacuum vessel, therefore it makes sense to estimate the variation of the flow parameters along this distance. The size of the Mach disk is given by equation [6]

$$x_d = 0.67d \sqrt{\frac{P_0}{P_{amb}}}, \quad (3.13)$$

where d is the diameter of the nozzle. For SMBI system on KSTAR this value is 60 m, which is much bigger than the distance from the exit of Laval nozzle to the vacuum

chamber. For this reason we use the assumption that velocity of the beam does not change on the distance from the exit of the nozzle to the vacuum chamber. The spreading of the beam due to thermal motion of molecules was calculated by using the values from the Table 3.1. The values of the thermal beam spreading as function of the propagation distance is shown in Fig. 3.6. This is equivalent of the diffusion distance is plotted over the convection distance. As can be seen on the three meter distance the spreading of beam is only several millimetres. Therefore the beam diameter at the entrance of plasma should not exceed one cm and we can assume that the density of the beam at the entrance of the plasma is the same as at the exit of the nozzle.

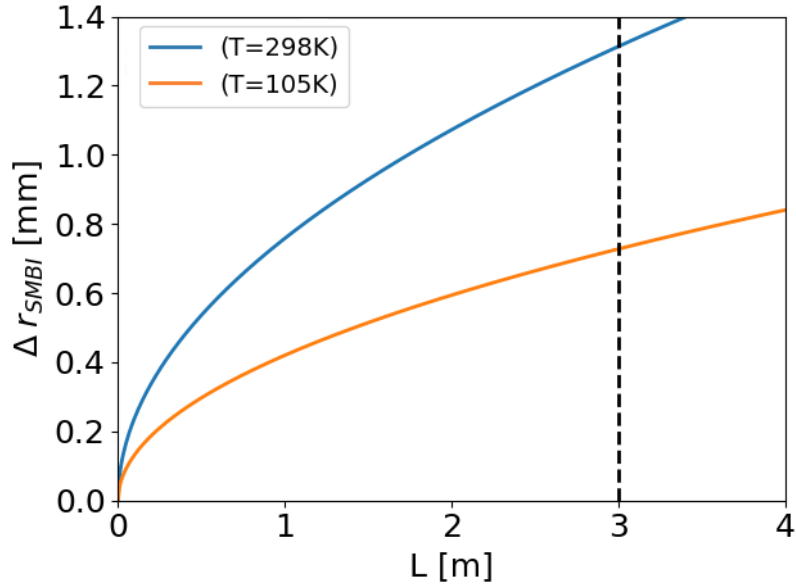


Figure 3.6: The value of diffusion spreading of the beam due to thermal motion of molecules as function of the propagation distance (convection length).

3.2.2 Influence of SMBI on KSTAR plasma

KSTAR tokamak [40] is a medium sized superconducting fusion device in South Korea, Daejeon. KSTAR operates with fully superconducting magnets and maintains a high-temperature plasma over 70 s. The main parameters are following : major radius $R = 1.8$ m, minor radius $a = 0.5$ m, toroidal field $B = 3.5$ T, plasma current $I = 2$ MA, total heating power 28 MW [41]. SMBI together with three GP systems (two at the mid port and one in the divertor) are implemented in the real-time feedback plasma density control system (CODAC), which shares some key similarities with the control system planned for ITER. KSTAR has a range of diagnostics for measuring the plasma parameters Fig. 3.7.

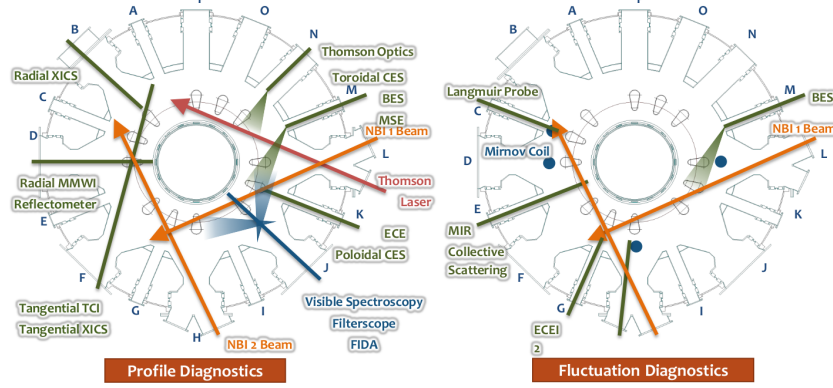


Figure 3.7: Diagnostics layout on the KSTAR tokamak. Figure are taken from [42]. SMBI system is located in the port C.

Unfortunately not all diagnostics were available in experiments with SMBI or provided data with a good signal to noise ratio. Due to time restriction it was impossible to perform dedicated experiments for comprehensive investigation of SMBI on the KSTAR tokamak. However, available data from the experimental campaign in 2016 helps to highlight some features regarding the influence of SMBI on plasma.

One of the main diagnostics, which allows studying the influence of SMBI on KSTAR plasma is the Millimeter-wave Interferometer (MMWI) [42] which measures a line integrated density with the time resolution of $10 \mu\text{s}$. The schematic view of the line of sight of MMWI diagnostic on KSTAR is shown in Fig. 3.8 .

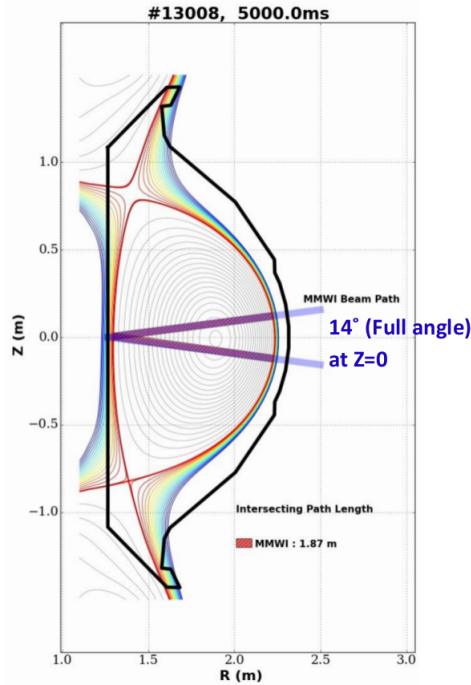


Figure 3.8: Schematic view of the line of sight of MMWI diagnostic on KSTAR. Figure are taken from [42]

The Electron Cyclotron Emission Radiometer (ECE) diagnostic measures the electron plasma temperature with the same time resolution of $10 \mu\text{s}$. 76 channels are

available on KSTAR, although the signal only of them is analyzed in this thesis. The spatial location of the channels depends on the field. The magnetic field $B = 2.5$ T corresponds to the shots analysed below. The position of the considered ECE channel is $R = 1.8$ m. The edge channels of ECE are not calibrated and measurements are presented in arbitrary units. The comparison of the three shots presented in this section is aimed to estimate the influence of the different fuelling methods on plasma.

Shot with GP on KSTAR

First the signal from the shot with GP is presented. The evolution of plasma temperature and density during GP is presented in Fig. 3.9. Plasma density continues to increase during injection time and immediately starts to decrease after termination of injection. The temperature drops and recovers to the value before injection on the same time scale. Plasma density increased by 15 % regarding to the level before injection, while the temperature decreased by 50 %. According to the calibration measurements the neutral flux is measured in atoms per second and is equal to $\Gamma_{GP} = 5.75 \cdot 10^{21} D/s$. The injection time is $\tau_{GP} = 200$ ms and this gives the total number of injected atoms $N_{atom}^{GP} = 1.14 \cdot 10^{21}$.

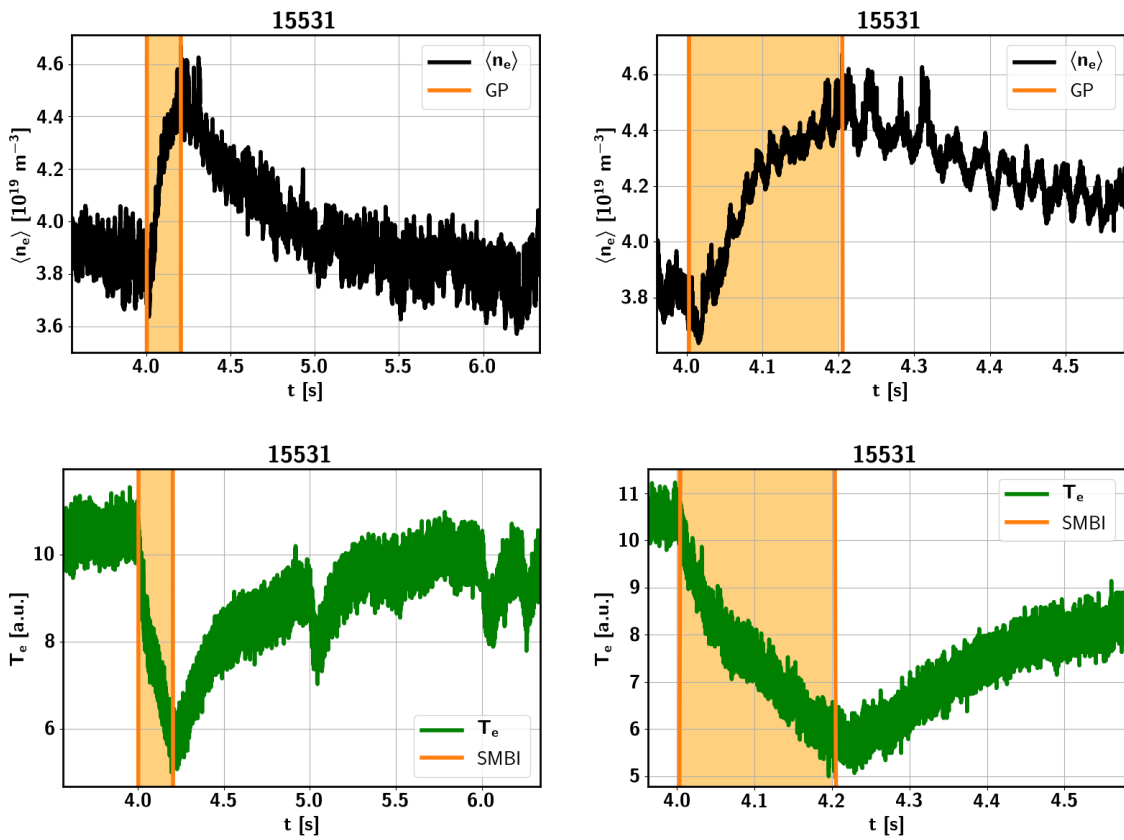


Figure 3.9: Line integrated plasma density and temperature at $R = 1.8$ m measured during GP on KSTAR.

Shots with SMBI on KSTAR

As mentioned above, SMBI on KSTAR works with deuterium gas in two regimes, with the working gas at the room temperature and with the working gas at the temperature

of 105 K.

Plasma density measured in shot with SMBI working with the gas under the room temperature is presented in Fig. 3.10. Measurements of the electron temperature can not be analysed in this shot due to high level of noise. As seen from Fig. 3.10 the plasma density reached the maximum value around 40 ms after SMBI. Level of the averaged plasma density returned to the value before injection in around 0.1 s after start of SMBI. The plasma increment is approximately 6 %. According to the calibration measurements the injected neutral flux is $\Gamma_{\text{SMBI}}^{\text{room}} = 2.0 \cdot 10^{22} D/s$. The injection time is $\tau_{\text{SMBI}}^{\text{room}} = 3 \text{ ms}$ and the number of injected atoms is $N_{\text{SMBI}}^{\text{room}} = 6.5 \cdot 10^{19}$.

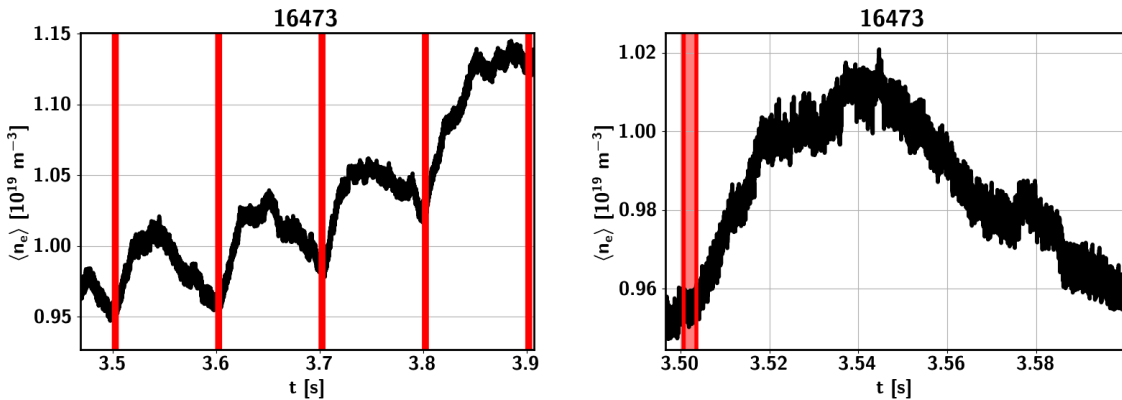


Figure 3.10: Line integrated plasma density measured in shot with SMBI worked with the gas under the room temperature

Plasma density and temperature measured in shot with SMBI worked with the gas at temperature of 105 K are presented in Fig. 3.11. The plasma density reached the maximum value in around 80 ms after start of SMBI and the density level did not return to the value before injection. The higher level of plasma density after injection can be resulted from the deeper penetration of neutrals and therefore better confinement of the created ions. The global modification of the plasma transport properties could be initiated by SMBI and be reflected in increase of the plasma density. The more detailed analysis of the performed shot including the heating power is required to understand the mechanisms of such plasma behavior. The plasma increment is around 40 % and the temperature drop is around 25 % compared to the level before injection. The pulse duration is the same as for SMBI with the gas at the room temperature and equals to $\tau_{\text{SMBI}}^{\text{cool}} = 3 \text{ ms}$. The neutral flux is $\Gamma_{\text{SMBI}}^{\text{cool}} = 6.0 \cdot 10^{22} D/s$ and the total number of injected particles is $N_{\text{SMBI}}^{\text{cool}} = 1.8 \cdot 10^{20}$ respectively.

Comparison of GP and SMBI shots on KSTAR

Comparison of these three shots indicates first of all the different mechanisms of neutral penetration in case of GP and SMBI. This is seen on the plasma density and temperature evolution after termination of the neutral injection. **Continuous increase of plasma density after SMBI can be evidence of the ionization of injected neutrals in the edge region.** The decrease of the plasma density immediately after GP can be caused by the particle losses along open field lines in the SOL region.

As was expected, **SMBI with the working gas at low temperature showed stronger influence on the plasma compared to GP and SMBI with working**

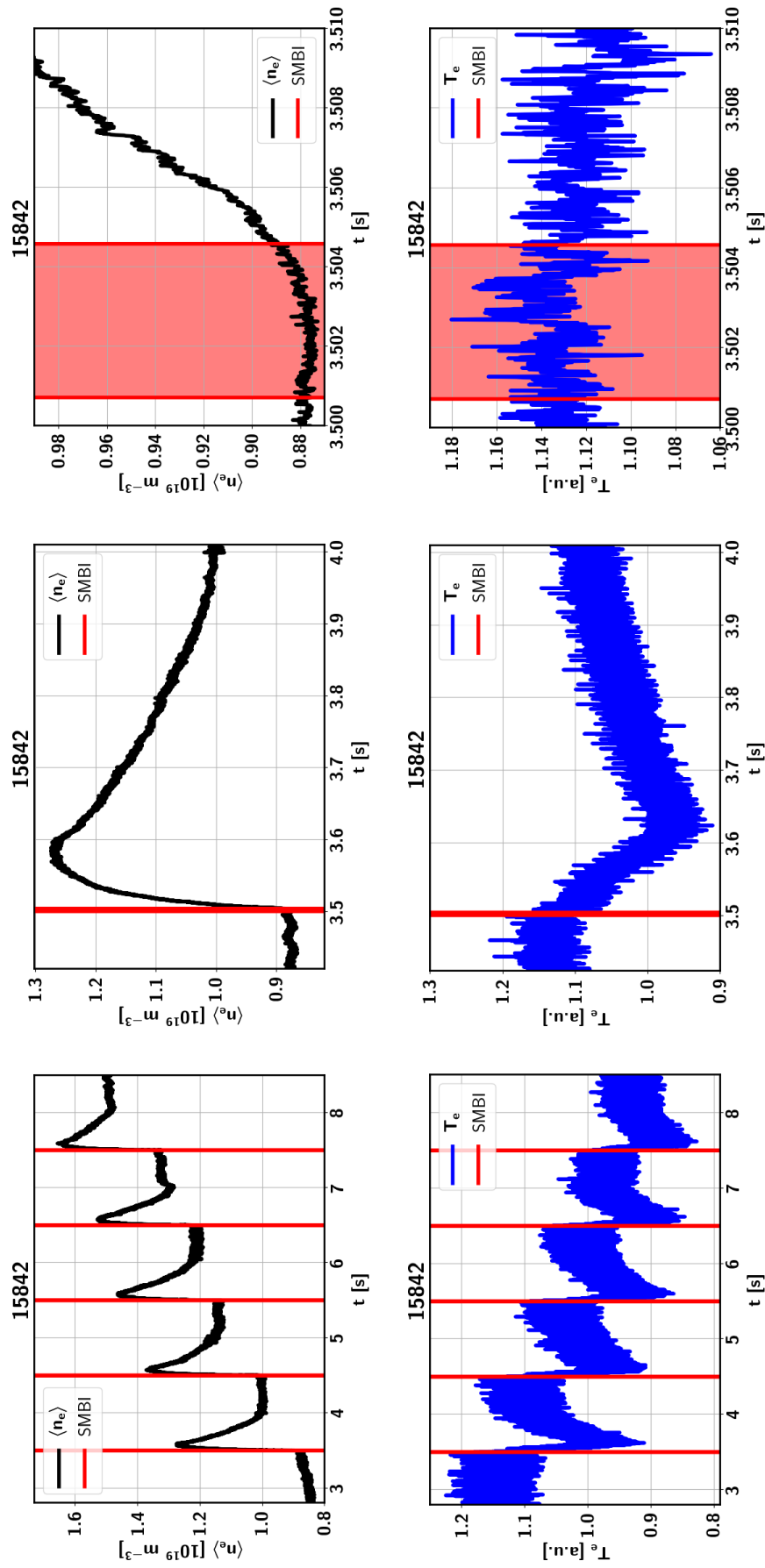


Figure 3.11: Line integrated plasma density and temperature at $R = 1.8$ m measured in shot with SMBI worked with the gas at low temperature

gas at the room temperature. This is understandable as the neutral flux and total number of injected particle in former case are higher compared to SMBI operated with the gas at the room temperature. The effect of the beam condensation and clustering under the low temperature could also take place and lead to the deeper beam penetration and stronger influence on the averaged plasma density. Higher density increment compared to GP, where the total number of injected particles is higher, can be caused by the beneficial effect of the direct velocity of injected molecules. Should be noticed also, that in the shot with GP averaged plasma density before injection is around three times higher compared to the averaged density in shot with SMBI.

SMBI with gas at the low temperature leads to around two times longer time rise of the plasma density compared to SMBI injection with the working gas at the room temperature. In addition should be noticed, that in both cases with GP and SMBI, plasma density and temperature vary in the same time scale, although GP reduced the temperature significantly more than SMBI.

Influence of SMBI on plasma density fluctuations on KSTAR

Microwave imaging reflectometer (MIR) measures the electron density fluctuations with poloidal wave-number up to 5 cm^{-1} and typical time resolution of $1 \mu\text{s}$ [42]. There are 4 radial channels and 16 poloidal as shown in Fig. 3.12.

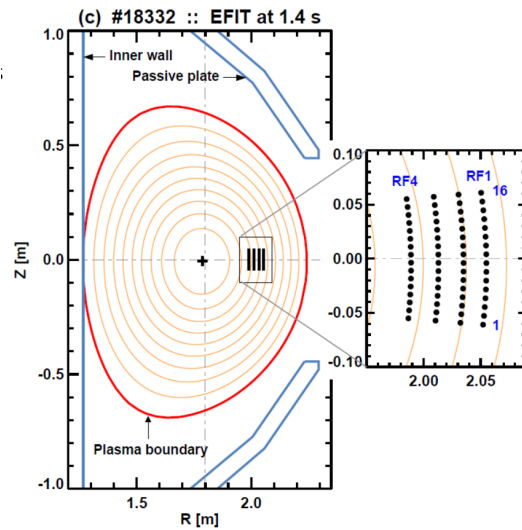


Figure 3.12: Demonstration of the locations of the MIR channels [43]

The spectral power of the plasma density fluctuations was analysed in two shots with SMBI. As shown in Fig. 3.13 the quasi-coherent mode (QCMs) [44] was observed during SMBI [43]. The QCM appears to be suppressed by the increased density plasma density caused by SMBI [45]. QCM is the strongest on the outer-most channel and weaker in the inner-most channel as can be seen in Fig. 3.13. The observed phenomena is reproducible in another shot with SMBI 3.14. The noticeable increase of the spectral power in the high frequency range is observed as well. The more deep analysis is required to explain the observed effects. The presented data demonstrates the pronounced effect of SMBI on the plasma density fluctuations and can be used for further investigation.

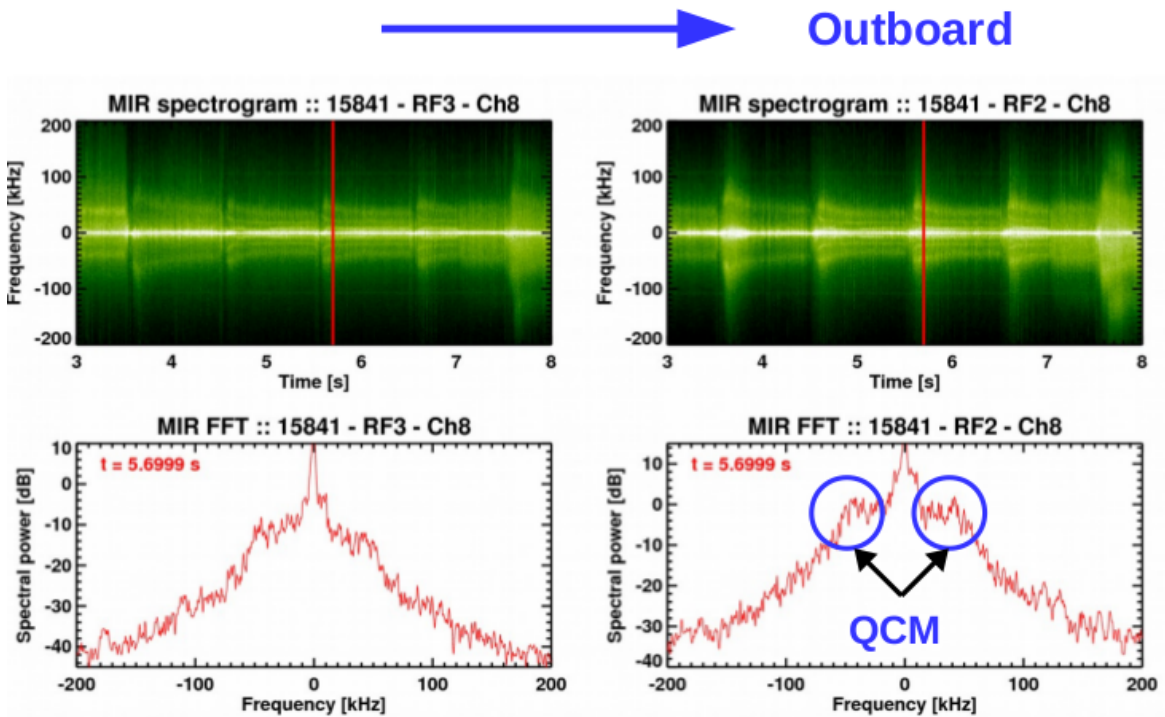


Figure 3.13: Microwave imaging reflectometer signals demonstrating the spectral power of the plasma density fluctuation during SMBI [43]

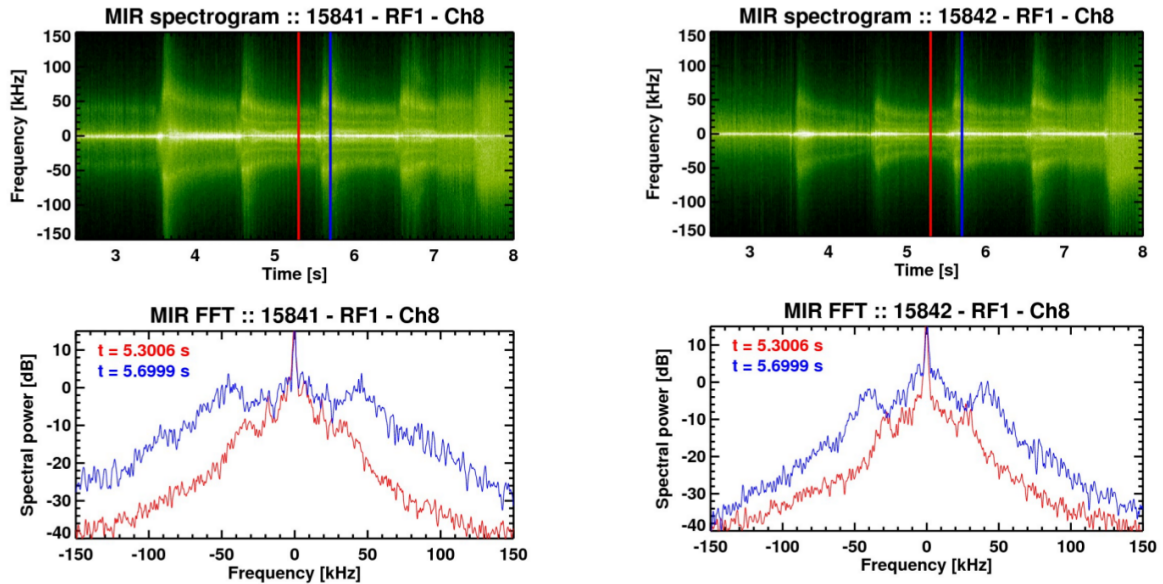


Figure 3.14: Microwave imaging reflectometer data analysed in shots 15841 and 15842 [43]. Red curve demonstrates the power specter of the plasma density fluctuations before SMBI and the blue curve demonstrates the power specter of the plasma density fluctuations during SMBI.

Chapter 4

Numerical simulation of plasma

This chapter describes the numerical model used for the simulations of SMBI. After brief general description of the numerical simulations of tokamak plasma the HESEL model is described. The HESEL model describes the dynamics of the plasma at the outboard mid-plane and is coupled with SMBI model for self-consistent simulations of the plasma - neutral interactions. The coupling of two models and description of the supersonic molecular beam in 2D geometry in terms of the HESEL model is presented.

4.1 Plasma transport equations

Numerical modelling is an essential part of fusion research, as the numerical simulations are intended for understanding the physics processes happening in plasma, especially when diagnostics measurements can not provide data with sufficient spatial and temporal resolution. Modelling is intended also for prediction of the plasma behavior in conditions not reachable by experiment. Due to an enormous number of particles in modern tokamaks, it is unrealistic with the present day computer technologies to solve the system of equations describing the dynamic of each particle, Coulomb interactions between them and electromagnetic fields. Therefore, the main difficulty is to construct the numerical model based on reasonable assumptions and simplifications of the plasma behavior which can be solved with minimum computer resources but at the same time describes the physical processes with capturing the main features.

The first simplification that can be made is a statistical description of particle behaviour. The plasma is described by the number of distribution functions $f_\alpha = (\vec{r}, \vec{v}, t)$ which gives the number of particles per unit volume in the the 6 dimensional phase space at the time t. The evolution of the plasma particles is described by the Boltzmann (kinetic) equation

$$\frac{\partial}{\partial t} f_\alpha + \vec{v} \nabla f_\alpha + \frac{q_\alpha}{m_\alpha} (\vec{E} + \vec{v} \times \vec{B}) \frac{\partial}{\partial \vec{v}} f_\alpha = St_\alpha, \quad (4.1)$$

Where the term $St = \sum_\beta St_{\alpha\beta}(f_\alpha, f_\beta)$ is the sum of the collision operators of species α with species β . In general the collision operator includes elastic and inelastic collisions. For elastic collisions between plasma particles the Coulomb collisions are assumed, where the potential energy of interaction is much less than the thermal energy of particles. Inelastic collisions with neutrals can change the number of particles in the system as well as momentum and energy.

On the whole it is still quite difficult to solve this equation and find expressions for the collisional operator. The next simplification is the description of the averaged characteristics of plasma through the velocity moments of the distribution function. The distribution function moments are combination of the particle velocity components averaged over the distribution.

$$M_n = \int v^n f_\alpha d\vec{v}. \quad (4.2)$$

The zeroth moment represents the average density

$$n_\alpha = \int f_\alpha d\vec{v}. \quad (4.3)$$

The macroscopic fluid velocity is given by the first moment

$$\vec{u}_\alpha = \frac{1}{n_\alpha} \int \vec{v} f_\alpha d\vec{v}. \quad (4.4)$$

The next moment gives the pressure tensor

$$\overline{\overline{P}}_\alpha = \int \frac{m_\alpha (\vec{v} - \vec{u}_\alpha)^2}{2} f_\alpha d\vec{v}. \quad (4.5)$$

The system of equations for the moments of the distribution function is obtained by the multiplication of the kinetic equation Eq. 4.1 on the corresponding term proportional to \vec{v}^n and subsequent integration. Each partial differential equation will contain the terms belonging to the higher order moment equations. It leads to an infinite number of momentum equations and in practice approximate solutions are applied to define unknown variables and describe the system by the finite number of equations. These variables are called the transport coefficients and commonly they are found by the approximate solution of the kinetic equation with the distribution function in the following form

$$f_\alpha = f_\alpha^0 + f_\alpha^1 \quad (4.6)$$

where f_0 is the Maxwellian function and f_1 is the small perturbation to the main function. This approach was suggested by Braginskii [?] and is based on the Chapman-Enskog method for gases. Justification of using this approximate solution is based on the relaxation process, which leads that any distribution function will approach to the Maxwellian as a consequence of collisions [?]. Therefore, this approach is valid in high collisional plasma when the changes in plasma quantities vary slowly on the distance between collisions. Although tokamak plasma are not strictly fulfil this conditions a lot of numerical plasma models based on the Braginskii system of equations namely B2-SOLPS, EDGE2D [46], Tokam-3D [47], GBS , HESEL [48] and others. These codes were verified against the experimental data and despite the used assumptions and simplifications they reveal the main features of plasma behavior. The relative simplicity and reasonable computation time are reasons for the wide use of fluid models.

The Maxwellian distribution function and its derivatives are completely defined by three first statistical moments. The system of the momentum equations is called the transport equations and contains the density continuity equation, the equation of motion and the equation of energy and heat transport. The derivation of this equations

without elastic term and expression of transport coefficients can be found in [?], or with both elastic and inelastic terms in [49]. Here, the resulting system is presented.

$$\frac{\partial n_\alpha}{\partial t} + \nabla(n_\alpha \vec{u}_\alpha) = S_\alpha^n \quad (4.7)$$

$$m_\alpha n_\alpha \left(\frac{\partial \vec{u}_\alpha}{\partial t} + (\vec{u}_\alpha \nabla) \vec{u}_\alpha \right) = -\nabla p_\alpha - \nabla \bar{\pi}_\alpha \quad (4.8)$$

$$+ q_\alpha n_\alpha (\vec{E} + \vec{u}_\alpha \times \vec{B}) + \vec{R}_\alpha + S_\alpha^u - m_\alpha \vec{u}_\alpha S_\alpha^n \Omega$$

$$\frac{3}{2} \frac{\partial p_\alpha}{\partial t} + \frac{3}{2} (\nabla p_\alpha \vec{u}_\alpha) + p_\alpha \nabla \vec{u}_\alpha + \pi_{\alpha j k} \frac{\partial u_{\alpha j}}{\partial x_k} + \nabla \vec{q}_\alpha = \quad (4.9)$$

$$Q_\alpha - \vec{u}_\alpha \cdot \vec{R}_\alpha + S_\alpha^p - \vec{u}_\alpha \cdot S_\alpha^u + \frac{1}{2} m_\alpha u_\alpha^2 S_\alpha^n \Omega$$

Where S_α^n is the particle source due to inelastic collisions with neutral particles. $\bar{\pi}_\alpha$ is the viscosity tensor, which is usually negligibly small for electrons. The physical meaning of the viscosity tensor is a diffusion of momentum in the direction of the velocity gradient. R_α is the resistive force due to collisional friction and difference in particles velocities and the thermal force due to gradient of the electron temperature. S_α^u is a momentum source due to inelastic collisions with neutral particles. Q_α is an energy exchange between moving electrons and ions and q_α is a heat flux, which also depends on the relative velocity and temperature gradient. S_α^p is an energy source caused by plasma neutral interactions.

The next simplification is based on the special feature of charge particle motion in magnetic field.

4.2 Drift-ordering and fluid motion

In the strong magnetic field particles move parallel to the magnetic field much faster than they drift in direction perpendicular to the magnetic field. Consequently, velocity can be split on the parallel and perpendicular parts and terms can be ordered according to their relative magnitude.

The drift ordering permits the iterative solution of the momentum equation and allows getting algebraic equations for each order of velocity. Usually it is sufficient to consider only zero and first order terms. This procedure in more details can be found in [50]. Drift ordering approximation is valid only on the large time scales, when the characteristics frequency is smaller than the ion gyrofrequency

$$\frac{w}{\Omega_i} \ll 1 \quad (4.10)$$

The resulting zero and first order drifts are following

$$\vec{v}_\perp = \vec{v}_{\text{ExB},0} + \vec{v}_{d,0} + \vec{v}_{p,0} + \vec{v}_{R,1} + \vec{v}_{\pi,1} + \vec{v}_{\text{Ped},1} + \vec{v}_{S,1} \quad (4.11)$$

The \vec{u}_{ExB} is a drift in electromagnetic field. As this drift is charge independent it leads to the convection transport of particle in direction perpendicular to magnetic and electric field. The drift is caused by the change in the gyration radius due to the particle acceleration by the electric field. The diamagnetic drift \vec{u}_d is caused by the pressure gradient. Diamagnetic drift is analogy of the gradient-B and curvature drifts

from the particle picture [51]. The polarization drift \vec{u}_p , the viscous drift \vec{u}_π , the resistive drift \vec{u}_R , Pedersen drift \vec{u}_{Ped} , and source drift \vec{u}_S are next order drift terms. The polarization drift arises since the charged particles are accelerated when the leading order drifts vary in time. Due to mass dependence this drift is retained only for ions in numerical simulations. The resistive drift consists of a friction force drift caused by the change of momentum due to collisions and thermal force drift caused by the temperature dependence of the collisionality. The viscous drift likewise is caused by collisions but as it is mass dependant only ion contribution is usually retained. Pederson and source drift are caused by the collisions with neutrals.

The obtained velocity can be directly applied to the system of momentum equation if the parallel velocity parametrized in particular manner or parallel momentum equation is solved.

Assumption of a quasi-neutrality and subtracting the ion and electron density equations yield the vorticity equation. The set of obtained equations, namely the equation of density, vorticity, ion and electron heat is denoted as a drift-fluid or reduced fluid equations. System of such equations self-consistently describes the evolution of plasma density, momentum and energy in time and space and applies for simulations of plasma turbulent transport.

4.3 Coupling of HESEL and SMBI models

The HESEL (hot-edge-sol-electrostatic) model [48], developed at DTU in Denmark, is a reduced drift-fluid model describing the dynamics of the quasi-neutral plasma at the outboard mid-plane of a tokamak. In the limit of the constant ion pressure model is reduced to the ESEL model, which has successfully reproduced the statistical properties and profiles of the plasma in MAST [52], EAST [53], TCV [54]. This motivated us to chose this model for the investigation of the supersonic molecular beam injection and the plasma-beam interactions. As the original HESEL model does not include interactions with neutral species the additional module describing the SMB dynamics were developed and coupled with HESEL model. This module is based on the nHESEL model [49], while some modifications been made due to narrow localization of SMB and stronger effect on the plasma, compared to GP injected. Description of the main features of the HESEL and the SMBI models is presented below.

The HESEL model describes the interchange instabilities driven by the pressure gradient. Obtained through the drift-fluid approximation this model describes the dynamics of the low-frequency turbulences at the outboard mid-plane of the tokamak. The elongation of the blob structures allows reduction of the model to 2D. The radial transport in the edge region mostly concentrated at the region that extend 30 degree above and below the outboard mid-plane, therefore HESEL model comprises only the small area at the outboard mid-plane of tokamak. Model is solving in the slab geometry with the unit vector \mathbf{z} along the inhomogeneous toroidal magnetic field. The magnetic field is approximated by $B(r) = B_0/(1 + \frac{a}{R} + \frac{x}{R})$ where a and R are the minor and major radii of tokamak and x is equal to zero at LCFS. Tokamak geometry and poloidal magnetic field lines are accounted for by a neo-classical Pfirsch-Schlüter correction to the diffusion coefficients. The magnetic field perturbations are neglected and the model is electrostatic. HESEL simulates open and closed regions with a smooth transition between. Difference between the two region, that the open filed line region contains parametrized parallel loses. The model uses the assumption of the finite bal-

loonging length for the parallel transport, equal to $L_b = qR$. Plasma propagates along the magnetic field lines with a speed of $2M_{\parallel}c_s$ where the c_s is the ion sound speed , $M_{\parallel} = 0.5$ is a parallel Mach number. Losses due to advection and electron heat conduction along the magnetic field lines in the SOL region are represented by the damping rates. The model contains the plasma density equation, vorticity equation, ion and electron pressure equations. In addition, model applies the finite layer approximation for vorticity [55]. At the inner part of the edge region plasma profiles are forced to the prescribed values and this acts as sources of the particles and energy. Dirichlet boundary conditions, in agreement with the prescribed profiles, conditions are applied at the inner radial boundary and zero gradient Neumann boundary conditions at the outer radial boundary. Periodic boundary conditions are imposed in poloidal direction. The illustration of the HESEL domain is shown in Fig. 4.1

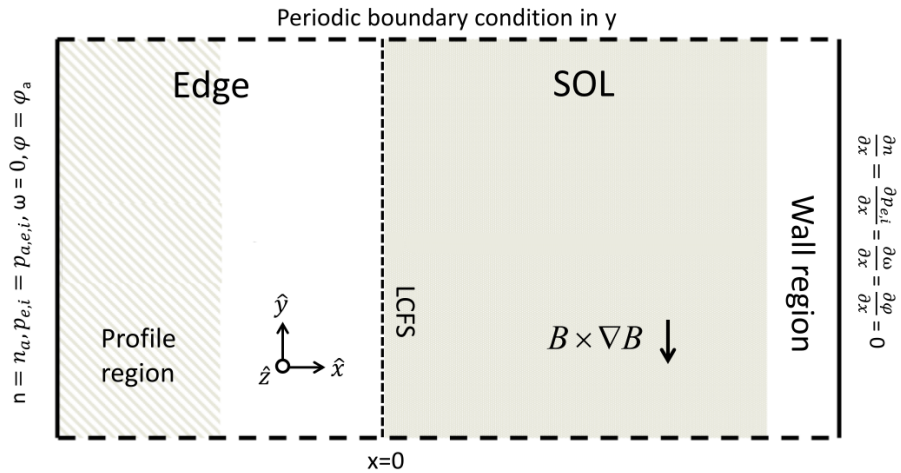


Figure 4.1: Illustration of the HESEL domain. Figure is taken from [48]

The diffusion-convection equations for describing the SMBI were added to the HESEL system of equation.

$$\begin{aligned} \frac{dN_{\text{mol}}}{dt} - \nabla(D_{\text{mol}} \nabla N_{\text{mol}}) + \nabla(V_{\text{SMBI}} N_{\text{mol}}) = \\ -n_e N_{\text{mol}} \langle \sigma v \rangle_{\text{mol}}^{\text{diss}} - n_e N_{\text{mol}} \langle \sigma v \rangle_{\text{mol}}^{\text{ion}} \end{aligned} \quad (4.12)$$

$$\begin{aligned} \frac{dN_{\text{FC}}}{dt} - \nabla(D_{\text{FC}} \nabla N_{\text{FC}}) + \nabla(V_{\text{SMBI}} N_{\text{FC}}) = \\ 2 n_e N_{\text{mol}} \langle \sigma v \rangle_{\text{mol}}^{\text{diss}} - n_e N_{\text{FC}} \langle \sigma v \rangle_{\text{atom}}^{\text{ion}} \end{aligned} \quad (4.13)$$

Where N_{mol} is the molecular density, N_{FC} is the atomic density, n_e is the plasma density, $\langle \sigma v \rangle$ is the reaction rate for the corresponding atomic process. The Eq.4.12 describes the dynamic of the molecules which subjected to dissociation and ionization processes. The choice of atomic processes included in the model is based on the work [49]. The Eg.4.13 describes the dynamic of the Franck-Condon atoms created by the dissociation of injected molecules. Atoms have the same direct velocity as super-sonic molecules and they are subjected to ionization. The injection source is set by the Dirichlet boundary conditions at the outer radial boundary and the zero Neumann boundary conditions are applied at the inner radii boundary. The boundary conditions allows variation of the beam size and density. The possibility of "switch on/off"

the beam dynamics at arbitrary moment of simulations is implemented in the code. Derivation of the particle and energy sources due to plasma-neutral interactions and implementation in the HESEL model can be found in [49]. For the numerical investigations performed in this thesis only the main terms are retained. All terms proportional to the m_i , m_e and m_e/m_i are neglected as they are smaller compared to terms proportional to the ϕ . Therefore, the retained terms are following

$$\Sigma_n = n_e(N_{\text{mol}}K_{\text{mol}}^{\text{ion}}(T_e) + N_{\text{FC}}K_{\text{atom}}^{\text{ion}}(T_e)), \quad (4.14)$$

$$\begin{aligned} \Sigma_{pe} = & -\phi_{\text{diss}}n_eN_{\text{mol}}K_{\text{mol}}^{\text{diss}}(T_e) - \phi_{\text{ion}}n_eN_{\text{mol}}K_{\text{mol}}^{\text{ion}}(T_e) \\ & -\phi_{\text{ion}}n_eN_{\text{FC}}K_{\text{atom}}^{\text{ion}}(T_e). \end{aligned} \quad (4.15)$$

The comparison of the simplified model used in this thesis and the full source model described in [49], as well as the effect of inclusion atoms generated by charge-exchange processes, are presented and discussed in Section 5.2.2.

As the HESEL is 2D model with the parallel length parametrized the special of the neutral source need to be taken. Following assumptions are used. The ionization source is instantaneously distributed along the flux tube of length $L_b = Rq$. The size of the beam in parallel direction is constant and equal to $w_{\text{beam}} = 1$ cm. The correction coefficient is introduced

$$K_{\text{toroidal}} = \frac{w_{\text{beam}}}{L_b} \quad (4.16)$$

Also the periodic boundary conditions are taken into account by the following correction coefficient is introduced.

$$K_{\text{periodic}} = \frac{2\pi a}{L_y} \quad (4.17)$$

where the a is a minor radius of tokamak and L_y is a size of the HESEL domain in the poloidal direction.

The resulting particle source is multiplied on the K_{periodic} and K_{toroidal} while adding to the HESEL equations. These correction coefficients are implemented in the model and varies according to the input parameters.

The model is implemented in BOUT++ framework [56], using the implicit time solver and the 4th order differential scheme.

Chapter 5

Investigation of SMBI by numerical simulations

Since the diagnostics on KSTAR can not provide the plasma profiles at the edge/SOL region with the required signal to noise ratio, the goal of the numerical simulations is investigation how penetration of neutrals and their impact on plasma depend on beam parameters, rather than the direct comparison of simulation results with experimental data. The initial parameters of the simulations, the main features of the numerical data and the structure of the presented results are given in Section 5.1. Section 5.2 illuminates the influence of the neutral sources on the neutral propagation and the plasma in the self-consistent plasma-SMBI modeling. Analysis of the fuelling efficiency as function of the beam parameters is presented in Section 5.3. The influence of SMBI on plasma fluctuations and vice versa are discussed in Sections 5.4 and 5.5 respectively.

5.1 Introduction to the numerical data of HESEL - SMBI simulations

To facilitate the interpretation of the results some main features of the numerical data are presented in this section. First the initial parameters of the HESEL code and the data of the reference simulation without neutral injection are discussed. Then the results of the combination of the HESEL code and SMBI module are described. The correspondence of the initial parameters for the SMBI module to the values calculated in Section 3.2 is discussed as well.

5.1.1 HESEL data

As mentioned in Section 4.3, the HESEL model describes the plasma dynamics at the outboard mid-plane of a tokamak. The typical initial parameters for the HESEL simulations are relevant for a medium-sized tokamak. Unless otherwise stated, the reference parameters for the presented results in this thesis are : major radius $R = 1.8$ m, minor radius $a = 0.5$ m and parallel connection length to the divertor targets $L_c = 15.0$ m.

The magnetic field strength is $B_0 = 2$ T and the safety factor is $q = q_{95} = 5.5$. The deuterium plasma and neutrals are considered in all simulations. The gyro-Bohm normalization parameters are used in the model, namely the characteristic elec-

tron density $n_0 = 1.5 \cdot 10^{19} \text{ m}^{-3}$. the characteristic electron and ion temperatures $T_{e0} = T_{i0} = 20 \text{ eV}$. They are correspond to the following transport coefficients: the neoclassical electron diffusion coefficient $D_e = 3.2 \cdot 10^{-2} \text{ m}^2\text{s}^{-1}$, the neoclassical ion diffusion coefficient $D_i = 1.3 \text{ m}^2\text{s}^{-1}$. The plasma parameters are following: the characteristic ion gyro-frequency $\Omega_{ci} = 7.48 \cdot 10^7 \text{ s}$ and the cold-ion hybrid thermal gyro-radius $\rho_s = 4.13 \cdot 10^{-4} \text{ m}$. The numerical domain is $11 \times 11 \text{ cm}$ and consists of three regions as described in Section 4.3. The width of the edge region (exclude the force region) is 6 cm, the width of the SOL region is 4 cm and the width of the wall region, which acts as a dumping layer, is 1 cm. The space resolution is $\text{dx} = \text{dz} = 5.2 \cdot 10^{-3} \text{ m}$.

Reference simulation without SMBI

HESEL simulations reproduce the dynamics of a hot plasma, which is characterised by the propagation of field-aligned filaments or blobs from the edge into the SOL region. These blobs have amplitude significantly higher than that of the ambient plasma and large radial velocity components [57]. The contour plots of the particle density and the electron temperature are shown in Fig. 5.1, where the evolution of the spatial structure of plasma and the propagation of the blobs are demonstrated.

The existence of the dense plasma structures in the center of the SOL region, as well as the correlation of the plasma density and electron temperature are observed. Fig. 5.2 depicts the time evolution of the plasma density and the electron temperature from the probe marked by the star in Fig. 5.1. The intermittency of the signal and the large fluctuations around the mean value of the signal are clearly seen.

Assumption of the poloidal symmetry of the plasma allows an averaging of plasma fields in the poloidal direction.

In order to define the correct time interval, which contains a sufficient number of intermittent events and provides a reliable mean value, the auto-correlation function $A(\tau)$ for the plasma density fluctuations ($\tilde{n}_e(t, x, y) = n_e(t, x, y) - \langle n_e(x, y) \rangle_t$) is calculated as

$$A(\tau) = \frac{\langle \sum \tilde{n}_e(t, x, y) \langle \tilde{n}_e(t - \tau, x, y) \rangle_t \rangle_y}{A(0)}, \quad (5.1)$$

where τ is a time lag for the discrete-time signal $\tilde{n}_e(t, x, y)$. The auto-correlation function for the plasma density fluctuations at three radial positions is shown in Fig. 5.3. It is noticed that, the auto-correlation time ($\tau_{\text{auto}} = \frac{1}{e} A(\tau)$) is in the order of tens μs and increases with the radial distance from the edge to the SOL region. Similar values of τ_{auto} were found in [58, 59]. The auto-correlation time represents the characteristic time scale of the burst events or plasma filaments. The radial increase of the auto-correlation time is due to slower radial propagation speed of the plasma filaments in the far SOL [57].

The temporally averaged signals presented in this thesis are taken over 270 $\mu\text{s} \sim 27\tau_{\text{auto}}$, unless otherwise stated. Such signals contain around twenty intermittent events and the time averaging provides the reliable mean value.

The poloidally and temporally averaged plasma profiles of the reference HESEL simulation without SMBI are shown in Fig.5.4. The red vertical bars indicate the root mean square values about the average value which define the statistical error of the numerical data. As seen from the plots, the chosen time interval provides the reliable mean values: where plasma density and temperature errors are below 2 % in the edge region and up to 10% in the SOL region. The last one cm of the domain is the wall

region where the amplitude of the perturbations and background values are the lowest. The errors in this region are around 10-14 % for the plasma density and 8-10 % for plasma temperature. Errors for the pressure are slightly bigger, specifically they are up to 5 % in the edge, 5-15 % in the SOL region and 15-25 % in the wall region.

This simulation without neutral injection serves as a "reference" for comparisons with simulations with different neutral injection.

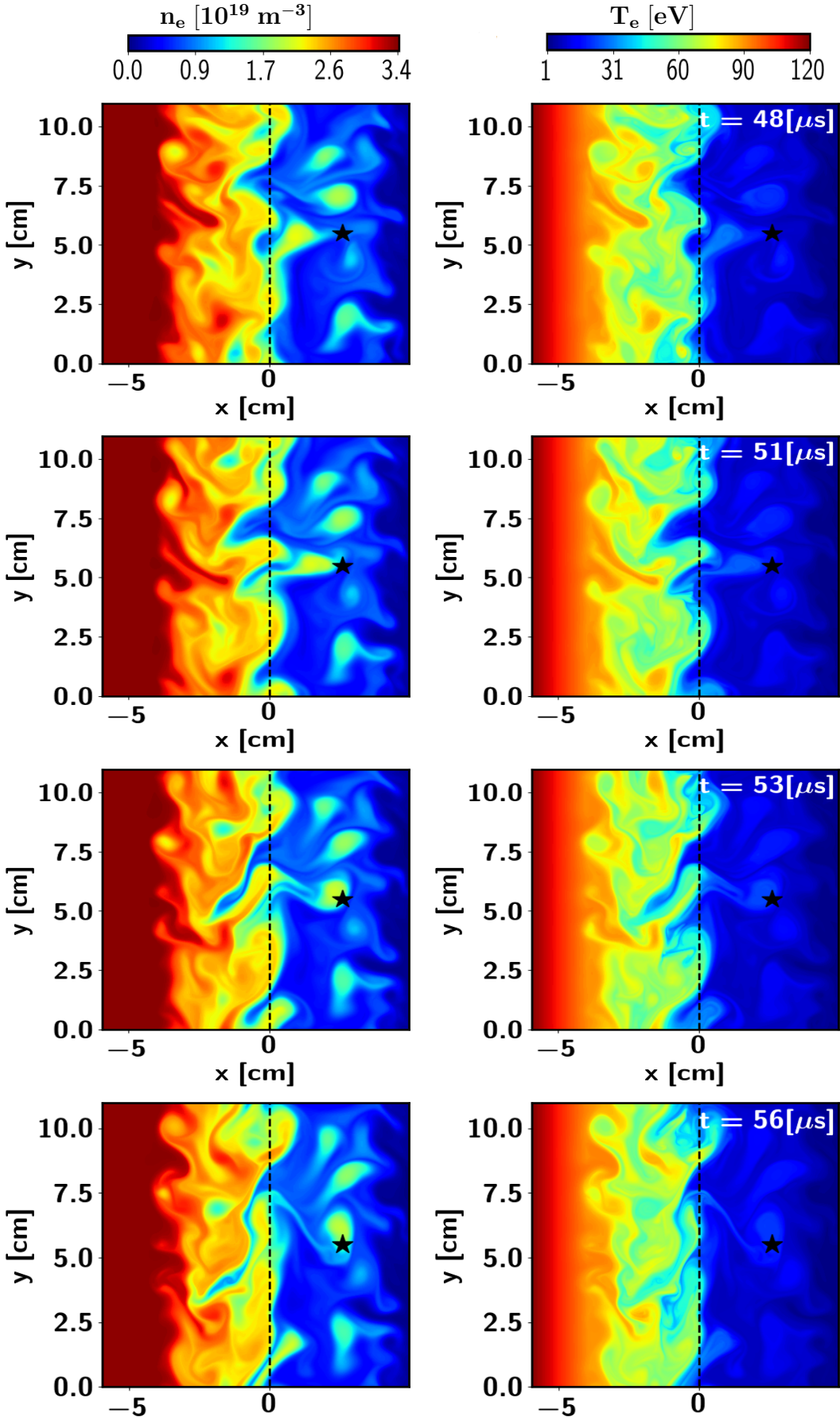


Figure 5.1: Contour plots of the plasma density (left) and electron temperature (right) over $8 \mu\text{s}$. The black star is the position of the probe used for the time signal in Fig. 5.2. Vertical lines indicate the position of the LCFS.

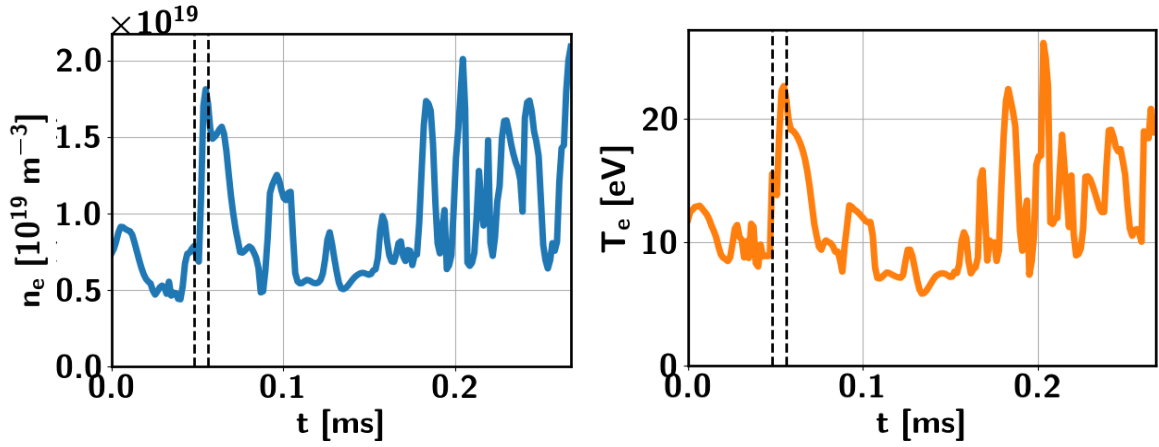


Figure 5.2: The temporal signal of the plasma density and plasma temperature from the probe marked by the star in Fig. 5.1. Vertical lines show the time interval of the signal presented in Fig. 5.1

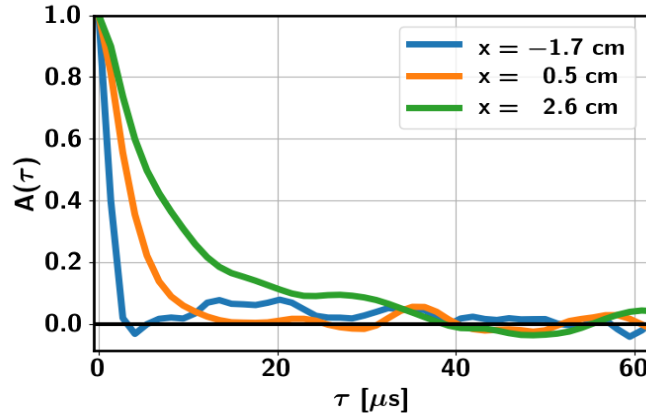


Figure 5.3: The auto-correlation function for the plasma density fluctuations at three radial positions.

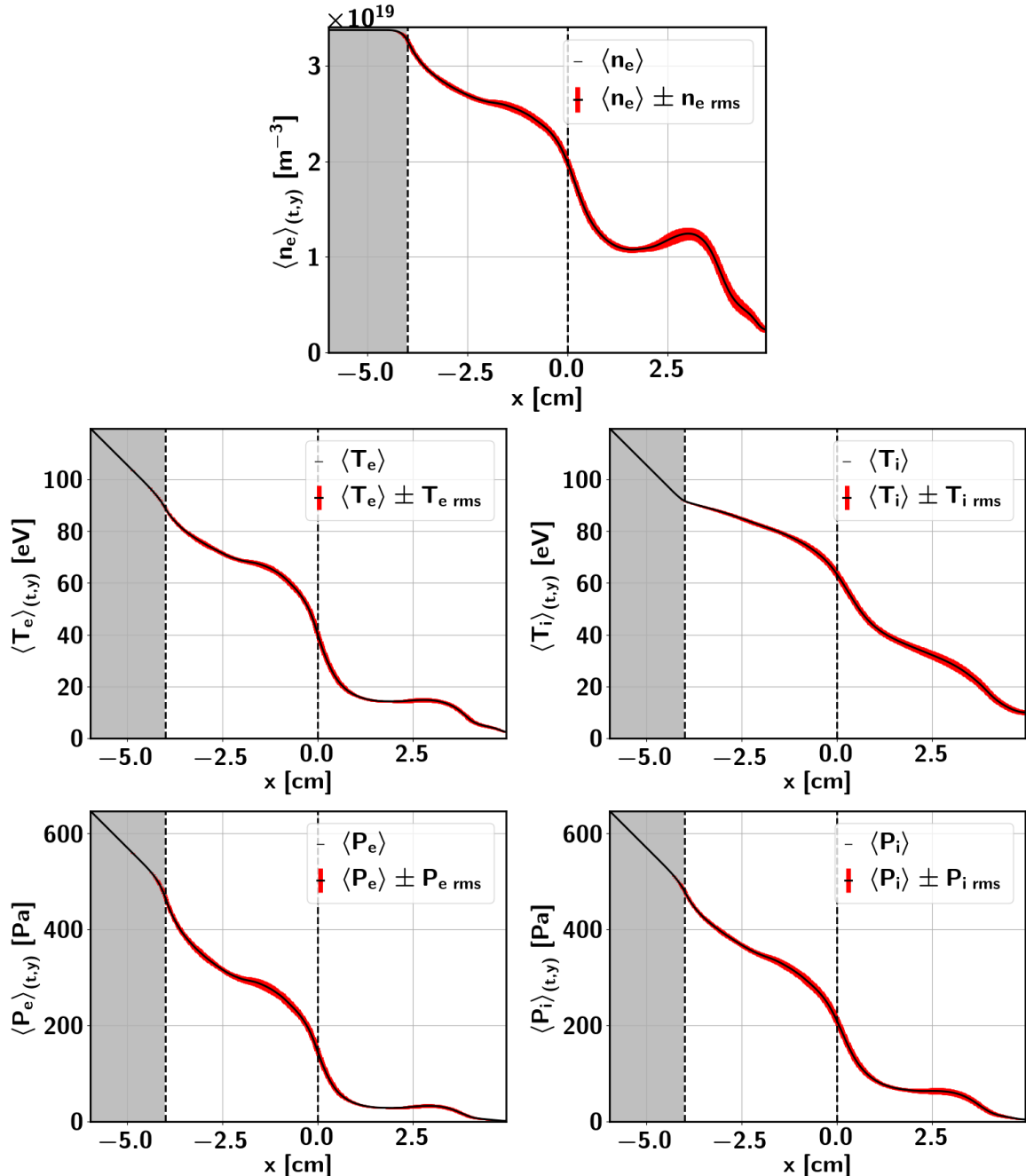


Figure 5.4: The averaged profiles of the plasma fields

. The root mean square values around the mean values indicates the statistical error of the numerical data. Grey area depicts the region with prescribed plasma profiles.

5.1.2 SMBI data

The initial parameters of SMBI module include the intensity of the molecular beam, the direct velocity of injected molecules and the duration of injection.

For the data used in this thesis, the neutral beam locates in the poloidal center of the domain and the density distribution is described by the Gaussian function apart from the beam width scan, where the uniform distribution of the molecules is used in some simulations. The typical initial profile of the molecular beam is shown in Fig. 5.5. The standard beam width, measured as the full width at half maximum (FWHM) of the Gaussian distribution, is two cm. It exceeds the calculated value of the beam width at the entry of the plasma, which is around one cm (Section 3.2), but is still smaller than the measured values of the beam spot in the plasma on ASDEX Upgrade [28], which are around 17 - 20 cm. Due to lack of precise measurements of the beam width at the entry of the plasma, any values in the range of 0.5 – 10 cm might be reasonable.

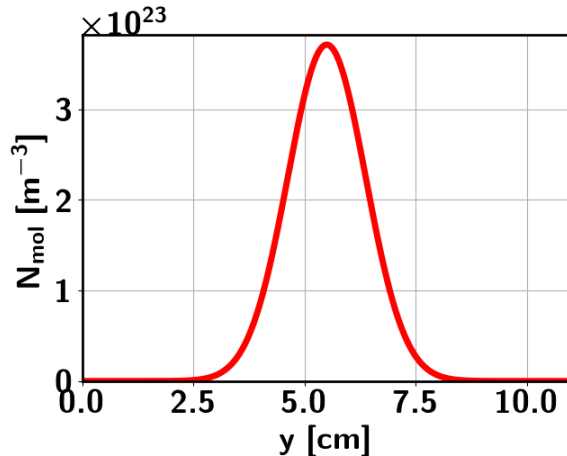


Figure 5.5: The initial molecular beam profile.

The intensity of the beam is defined as the mean value of the initial molecular beam profile and for simplicity the notation of $\langle \rangle$ is omitted hereafter for the molecular density (N_{mol}). The maximum intensity of the molecular beam is restricted by the HESEL boundary conditions and prescribed profile of the plasma density in the inner edge region. In order to keep the working parameters of the HESEL model, which are required for the correct description of the plasma dynamics, the density source produced by the ionization of injected neutrals should not lead to excess of the prescribed density level in the inner edge region. This level depends on the initial parameters for the HESEL model. In the considered simulations the critical neutral density level is approximately $N_{\text{mol}} \sim (60 - 90) \cdot 10^{21} \text{ m}^{-3}$. This is approximately two orders of magnitude smaller than the values mentioned in Section 3.2. Except for the beam velocity scan the molecular velocity is 1000 ms^{-1} which is in the same order of magnitude as the velocity calculated in Section 3.2.

In all simulations the supersonic molecular beam is injected into the same plasma condition and the injection lasts until the end of the simulations. Data for the statistical analysis are taken 0.8 ms after the start of SMBI, when the plasma-neutral interactions reached the conditions close to the steady-state. The averaged values of the plasma density and electron temperature in the edge and SOL regions as functions of time during SMBI are shown in Fig. 5.6. As seen from the plots, the quasi steady-state

conditions are approached less than one ms after the start of SMBI. The grey area in Fig. 5.6 indicates the time interval of the signals analysed in this thesis.

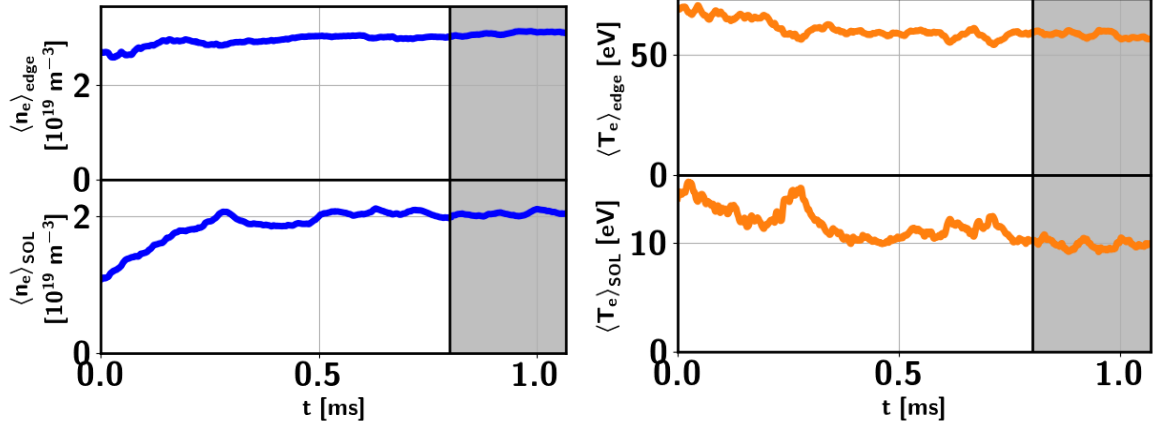


Figure 5.6: Plasma density and temperature averaged in the SOL and edge regions during SMBI as functions of the time. The grey area shows the time interval of the signal analysed in this thesis. The initial parameters for the simulations correspond to the case *I4* in Table 5.1.

The dynamics of the molecules is described by the convection-diffusion Eq. 4.12. A dissociation of molecules results in creation of Franck-Condon atoms which are described by the convection-diffusion Eq. 4.13 with the corresponding source and sink terms. Atoms are created with the same direct velocity as injected molecules and with an energy of 2 eV. While the direct velocity is the initial parameter, the diffusion coefficient is proportional to the thermal energy, i.e.

$$D_n = \frac{1}{2} \frac{T_n}{m_n n_n \langle \sigma v \rangle_n}, \quad (5.2)$$

where T_n , m_n are the energy and mass of the neutral species, n_n is the total density of interactive particles. The reaction rate $\langle \sigma v \rangle_n$ includes all possible interactions between neutrals and plasma particles. Reaction rate of neutral-neutrals collision (assuming kinetic diameter of molecular is $d = 2.8 \times 10^{-10} \text{ m}$ and volume $V = d_{SMBI}^3 = 10^{-6} \text{ m}^3$) is

$$\langle \sigma v \rangle = \pi d^2 V = 8.8 \times 10^{-16}. \quad (5.3)$$

As seen this reaction rate is much smaller compared to reaction rates of the plasma-neutral interactions (Fig. 5.7).

In reality the diffusion coefficient should depend on the local values of the plasma density, temperature and neutral density, however for computational reasons it is taken as a constant. The coefficients $D_{\text{mol}} = 0.03 \text{ m}^2 \text{s}^{-1}$ and $D_{\text{FC}} = 33.3 \text{ m}^2 \text{s}^{-1}$ were obtained by using the following parameters: $T_{\text{mol}} = 0.003 \text{ eV}$, $T_{\text{FC}} = 2 \text{ eV}$, $n_{\text{mol}} = 3 \cdot 10^{19} \text{ m}^{-3}$, $n_{\text{FC}} = 7.5 \cdot 10^{19} \text{ m}^{-3}$, $\langle \sigma v \rangle_{\text{mol}} = 10^{-13} \text{ m}^3 \text{s}^{-1}$, $\langle \sigma v \rangle_{\text{FC}} = 8 \cdot 10^{-14} \text{ m}^3 \text{s}^{-1}$, $m_{\text{mol}} = 2 \cdot 1.6 \cdot 10^{-27} \text{ kg}$ and $m_{\text{FC}} = 1.6 \cdot 10^{-27} \text{ kg}$. For the molecules there is also a restriction by a resolution of the domain, as a high ratio of the diffusion coefficient to the direct velocity requires a small spatial step which increases the computation time. In addition, the reduction of the diffusion coefficient below the value $0.03 \text{ m}^2 \text{s}^{-1}$ does not make any visible modification in the penetration of the molecular beam. Therefore, the chosen diffusion coefficient was calculated for the underestimated values of the molecular density.

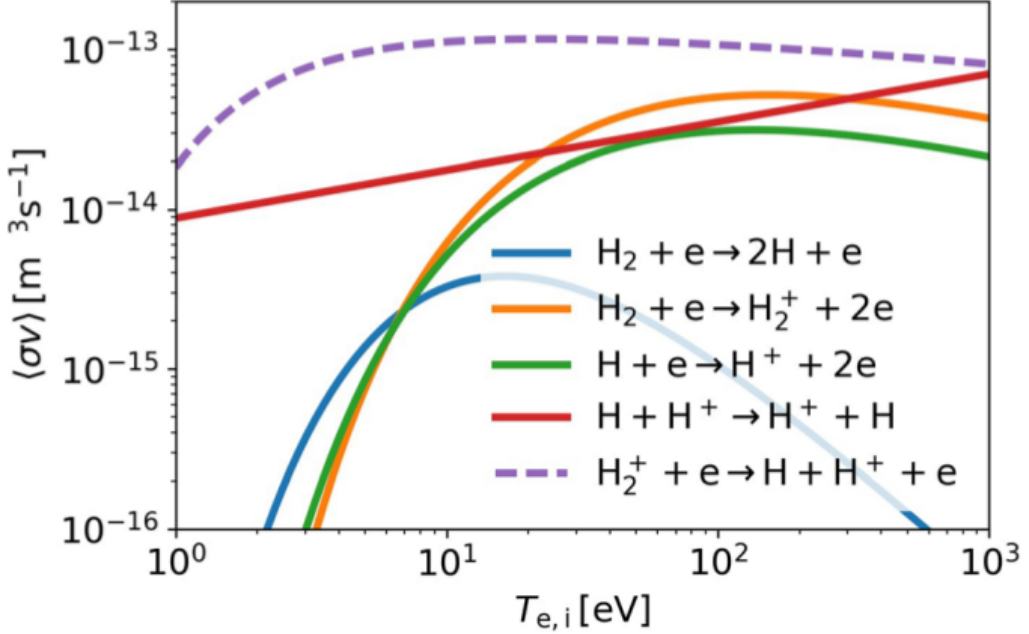


Figure 5.7: The reaction rates for the atomic processes included in the model. Figure are taken from [49]

The ratio of the convection transport rate to the diffusion transport rate is defined by the Péclet number

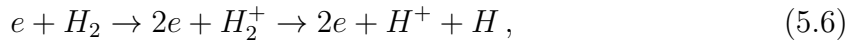
$$Pe = \frac{LV}{D}, \quad (5.4)$$

where L is the characteristic length, V is the velocity and D is the diffusion coefficient. With the centimeter scale characteristic length and the velocity 10^3 m/s, the Péclet number for the molecules is 286 and consequently the convection transport significantly dominates over the diffusion transport. For the atoms, on the other hand, $Pe \sim 0.3$ which indicates the weak domination of diffusion over convection. However, if the characteristic length is increased from one to three centimeter, both processes would have the same rate. The contour plots of the molecular and atomic densities are shown in Fig. 5.8. As can be noticed the density of the atoms (N_{FC}) is around one order smaller, than the density of the molecules. The atoms have the broader distribution over the domain due to the higher diffusion coefficient.

The asymmetric shape of the neutral distribution in Fig.5.8 indicates the interactions of the neutrals with the plasma. Plasma-neutral interactions result in the density source (Sn) and energy sink of plasma (Spe). The neutral sources were described in Section 4.3 but for the sake of convenience they are written here again. The density source is defined by the equation

$$Sn = n_e \left(N_{\text{mol}} \langle\sigma v\rangle_{\text{mol}}^{\text{ion}} + N_{\text{FC}} \langle\sigma v\rangle_{\text{atom}}^{\text{ion}} \right) = Sn_{\text{mol}} + Sn_{\text{FC}}, \quad (5.5)$$

where n_e is the plasma density, N_{mol} and N_{FC} are the densities of molecules and atoms correspondingly, $\langle\sigma v\rangle_{\text{mol}}^{\text{ion}}$ is the reaction rate for the ionization of molecules and $\langle\sigma v\rangle_{\text{atom}}^{\text{ion}}$ is the reaction rate for the ionization of atoms. Although the direct ionization of molecules is a two steps process



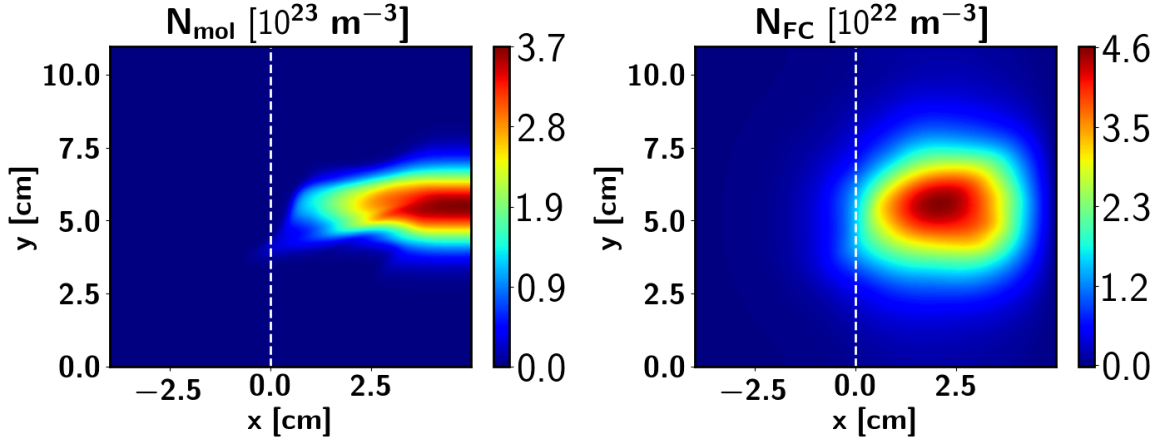


Figure 5.8: Contour plots of the molecular (left) and atomic (right) density for $t = 1.068$ ms. The initial parameters for the simulations correspond to the case *I4* in the Table 5.1.

the dissociation of excited molecules H_2^+ occurs at a high cross-section (Fig. 5.7). For this reason the assumption of an instantaneous dissociation of H_2^+ after its creation is applied in the model. It should be noticed, that the reaction rate for the ionization of atoms



is closed to the reaction rate for the ionization of molecules. Charge exchange reactions are included only in the *nHESEL model* which is discussed in section 5.2.2, while the rest of the thesis presents the results of the SMBI model, which includes only dissociation and ionization of molecules and ionization of atoms. In the *SMBI model* the energy sink is defined by the equation

$$Spe = -\phi_{\text{mol}}^{\text{diss}} n_e N_{\text{mol}} \langle \sigma v \rangle_{\text{mol}}^{\text{diss}} - \phi_{\text{mol}}^{\text{ion}} S n_{\text{mol}} - \phi_{\text{atom}}^{\text{ion}} S n_{\text{FC}} \quad (5.8)$$

where $\phi_{\text{mol}}^{\text{diss}}$, $\phi_{\text{mol}}^{\text{ion}}$, $\phi_{\text{atom}}^{\text{ion}}$ are the reaction potentials [60] for the dissociation of molecules, ionization of molecules and ionization of atoms respectively. The energy sink describes the decrease of the plasma energy due to plasma-neutral interactions. The additional pressure source terms according to the neutral model in [49] are discussed in Section 5.2.2. HESEL model is coupled with the SMBI module through the density source and energy sink terms, which are added to the plasma transport equation. However the results presented in Section 5.2 were performed also without coupling with HESEL and those simulations are refereed as "w/o neutral source".

The density sources created by the molecules, atoms and the total density source are shown in Fig. 5.9. It is seen, that the source from atoms is broader, however the maximum amplitude is almost two times smaller compared to the source from molecules. This is understandable as the density of atoms is lower than the density of molecules (Fig. 5.8). Owing to the higher thermal energy and penetration of atoms closer to LCFS, the density source produced by the ionization of atoms locates deeper inside the plasma compared to the source produced by the ionization of molecules. This emphasise the importance of the inclusion both neutral species in the model. The convective nature of the molecular transport provides the high amplitude localised density source, while the thermal atoms create the broader source and have the high impact to the total source in the edge region.

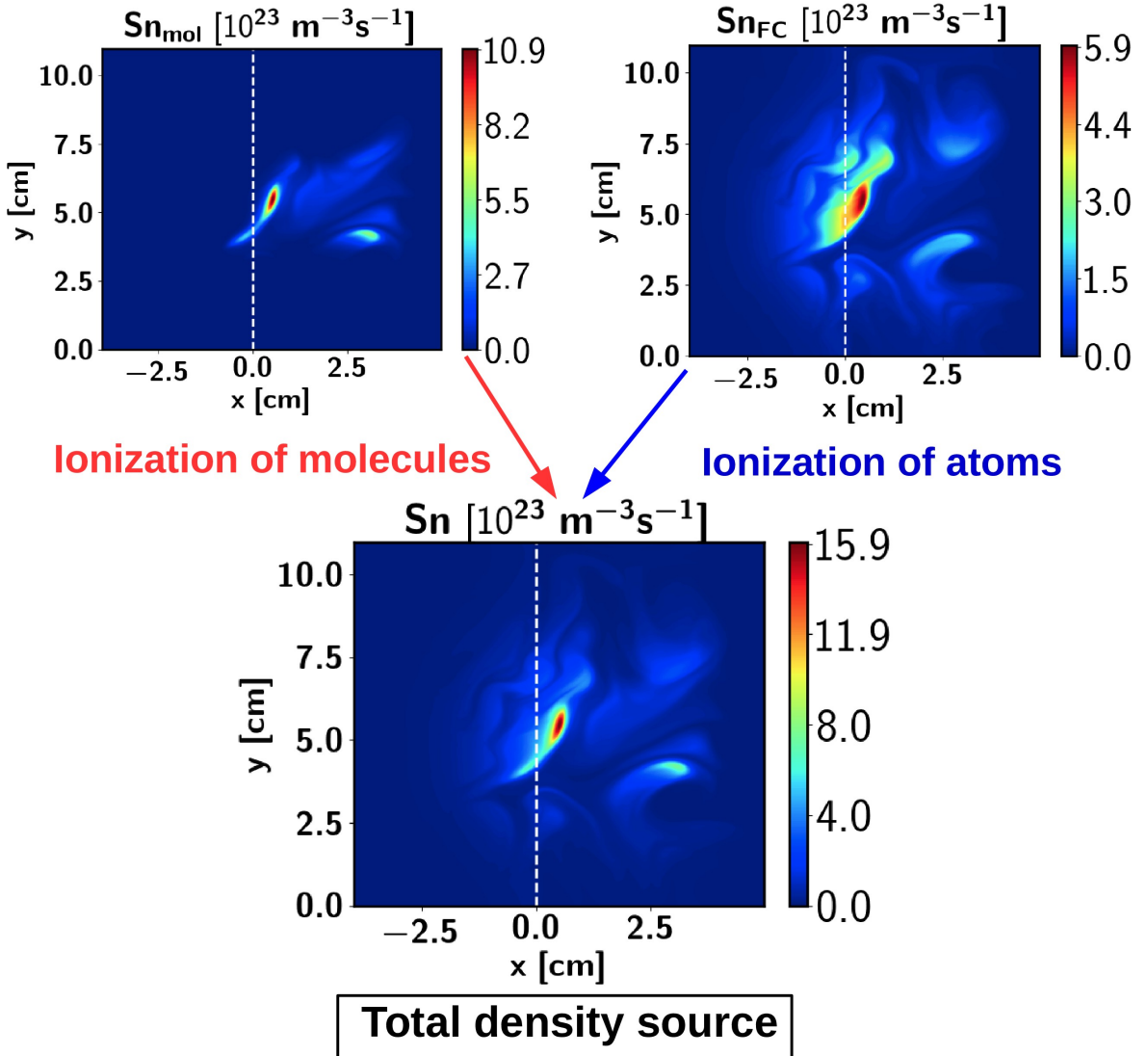


Figure 5.9: The density source produced by the ionization of molecules, ionization of atoms and the total density source for $t = 1.068$ ms. The initial parameters for the simulations correspond to the case I4 in the Table 5.1.

Fig. 5.10 illuminates how the molecular beam and ionization source correlate with the plasma density and temperature fluctuations. The spatial distribution of the molecules is plotted by the black curves on the plasma density contour plot and the labels depict the ratio of the local molecular density to the maximum molecular density. A similar plot is made for the plasma temperature and density source, where the areas enclosed by the black curves correspond to the locations, where the ionization source is higher than 10 % of its maximum. As seen from the figures, the shape of the molecular beam is affected by the spatial structures of the plasma density. The locations of the density source correspond to the spots with high plasma temperatures. Recall, however, that the density source depends on the plasma and neutral density as well.

Although the time frames of the plasma and neutral fields are presented in this section in order to help understanding plasma-neutral interactions in the model, **the temporally averaged plasma and neutral fields are presented hereafter**.

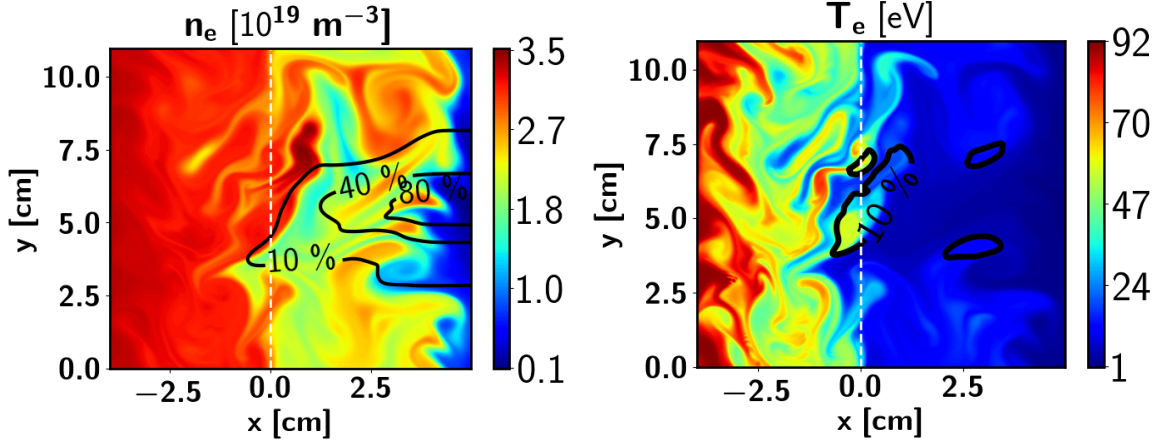


Figure 5.10: On the left: plasma density and molecular beam density with the labels depicting the relative local density of molecules to its maximum value. On the right: electron temperature and areas enclosed by black curves where the density source is higher than 10% of its maximum. Both plots correspond to $t = 1.068$ ms and the initial parameters for the simulations correspond to case *I4* in Table 5.1.

The HESEL model is restricted by the periodic boundary conditions in the poloidal direction. In addition the inward particle transport, which took place in the experiments with SMBI [?], is not included in the model. Therefore HESEL model can not reproduce the influence of SMBI on plasma in tokamak in total, but only the alteration of the plasma properties in the SOL and a few centimeters inside the separatrix. It is not trivial to correctly estimate the fuelling efficiency, i.e. the ratio of the density increment to the number of injected molecules in terms of the HESEL model. **The ionization efficiency** is defined as the ratio of the density source in the edge region to the total density source over the whole domain

$$\eta = \frac{\int_{edge} S_n dx dy dt}{\int_{total} S_n dx dy dt}. \quad (5.9)$$

This is an analogy of the fuelling efficiency and allows an estimation of the feasibility of SMBI to effectively fuel the plasma, if accept the assumption that only the ionization in the edge region can effectively increase the plasma density, while the ionization in the SOL is ineffective due to parallel losses along the open magnetic field lines.

The initial parameters for the HESEL-SMBI simulations are summarized in Table 5.1 and Table 5.2.

study	reference case	N_{mol} [$10^{21} m^{-3}$]	V_{SMBI} [m/s]	w_{beam} [cm]	T_e eV	n_e [$10^{19} m^{-3}$]	q	neutral source
influence of neutral sources	I3	61	1000	2	43	2	5.5	SMBI model
	I3-W	61						w/o source
	I7	335						SMBI model
	I7-W	335						w/o source
	I3-F-CX1	61						nHESEL model $T_{CX} = 10eV$
	I3-FCX2	61						nHESEL model $T_{CX} = 20eV$
beam intensity scan	I1	0.3	1000	2	43	2	5.5	SMBI model
	I2	13						SMBI model
	I3	61						SMBI model
	I4	74						SMBI model
	I5	80						SMBI model
	I6	87						SMBI model
beam intensity q scan	I2-q2	13	1000	2	46	2.2	7.5	SMBI model
	I2-A-q2	33						SMBI model
	I3-q2	61						SMBI model
	I4-q2	74						SMBI model
	I1-q3	0.3	1000	2	38	1.7	3	SMBI model
	I2-q3	13						SMBI model
	I2-B-q3	20						SMBI model
velocity small flux scan	I2-V0	1338	10					
	I2-V1	34	400					
	I2	13	1000					
	I2-V2	6.7	2000	2	43	2	5.5	SMBI model
	I2-V3	3.4	4000					
	I2-V4	1.4	10000					
velocity large flux scan	I4-V0	7400	10					
	I4-V1	185	400					
	I4	74	1000	2	43	2	5.5	SMBI model
	I4-V2	18	4000					
velocity q scan	I4-q2-V1	185	400					
	I4-q2	74	1000	2	46	2.2	7.5	SMBI model
	I4-q2-V2	18	4000					
	I2-B-q3-V1	50	400					
	I2-B-q3	20	1000	2	38	1.7	3	SMBI model
	I2-B-q3-V2	5	4000					

Table 5.1: The initialization parameters of the HESEL-SMBI simulations. T_e and n_e represents plasma temperature and density at the LCFS on the onset of SMBI.

study	reference case	N_{mol} [$10^{21} m^{-3}$]	V_{SMBI} [m/s]	w_{beam} [cm]	T_e eV	n_e [$10^{19} m^{-3}$]	q	neutral source
width small flux scan	I2-NB	13	1000	0.1	43	2	5.5	SMBI model
	I2			2				
	I2-F			11				
width large flux scan	I4-NB	74	1000	0.1	43	2	5.5	SMBI model
	I4			2				
	I4-F			11				
width q scan	I2-B-q3-NB	20	1000	0.1	38	1.7	3	SMBI model
	I2-B-q3			2				
	I2-B-q3-F			11				
width q scan	I4-q2-NB	74	1000	0.1	46	2.2	7.5	SMBI model
	I4-q2			2				
	I4-q2-F			11				

Table 5.2: The initialization parameters of the HESEL-SMBI simulations for the beam width scan. T_e and n_e represents plasma temperature and density at the LCFS on the onset of SMBI.

5.1.3 Outline of the result section

Each section of this Chapter is aimed to answer one of the question raised in the thesis goal in Section 2.3 and approach the understanding of the underlying physics.

Section 5.2 is devoted to discussion of neutral sources. The question "*Can we observe a "self-shielding" effect in the presence of plasma turbulence ?*" is answered by comparison of the models with plasma feedback on neutral injection and without. In addition, the discussion of the neutrals source terms caused by the inelastic plasma -neutral interaction and their influence on the plasma dynamic in a fluid model is presented. Section 5.3 gives the answer to the question "*How the fuelling efficiency depends on the beam velocity, density and width?*". For each scan of parameters the following aspects are discussed

- 1) influence of SMBI on the plasma
- 2) spatial structure of the density source
- 3) scaling of the ionization efficiency on the scanned parameter

In Section 5.4 the influence of SMBI on the plasma turbulence is studied to understand "*Under which conditions turbulence suppression by SMBI can be observed?*". Influence of the beam density, velocity and width variations on the plasma fluctuations is investigated by comparing the reference simulation with the simulations without SMBI and focusing on:

- 1) fluctuation level for plasma density and plasma temperature
- 2) PDF (probability density function) of the plasma density and its statistical moments
- 4) cross correlation of the plasma density and temperature fluctuations
- 5) particle flux across the LCFS
- 6) poloidal velocity profile and velocity shear
- 7) gradient of the ion and electron pressure

The question "*How turbulence affects on the supersonic molecular beam*" is elucidated in Section 5.5. To answer on this question the following steps were done:

- 1) comparison of the dynamic plasma simulations with the mean-field model, where dynamical plasma fields are replaced by their temporal mean values
- 2) analysis of the fluctuation level of the density source

5.2 Influence of neutral sources on the SMB penetration in self-consistent simulations

5.2.1 Investigation of the "self-shielding" effect in simulations with plasma dynamics

As mentioned, plasma-neutral interactions lead to a modification of plasma fields. The density source resulting from ionization of neutrals increases the plasma density while

the plasma temperature drops proportional to the energy required for the dissociation and ionization of molecules and ionization of atoms. Subsequently the lower temperature enhances the probability of neutrals to penetrate deeper into the plasma, while the high density of plasma increases a frequency of plasma-neutral interactions and reduces the penetration depth of neutrals. Since both processes take place at the same time it is essential to understand which of them dominates and determines the penetration of supersonic molecular beam in plasmas.

Earlier research of this question are mentioned in Chapter 2 and the short summary for refreshing is given here. The simulation results on the Tore Supra justified the experimental measurements from the reciprocating probe, which showed the rise of the parallel particle flux and temperature drop at the LCFS during SMBI [18]. According to the 1D plasma simulations with the neutral code EIRENE the ionization source shifted deeper into the plasma in time of the maximum SOL cooling (Fig. 2.4). That indicates the domination of the energy sink, caused by the plasma-neutral interactions on the neutral penetration. On ASDEX Upgrade the so called "self-shielding effect" was found [28]. This effect consists of the formation of the high density plasmoid resulting from the ionization of injected neutrals which blocks the deeper penetration of the molecular beam into the plasma. The creation of the density spike near the separatrix was demonstrated in the simulations with the B2-Eirene code (Fig. 2.5) and measurements of the edge plasma profiles by the Li-beam diagnostic (Fig. 2.6). According to the numerical data [28], the plasma density locally increased in around three times in $16.7 \mu s$ after start of SMBI, while the temperature stayed at the same level as before the neutral injection. This brought to the conclusion about the existence of the "self-shielding effect", which determines the penetration of the dense molecular beam in experiments with SMBI. The later simulations with the *trans-neut module* [32], which self-consistently describes plasma - supersonic molecular beam interactions, showed both effects: the increase of the plasma density and decrease of the temperature in the edge and the SOL regions during the SMBI. The increase of the plasma density over ten times compared to the value before injection leaded to the backward molecular penetration after around 0.1 ms from the start of the neutral injection (Fig. 2.9). This can be considered as an analogy of the self-blocking effect. Therefore the increase of the plasma density plays the main role and stops the molecular beam penetration after several hundred μs after it started.

It should be noticed that none of those simulations included the description of plasma dynamics, which is essential in the analysis of the SOL plasma. Numerical simulations, which includes the particle and energy turbulence transport allows investigation of the local neutral injection in more realistic conditions closer to the experimental situations.

In order to study the influence of neutral sources (Eq. 5.5 and Eq. 5.8) on the supersonic molecular beam penetration within the framework of HESEL-SMBI model, two kinds of simulations are compared, namely the self - consistent simulations of the plasma-beam interactions (which are referred as the "**with neutral source**") and the simulations without plasma response on the neutral injection ("**w/o neutral source**"), i.e with zero terms on the right had side of equations 4.14 -4.15. In other words, the plasma fields in the first kind of simulations are modified by the neutral sources while in the second case the plasma is not affected by neutrals and keeps the dynamic as it was before the neutral injection. In both simulations the neutral beam interacts with the plasma and is subjected to dissociation and ionization processes.

The initial parameters of the simulations are presented in Table 5.1. First consider the cases *I3* and *I3-W*. The time evolution of the averaged plasma fields in the SOL and the edge regions is shown in Fig. 5.11.

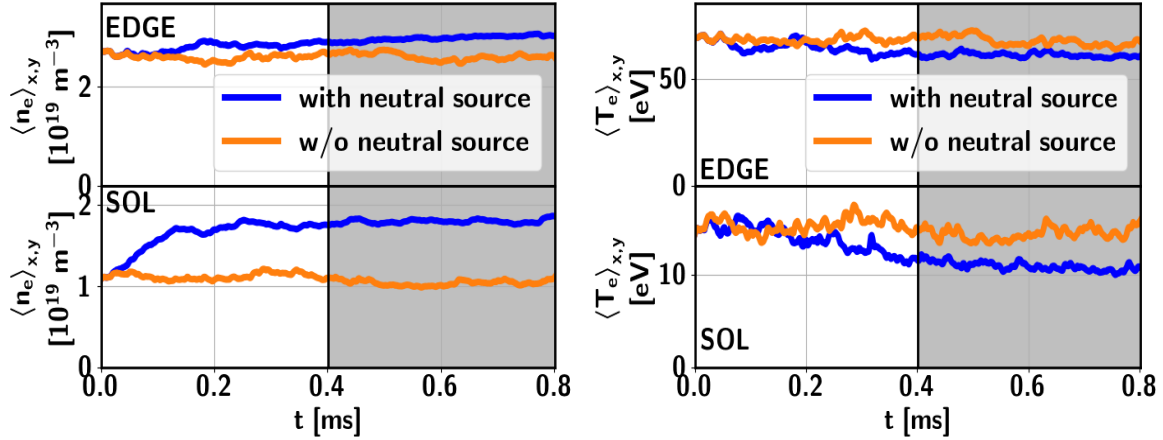


Figure 5.11: The time evolution of the averaged plasma fields during SMBI. The initial parameters correspond to the cases *I3* and *I3-W* in Table 5.1. SMBI starts at $t = 0$ and lasts until the end of simulations. The grey area represents the interval of the time averaging for the data presented in Fig. 5.12 and Fig. 5.14.

Neutral injection starts from $t = 0$ and lasts over the full simulation period. The influence of neutral sources on the plasma density and electron temperature is visible in the simulation "with neutral source". In the considered simulation, neutral injection leads to an increase in the plasma density up to 80 % in the SOL region and up to 20 % in the edge region, while the maximum decrease of the temperature is only 30 % in the SOL and around 10 % in the edge.

The plasma density and temperature averaged in the poloidal direction and temporally over the second part of the simulations (illustrated by the grey area in Fig. 5.11) are shown in Fig. 5.12.

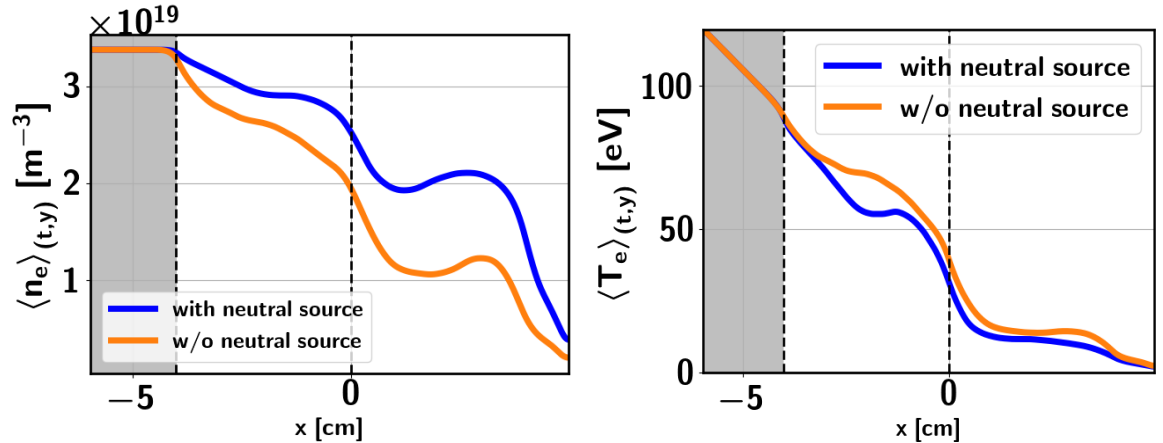


Figure 5.12: The averaged plasma profiles over the statistically steady-state phase of the simulations shown by the grey area in Fig. 5.11. Initial simulation parameters correspond to the cases *I3* and *I3-W* in Table 5.1.

The plasma density increased homogeneously without any pronounced spikes in the profile. 2D plots of the averaged plasma density and temperature show the stronger

decrease of the plasma temperature on the beam propagation front compared to the upper and lower parts of the domain, while the density increased uniformly in the poloidal direction (Fig. 5.13). The higher plasma density in the upper part of the SOL region relates to the filaments transport rather than the ionization of the neutrals, since the concentration of the blobs in those area is observed in the simulations without neutral injection as well (Fig. 5.1).

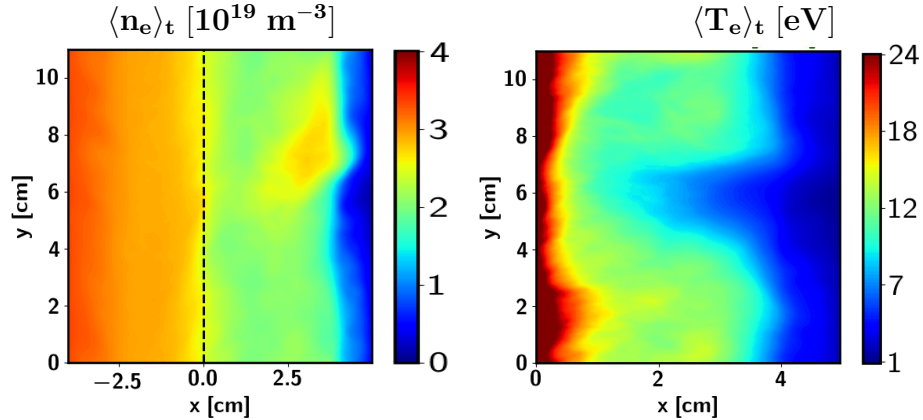


Figure 5.13: The temporally averaged plasma density over the domain and the electron temperature in the SOL region. Initial parameters of simulations correspond to the cases *I3* and *I3-W* in Table 5.1.

The density source profiles (Eq. 5.5) are show in Fig. 5.14. The density source at the LCFS in the simulation where neutrals affect the plasma is almost two times higher compared to the simulation where the influence of neutrals on plasma fields does not included. This indicates that despite the increase in the plasma density, neutral particles penetrate deeper inside the plasma in the former simulation owing to the decrease of the temperature and the subsequent reduction of the frequency of plasma-neutral interactions.

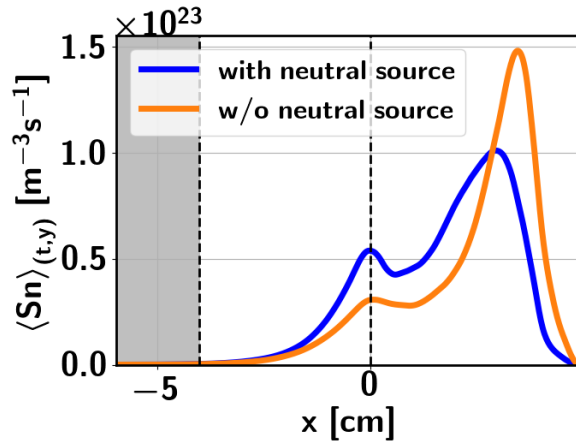


Figure 5.14: The averaged density source profiles. Initial parameters of the simulations correspond to the cases *I3* and *I3-W* in Table 5.1.

The reaction rate coefficients have a nonlinear dependence on the temperature and for the reactions included in the model are shown in Fig. 5.15. The vertical line indicates the averaged SOL temperature before SMBI which is 15 eV. Since the functions

are steeper in the range of 1 - 15 eV, it is understandable why even the relatively small decrease in the electron temperature (from 15 eV to 10 eV) in the SOL region noticeably enhanced the penetration depth of neutrals in the considered simulations. In conditions with higher initial temperature in the SOL, the decrease of the plasma temperature should have weaker influence on the neutral penetration as the dependence of the ionization rates from the temperature is approximately linear in the temperature range of 15-100 eV.

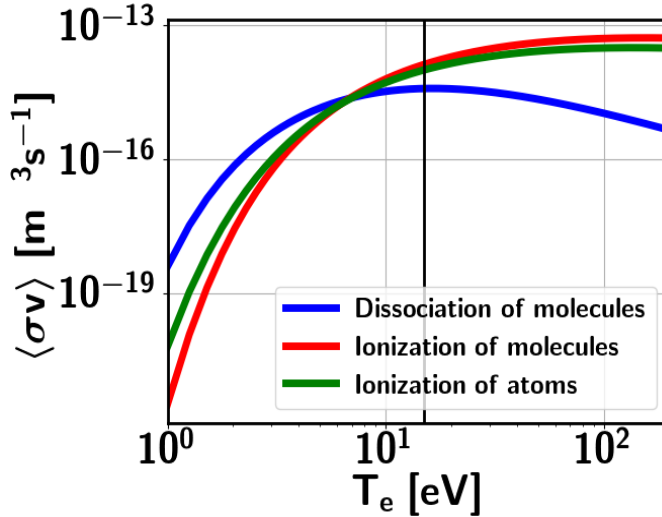


Figure 5.15: Reaction rate coefficients for the reactions included in the model. The vertical line indicates the averaged SOL temperature before SMBI which is equal to 15 eV

The investigation was repeated with the higher neutral density (cases *I7* and *I7-W* in Table 5.1) to check if the "self-shielding effect" takes place for the higher neutral injection rate. Compared to the previous simulations, the neutral density was increased by 5.5 times. This lead to the increase of the averaged plasma density by 320 % in the SOL region and by 160% in the edge, while the averaged temperature decreased by 50 % in the edge region and by 75 % in the SOL. The time evolution and the averaged profiles of the plasma density and electron temperature are shown in Fig. 5.16 and Fig. 5.17. In this simulations the so called "overfuelling" is observed, where the plasma density in the edge region is higher than the prescribed level in the forcing region. This is not a working situation of the HESEL model for the correct description of the plasma turbulence, however the preliminary general understanding of the question: how the strong density source affects on the beam penetration, can be obtained from this simulation. Compared to the previous simulations the higher density increase as well as the stronger reduction of the plasma temperature caused by the neutral injection are observed.

2D plots of the time averaged plasma density and electron temperature in the SOL region are shown in Fig. 5.18 shows the local increase of the plasma density inside the edge region in the poloidal center of the domain.

The density source profiles are shown in Fig. 5.19. As seen from the figure there are pronounced differences between the two simulation and as in the previous case the neutrals penetrate deeper if the plasma feedback on the neutral injection is included in the model. The relative density increase is comparable with the simulation results presented in ASDEX Upgrade (Fig. 2.5), however the strong cooling of the plasma

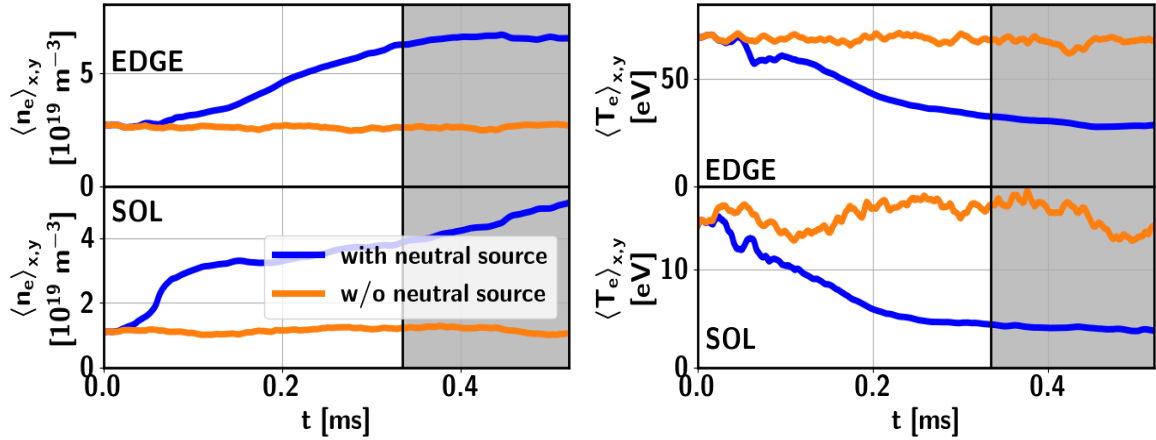


Figure 5.16: The time evolution of the averaged plasma density and electron temperature during SMBI. Initial parameters for the simulations correspond to the cases *I7* and *I7-W* in Table 5.1. SMBI starts at $t = 0$ and lasts until the end of simulations. The grey area represents the interval used for the time averaging for the data presented in Fig. 5.17 and Fig. 5.19.

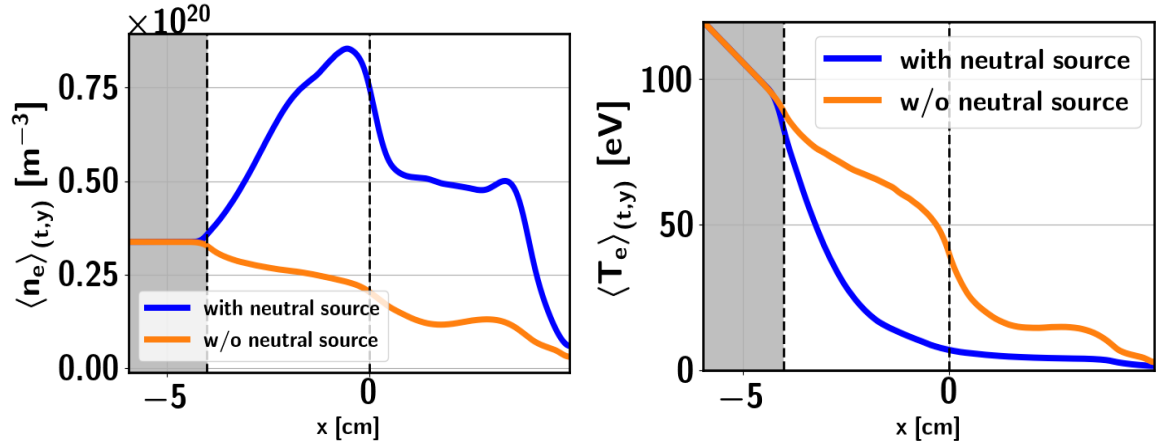


Figure 5.17: The plasma profiles averaged over the statistically steady-state phase of the simulations shown by the grey area in Fig. 5.16. Initial parameters of the simulations correspond to the cases *I7* and *I7-W* in Table 5.1.

is observed in HESEL model. Results obtained with HESEL model are in qualitative agreement with the work [38], where the beam with injection density $1.7 \cdot 10^{21} m^{-3}$ was completely ionized at the separatrix, but without pronounced the "self-shielding" effect. In present simulations the beam density plasma parameters are higher and the beam penetrates only a few centimetres inside the LCFS.

Summary

No self-shielding effect was observed in the simulations with plasma dynamics. Increase of the injection neutral density leads to the stronger decrease of the plasma temperature and consequently deeper penetration of neutrals in plasma.

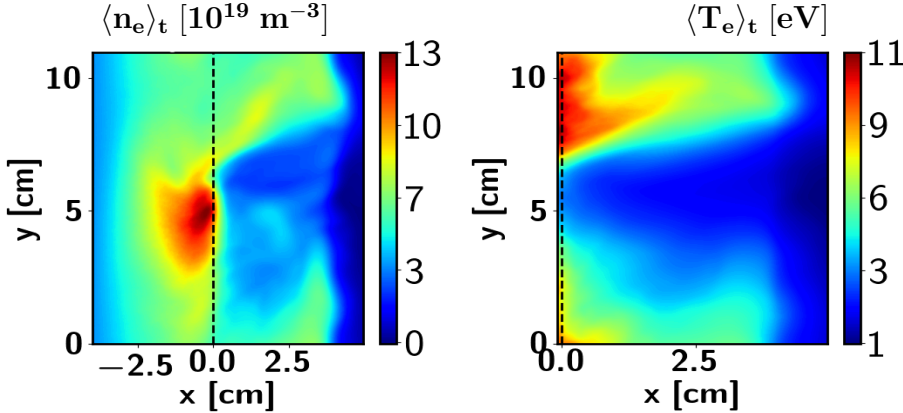


Figure 5.18: The temporally averaged plasma density and electron temperature in the SOL region. Initial parameters of the simulations correspond to the cases *I7* and *I7-W* in Table 5.1

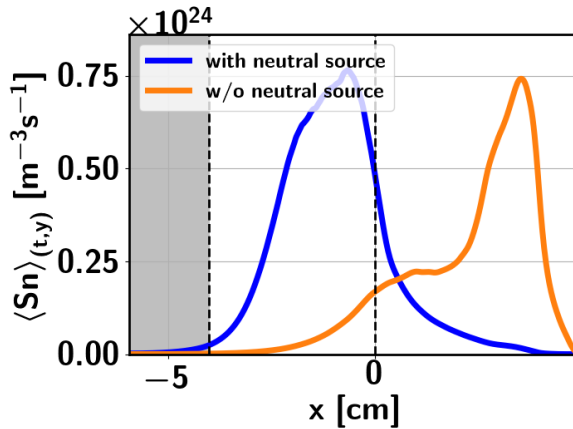


Figure 5.19: The averaged density source profiles. Initial simulation parameters correspond to the cases *I7* and *I7-W* in Table 5.1.

5.2.2 Neutral source terms in a plasma drift-fluid model

The source terms resulting from inelastic neutral-plasma interactions were derived from the Boltzmann equation in [61] and in particular for the coupling with the HESEL model in [49]. The model presented in [49] is referred here as nHESEL model. In order to make the investigation of plasma-supersonic molecular beam interactions and interpretation of results clearer the reduced nHESEL model is used in this thesis. This reduced model is described in Section 4.3 and is referred as SMBI model. In this section the SMBI model is compared with the nHESEL model.

In addition to the density source (Eq. 5.5) and electron pressure sink (Eq. 5.8) the nHESEL model contains the source term for the vorticity, the ion pressure source term and addition terms in the electron pressure source. Moreover, the charge-exchange ions-atoms collisions with corresponding source terms are included in the nHESEL model.

A fluid model requires an additional equation for each species of neutral particle with distinct energy. Only one species of the "hot atoms" [49], which are created by charge-exchange collisions, is included in the nHESEL model. The dynamics of the "hot atoms" (N_{CX}), which for simplicity will be mentioned later as CX atoms, is described by

the diffusion equation

$$\frac{dN_{\text{CX}}}{dt} - \nabla(D_{\text{CX}}\nabla N_{\text{CX}}) = n_e N_{\text{FC}} \langle\sigma v\rangle^{\text{CX}} - n_e N_{\text{CX}} \langle\sigma v\rangle_{\text{atom}}^{\text{ion}}, \quad (5.10)$$

where $\langle\sigma v\rangle^{\text{CX}}$ is the reaction rate for the charge-exchange collisions. The diffusion coefficient is calculated by using Eq. 5.2 with the following parameters: $N_{\text{CX}} = 5 \cdot 10^{19} \text{ m}^{-3}$, $\langle\sigma v\rangle_{\text{CX}} = 10^{-14} \text{ m}^3 \text{s}^{-1}$, $m_{\text{CX}} = 1.6 \cdot 10^{-27} \text{ kg}$. Two simulations with the energy of CX atoms equal to 10 eV and 20 eV are considered in this section. The corresponding diffusion coefficients are $D_{\text{CX}} = 148 \text{ m}^2 \text{s}^{-1}$ and $D_{\text{CX}} = 296 \text{ m}^2 \text{s}^{-1}$. The temperatures of 10 eV and equal to 20 eV are chosen as the characteristic ion temperature in the SOL region, however need to be emphasised, that the decrease of the plasma temperature, caused by SMBI injection can not be included in the dynamics of CX atoms, which have a constant energy.

It is convenient to define the pressure source terms in the nHESEL model as "kinetic" and "thermal" terms. The "thermal" source terms arise from the creation of new ions with the energy equal to the energy of ionized neutral (T_n). According to [49] these terms are written as

$$Spe^{\text{thermal}} = \frac{3}{2} \frac{m_e}{m_n} T_n S_n, \quad (5.11)$$

$$Spi^{\text{thermal}} = \frac{3}{2} \frac{m_i}{m_n} T_n S_n, \quad (5.12)$$

where m_e is the electron mass, m_i is the ion mass, m_n is the mass of neutral.

"Kinetic" pressure source terms are associated with a relative difference in velocity of plasma electrons (\vec{u}_e) and velocity of atoms (\vec{u}_n).

$$Spe^{\text{kinetic}} = \frac{1}{2} m_e (\vec{u}_n - \vec{u}_e)^2 S_n, \quad (5.13)$$

$$Spi^{\text{kinetic}} = \frac{1}{2} m_i (\vec{u}_n - \vec{u}_e)^2 (S_n + S_{\text{cx}}), \quad (5.14)$$

where $S_{\text{cx}} = n_e N_{\text{FC}} \langle\sigma v\rangle^{\text{CX}}$.

As can be noticed this terms have a positive sign. This means that the neutral injection leads to increase of the plasma energy. These terms are obtained in the assumption of the Maxwellian distribution function of injected neutrals. Although these terms are obtained mathematically correct from the Boltzmann equation they reflect the fluid feature of the equations rather than the real physical processes. In addition, the assumption of the Maxwellian distribution function might be irrelevant for the considered collision regime and it might be a reason of the doubtful conclusion of heating the plasma by injecting the cold neutrals [62].

As seen from Eq. 5.13 - 5.14 the "kinetic" terms are proportional to the electron mass for the electron pressure equation and to the ion mass for the ion pressure equation. It is reasonable to expect the small contribution of these terms to the model. The "thermal" terms are proportional to the mass ratio and have a bigger impact compared to the "kinetic" terms. However all of them are smaller than the electron pressure sink term (Eq. 5.8), which is proportional to the density source and the reaction potential (ϕ). Reaction potential is equal to 4.52 eV for the dissociation of molecules, 18.11

eV for the ionization of molecules and 13.6 eV for the ionization of atoms. The energy pressure sink term defines the losses of a plasma energy due to dissociation and ionization processes and has a negative sign.

The ion pressure source term in the nHESEL model has the additional contribution from charge-exchange collisions. This term is expected to be small as it is proportional to the ion mass its expression can be found in [49].

Summing up what has been said, the total source term for the ion and electron pressure in the nHESEL model are written as

$$Spe = Spe^{\text{kinetic}} + Spe^{\text{thermal}} - \phi_{\text{mol}}^{\text{diss}} n_e N_{\text{mol}} \langle \sigma v \rangle_{\text{mol}}^{\text{diss}} - \phi_{\text{mol}}^{\text{ion}} S n_{\text{mol}} - \phi_{\text{atom}}^{\text{ion}} S n_{\text{FC}}, \quad (5.15)$$

$$Spi = Spi^{\text{kinetic}} + Spi^{\text{thermal}} + Si^{CX}, \quad (5.16)$$

The density source $Sn = Sn_{\text{mol}} + Sn_{\text{FC}}$ (5.5) is the same in both models. The coupling of the neutral source terms with the HESEL plasma equations in the SMBI model is described in Section 4.3. For the nHESEL model the same procedure as in [49] is used except the all neutral sources are normalised according to Eq. 4.16 and Eq. 4.17.

The initial simulations parameters are presented in Table 5.1 and correspond to the cases *I3*, *I3-F-CX1*, *I3-F-CX2*. The time signals of the electron pressure source terms are shown in Fig. 5.20. As was expected, the "kinetic" and "thermal" terms are in several orders of magnitude lower compared to the total pressure source term. Due to linear dependence on the energy of atoms, the "thermal" term rises with increase of the energy of CX atoms, while the influence of the energy of atoms on the "kinetic" pressure source term is not so pronounced. All models show the negative value of the total electron pressure source term due to the domination of the energy sink term over the positive "kinetic" and "thermal" terms. The time signals of the ion pressure source terms are shown in Fig. 5.21. The total ion pressure source term has the positive sign since this term does not include the energy losses on the ionization and dissociation of neutrals. The average value of the total ion pressure source term is approximately 50 % smaller than the averaged value of the total electron pressure source term. Since the ion mass is higher compared to the electron mass the "thermal" and "kinetic" terms are bigger for the ion pressure compared to the same terms for the electron pressure. The "thermal" term plays an essential role in the ion pressure source term, while the contribution of the charge-exchange collisions (Fig. 5.22) is around 20% and the contribution of the "kinetic" term is around 2 %.

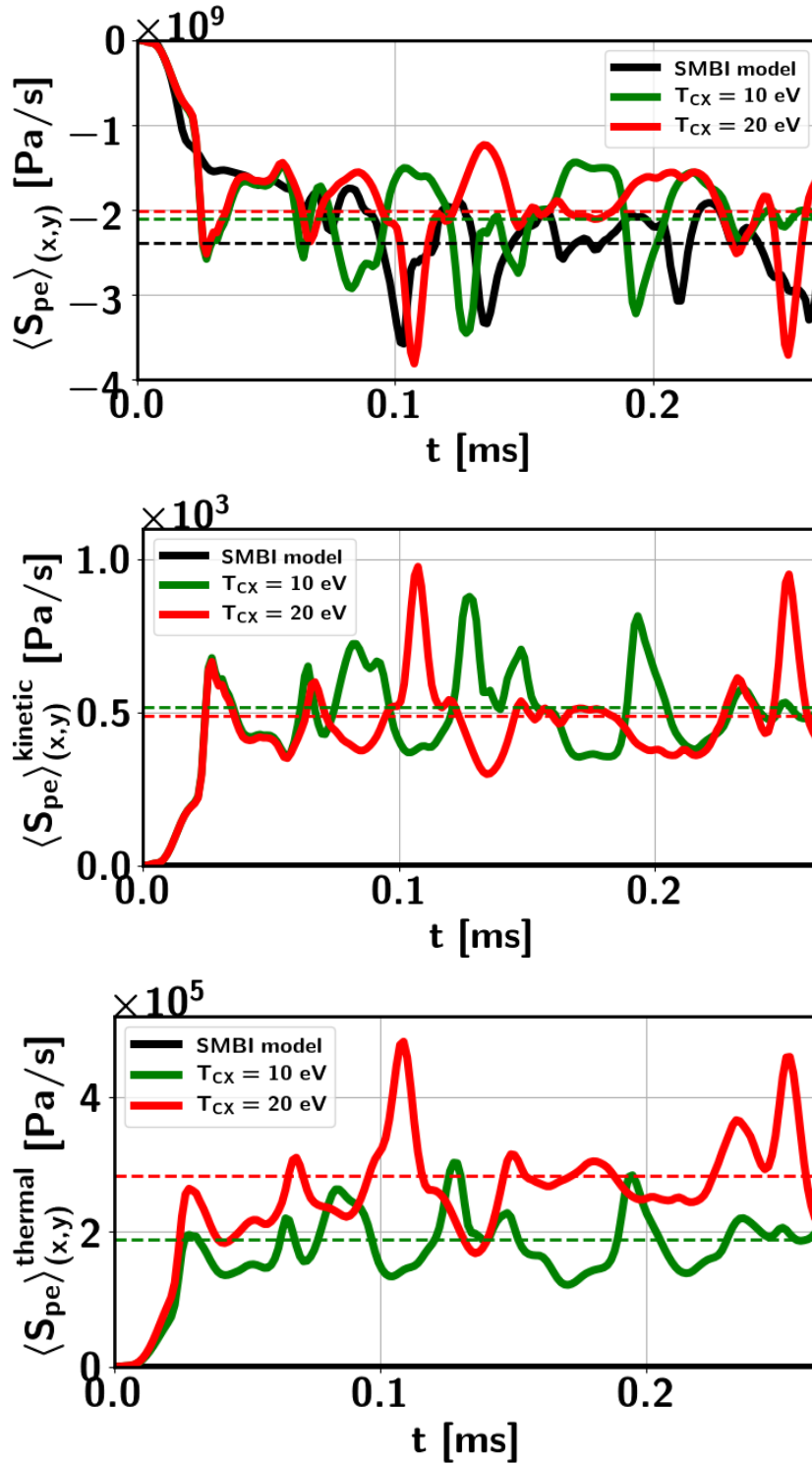


Figure 5.20: The time signal of the averaged total electron pressure source term (top), the "thermal" electron pressure source term (middle) and the "kinetic" electron pressure source term (bottom). Horizontal lines show the time averaged values. Initial parameters correspond to the cases $I3$, $I3\text{-}F\text{-}CX1$, $I3\text{-}F\text{-}CX2$ in Table 5.1.

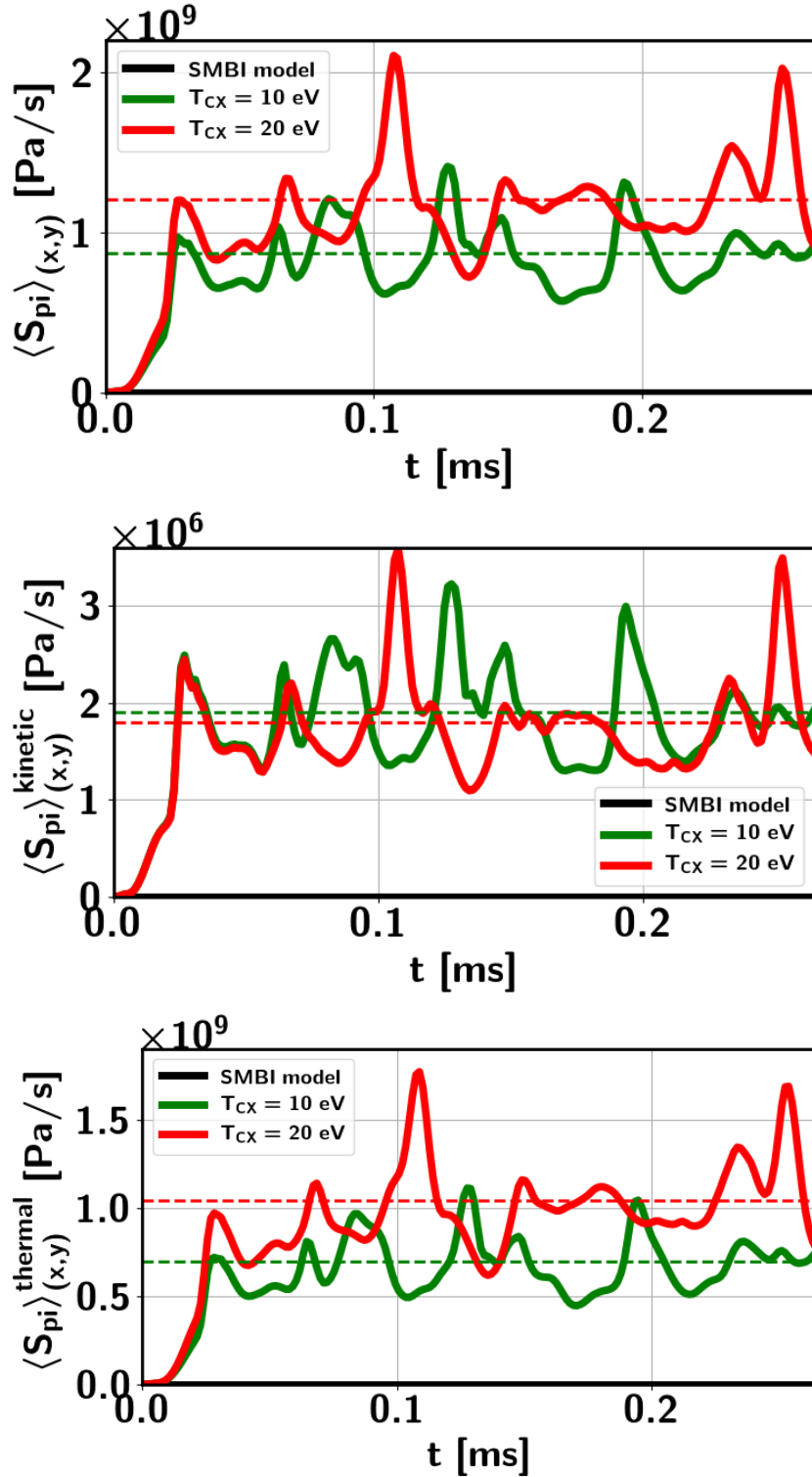


Figure 5.21: The time signal of the averaged total ion pressure source term (on the top), the "thermal" ion pressure source term (middle) and the "kinetic" ion pressure source term (bottom). Horizontal lines show the time averaged values. Initial parameters correspond to the cases I3, I3-F-CX1, I3-F-CX2 in Table 5.1.

The poloidally and temporally averaged profiles of the electron and ion pressure are compared for different models in Fig. 5.23. The profiles obtained by three different models are close to each other for both ion and electron pressures. In order to quantify

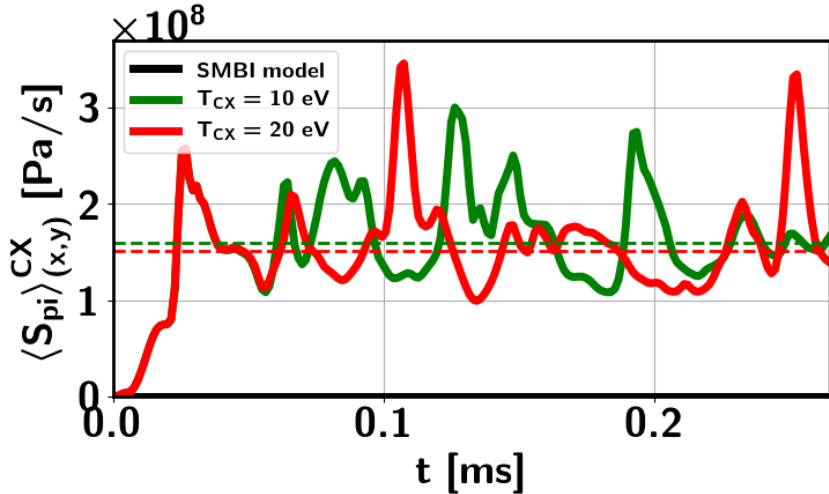


Figure 5.22: The ion pressure source term resulted from the charge-exchange collisions. Horizontal lines show the time averaged values. Initial parameters are the cases *I3*, *I3-F-CX1*, *I3-F-CX2* in Table 5.1.

the difference between the models, the ratio of the profiles obtained with the nHESEL model to the profiles obtained with the SMBI model

$$\delta f = \frac{\langle f \rangle^{nHESEL}}{\langle f \rangle^{SMBI}}. \quad (5.17)$$

is computed. The ratios of the electron and ion pressure profiles are shown in Fig. 5.23. The ratios increase from the edge to the SOL region as the absolute value of the pressure decreases towards the wall. In the edge region the SMBI model gives the same results as the nHESEL with precision over 80 %. The discrepancy between the SMBI model and the nHESEL model is bigger for the ion pressure due to mass dependence of the pressure sources and absence of the energy sink term in the ion pressure equation, which mitigates the impact of the positive pressure source terms in the electron pressure equation.

The similar comparison of the SMBI and the nHESEL models is performed for the plasma temperature (Fig. 5.24) and the plasma density (Fig. 5.25). The plasma temperature demonstrates the similar behavior in the SMBI and the nHESEL models as the plasma pressure. The ratio of the density profiles is comparable with the errors of numerical data (Section 5.1). It should be emphasised, that the difference in plasma profiles between the SMBI and nHESEL models are mostly caused by the "thermal" pressure source term rather than the inclusion of the charge-exchange collisions in the model.

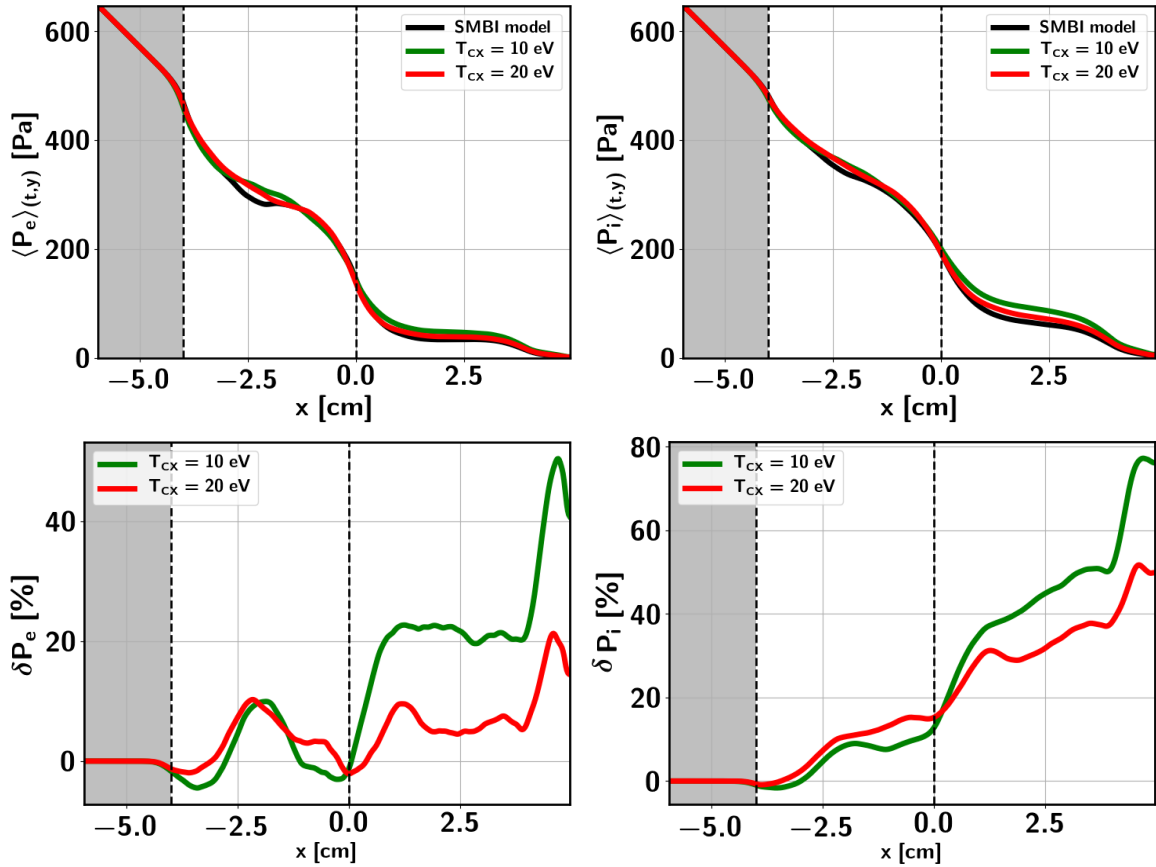


Figure 5.23: Poloidally and time averaged electron pressure and ion pressure profiles for the different models on the top. The ratio of the pressure profiles in the nHESEL model to the profiles in the SMBI model on the bottom. Initial parameters correspond to the cases *I3*, *I3-F-CX1*, *I3-F-CX2* in Table 5.1.

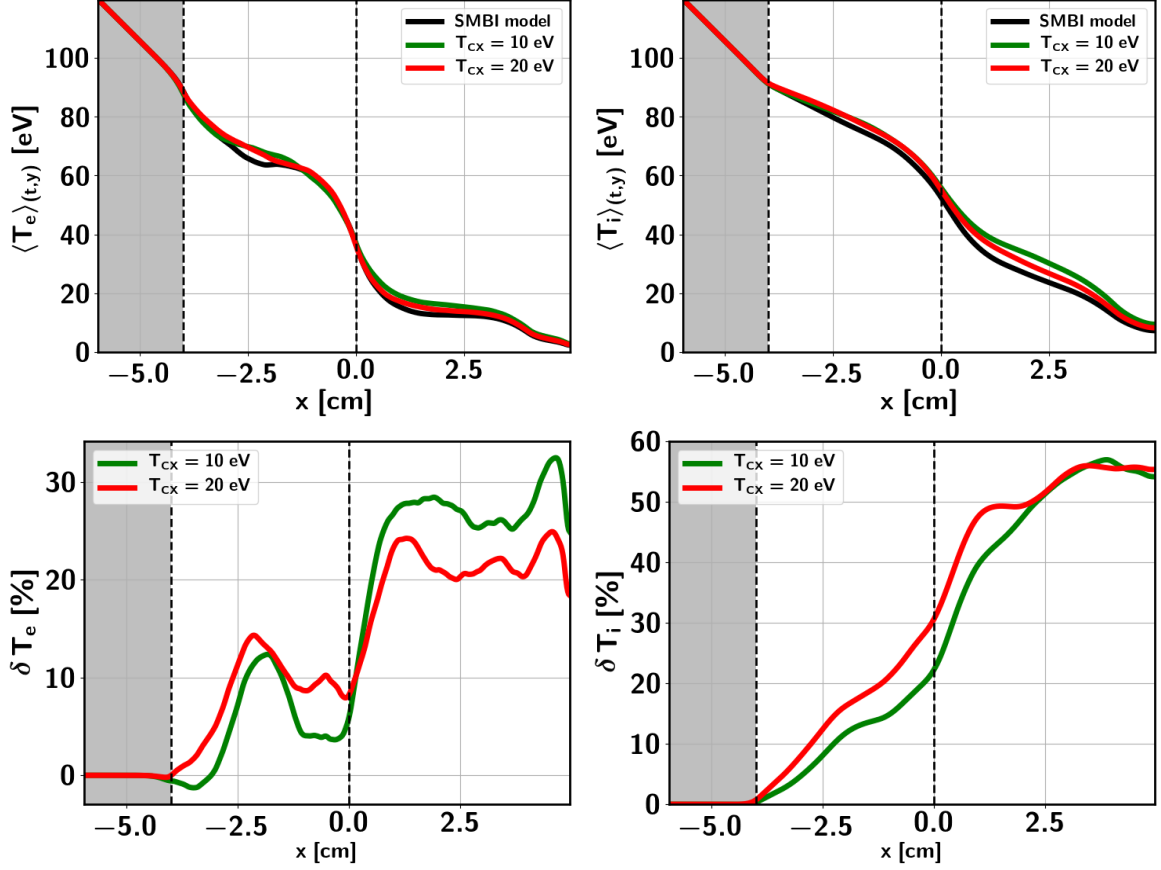


Figure 5.24: Poloidally and temporally averaged electron temperature and ion temperature profiles for the different models on the top. The ratio of the temperature profiles in the nHESEL model to the profiles in the SMBI model on the bottom. Initial parameters correspond to the cases I3, I3-F-CX1, I3-F-CX2 in Table 5.1.

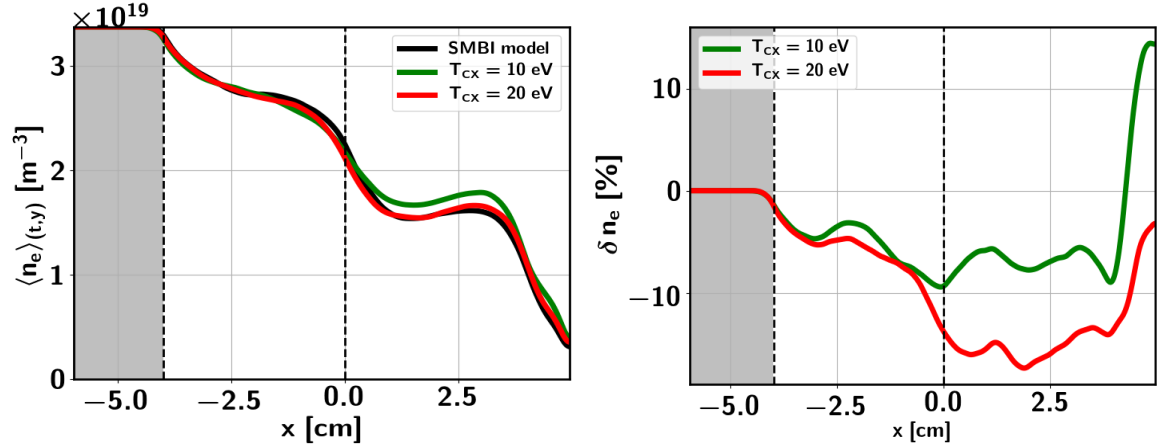


Figure 5.25: Poloidally and temporally averaged plasma density profiles in different models on the left. The ratio of the density profiles in the nHESEL model to the profiles in the SMBI model on the right. Initial parameters correspond to the cases I3, I3-F-CX1, I3-F-CX2 in Table 5.1.

To investigate the influence of the neutral sources on the plasma velocity the radial profiles of the poloidal component of the plasma velocity is shown in Fig. 5.26. The

lower velocity of the plasma in the simulations with the nHESEL model compared to the SMBI model is observed.

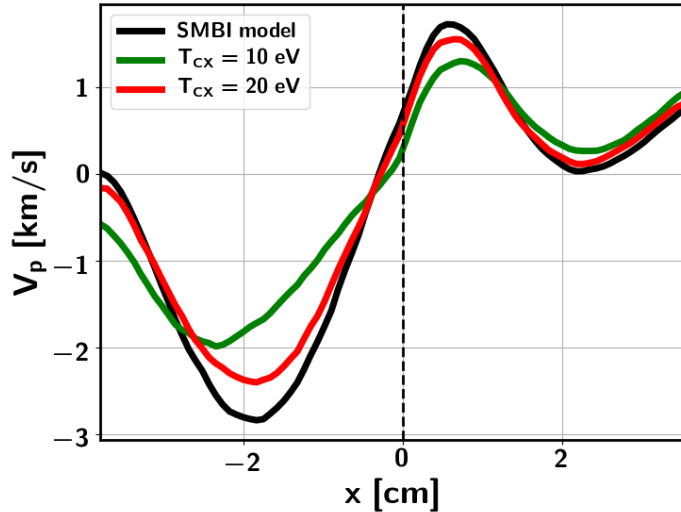


Figure 5.26: The radial profile of the poloidal component of the plasma velocity. Initial parameters correspond to the cases *I3*, *I3-F-CX1*, *I3-F-CX2* in Table 5.1.

The neutral fields from the different models are shown in Fig. 5.27.

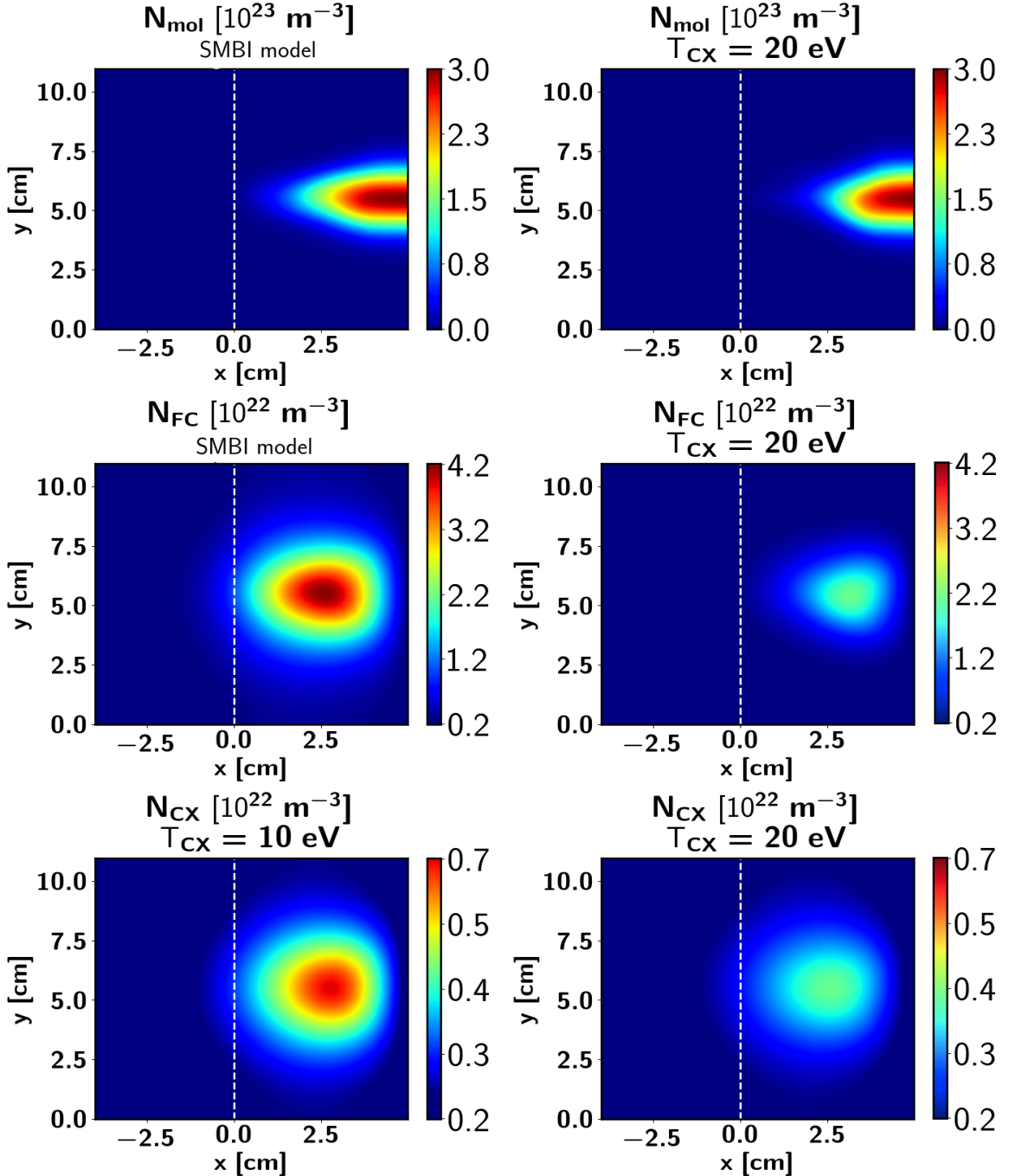


Figure 5.27: Time averaged density of the injected molecules (N_{mol}), Franck-Condon atoms (N_{FC}) and the atoms created by charge-exchange processes (N_{CX}). Initial simulation parameters correspond to the cases I3 and I3-F-CX2 in Table 5.1.

The deeper penetration of the molecules is observed in the simple model (Fig. 5.27 and Fig. 5.29). It is caused by the higher plasma temperature and consequently larger reaction rates of dissociation and ionization of molecules in the full model simulations. As can be seen from Fig. 5.28 the ionization rate in the SOL region is approximately two times higher in the nHESEL model. The density of the Franck-Condon atoms is around two times lower in the nHESEL model than that in the SMBI model (Fig. 5.27 and Fig. 5.29). This again relates with the higher plasma temperature and faster ionization of neutrals in the nHESEL model and with charge-exchange collisions included only

in the nHESEL model. The charge-exchange collisions have much higher reaction rate in the SOL region compared to the reaction rate for ionization (Fig. 5.28.) Despite the higher diffusion coefficient the CX atoms do not penetrate significantly deeper than the Franck-Condon atoms due to their fast ionization. Different densities of CX atoms in two nHESEL models relate with the different plasma conditions caused by self-consistent simulations of plasma-neutral interaction.

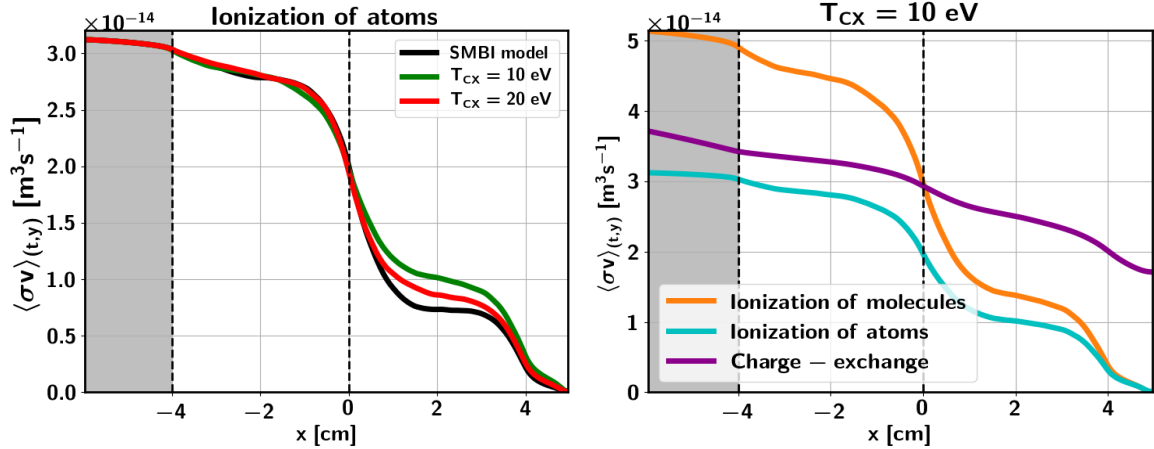


Figure 5.28: Averaged ionization reaction rate compared for different models on the right. Initial parameters for the simulations correspond to the cases $I3$, $I3-F-CX1$, $I3-F-CX2$ in Table 5.1. Averaged radial distributions of reaction rate on the left. Initial parameters for the simulations correspond to the case $I3-F-CX1$ in Table 5.1.

The poloidally and temporally averaged profiles of the molecular and atomic densities are shown in Fig. 5.29. As can be understood from the figure, in the nHESEL model the major part of the density source in the edge region is created by the CX atoms, however their density is much smaller compared to the density of the Franck-Condon atoms in the SMBI model. The time averaged radial profiles of the density source in different models are shown in Fig. 5.30. The time averaged counter plots of the density source produced by ionization of the molecules, by ionization of the Franck-Condon atoms and the total density source are shown in Fig. 5.31. These pictures more clearly demonstrate that neutral particles penetrate deeper into the plasma in the SMBI model and the ionization efficiency in this case higher.

Summary

Comparison of the nHESEL and the SMBI models showed the difference in plasma profiles below the 30% in the edge region. The biggest discrepancy is observed in the ion temperature while the ratio between plasma density profiles in different models is comparable with the errors of numerical data. This difference is caused mostly by the inclusion of the "thermal" term in the ion pressure source in the model rather by the transport of CX atoms. The "thermal" term plays an essential role in the ion pressure source term, while the contribution of the charge-exchange collisions is around 20% and the contribution of the "kinetic" term is around 2 %. As the justification of applying "thermal" neutral pressure source terms in a fluid model is still doubtful the applying of the SMBI model is reasonable as it provides an acceptable results which can be interpreted without contradict to understanding the physical processes behind.

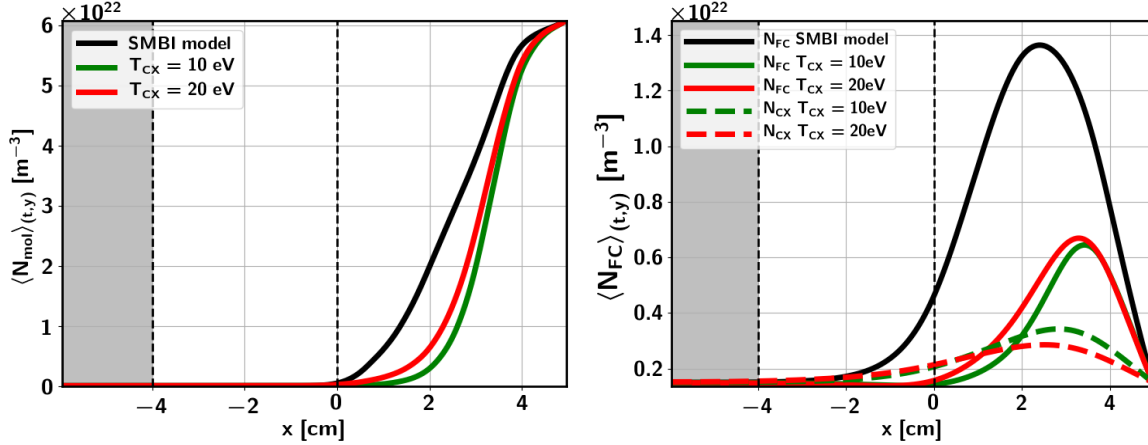


Figure 5.29: Averaged profiles of the injected molecules (left) and atoms (right) compared for different models. Initial simulation parameters correspond to the cases $I3$, $I3\text{-}F\text{-}CX1$, $I3\text{-}F\text{-}CX2$ in Table 5.1.

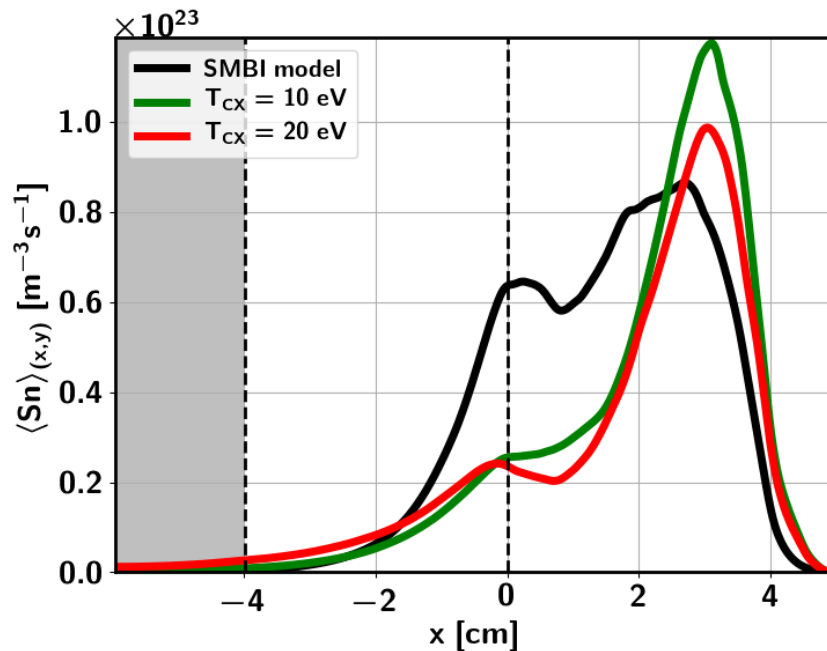


Figure 5.30: Poloidally and time averaged density source profiles in different models. Initial simulation parameters correspond to the cases $I3$, $I3\text{-}F\text{-}CX1$, $I3\text{-}F\text{-}CX2$ in Table 5.1.

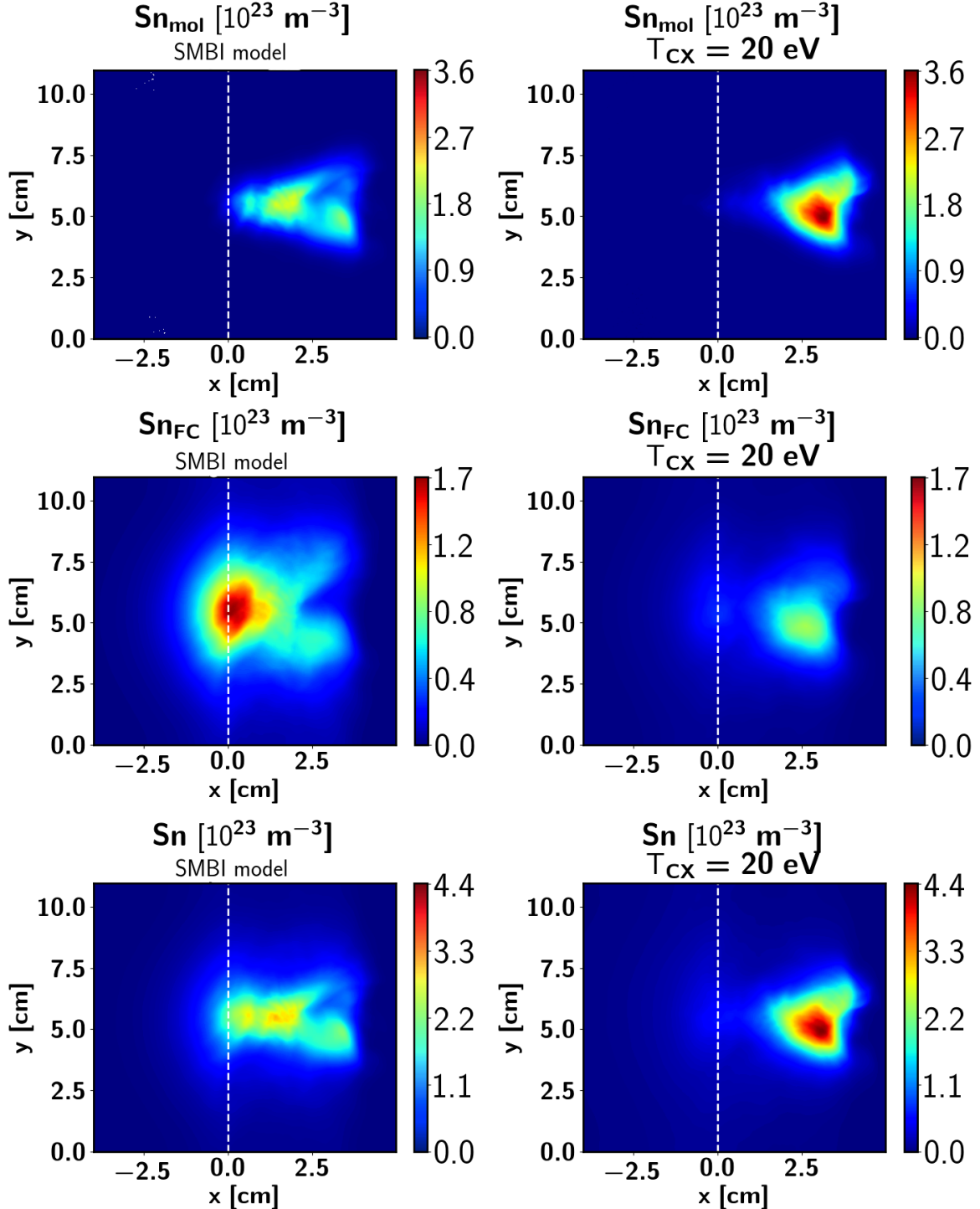


Figure 5.31: Time averaged density source produced by the ionization of molecules (Sn_{mol}), by ionization of Frack-Condon atoms (Sn_{FC}) and the total density source (Sn). Initial parameters correspond to the cases $I3$, $I3-F-CX2$ in Table 5.1.

5.3 Scan of the beam parameters

The scans of the beam parameters, namely the beam intensity, velocity and width are performed to study how ionization efficiency scales with beam parameters. The experimental setup on tokamaks does not have a lot of flexibility to vary parameters of the supersonic molecular beam and numerical simulations are powerful in this situation.

Some features of the supersonic molecular beam are known from the experiments and simulations of SMBI. An enhance of the molecular injection flux achieving by raising of a gas working pressure or by decrease its temperature, increases the fuelling efficiency of SMBI. The scan of the molecular beam intensity was performed on the Tore Supra where a slight increase of the fuelling efficiency with increase of the beam intensity was observed [18]. In Section 3.2 the stronger plasma response on SMBI with the working gas under the low temperature was observed on KSTAR experimental data. Since, these discharges have different plasma conditions before the injection and the proper comparison of two molecular injection rates can not be made. Simulations performed by Rozhansky with the MHD code [38] also pointed on the deeper penetration of the supersonic molecular beam with increase of the beam intensity. However this effect was explained by the protection shielding of the beam core by surrounding neutrals. Simulations performed with the *trans-neut* module [37] showed the deeper dissociation of molecules inside the plasma with increase of the density of the molecular beam. However none of those simulations included the plasma dynamics in the consideration.

It is impossible to perform the scan of the velocity of the molecular beam in experiments. The numerical simulations with the *trans-neut* module [37] demonstrated deeper penetration of neutrals with increase of the beam velocity. However those did not provided any quantitative prediction how the penetration depth of neutrals scales with the injection velocity.

Neither experimental or numerical investigations of the beam size effect on the fuelling characteristics of the supersonic molecular beam have been done so far. Commonly in numerical simulations [32, 36–38] the supersonic molecular beam is initialized in the similar manner as the gas puff injection apart from the existence of the high direct velocity of molecules.

The decrease of the fuelling efficiency with increase of the averaged plasma density was demonstrated in [18, 35]. However, as it is shown in [26] the measuring technique plays an important role. The efficiency was estimated based on the line integration measurements of the plasma density, therefore it does not indicate how many particles were ionized in the SOL region compared to the edge. Numerical simulations provide the distribution of the density source and allows an estimation the ratio of neutrals ionized in SOL and edge region. The scan of the safety factor (q) was performed to study how the penetration of the supersonic molecular beam depends on the plasma conditions. The variation of the safety factor modifies the plasma dynamics and creates new initial plasma conditions for SMBI. The plasma profiles before SMBI are shown in Fig. 5.32. As can be seen the increase of q provides the higher plasma density and temperature. Also should be reminded, that the normalization of the density source is inversely proportional to the safety factor (Eq. 4.17).

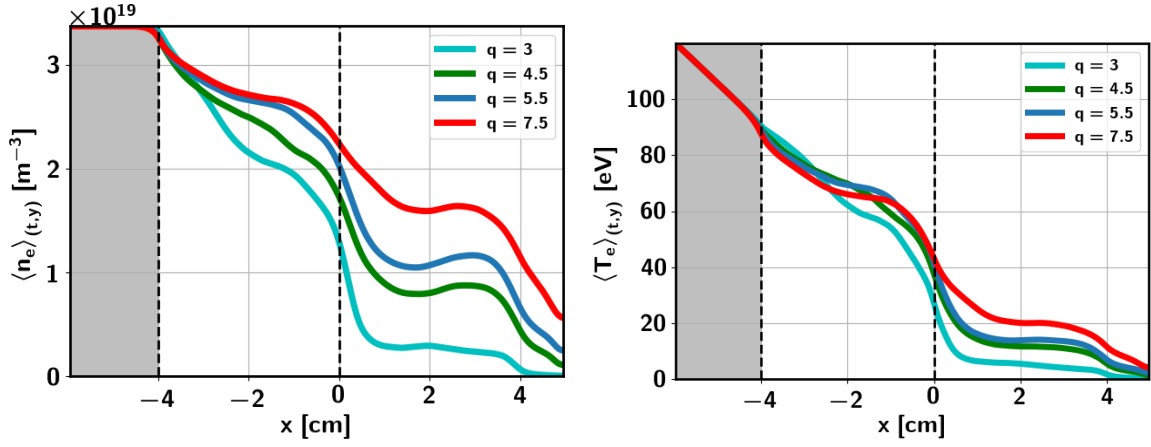


Figure 5.32: Initial plasma profiles before SMBI in simulations with different safety factor (q)

5.3.1 Scan of the beam intensity

The first scan is the scan of the beam intensity. The initial parameters of simulations are summarized in Table 5.1 and correspond to the cases *I1 - I2-B-q3*.

Influence of SMBI on plasma profiles

An influence of SMBI on plasma results in a higher averaged plasma density and lower averaged plasma temperature. The temporally and poloidally averaged profiles of plasma fields are shown in Fig. 5.33. Since the amplitude of the neutral source grows with increase of the amount of injected particles, the influence of neutral injection on plasma becomes more pronounced with increase of the neutral beam intensity. In order to quantify the influence of SMBI on the plasma, the deviation of the averaged plasma fields after injection ($\langle f^{SMBI} \rangle_{(y,t)}$) from the averaged values in reference simulation without injection ($\langle f^{w/o} \rangle_{(y,t)}$) is calculated as

$$\Delta f = \int \frac{(\langle f^{w/o} \rangle_{(y,t)} - \langle f^{SMBI} \rangle_{(y,t)})}{\langle f^{w/o} \rangle_{(y,t)}} dx. \quad (5.18)$$

is investigated as a function of the molecular beam intensity. The results are shown in Fig. 5.34.

Neutral injection into the plasma with high temperature and density results in smaller deviation of plasma profiles from the reference simulation. In lower plasma conditions the deviation of the plasma density grows faster with increase of the molecular injection density. In the edge region the dependence from the molecular density is stronger, as the plasma is confined in this region unlike the SOL region where the part of the ionized particles is lost due to parallel motion along the open magnetic field lines. Independence of the electron temperature in the SOL region from the injection density in simulation with $q=3$ is explained by the already low initial electron temperature before the injection. This is similar to experimental results on the Tore Supra where the decrease of the plasma temperature did not depend on the amount of injected particles. [27]. The reduction of the ion temperature is bigger compared to the electron temperature, what might be explained by the slower ion heat transport.

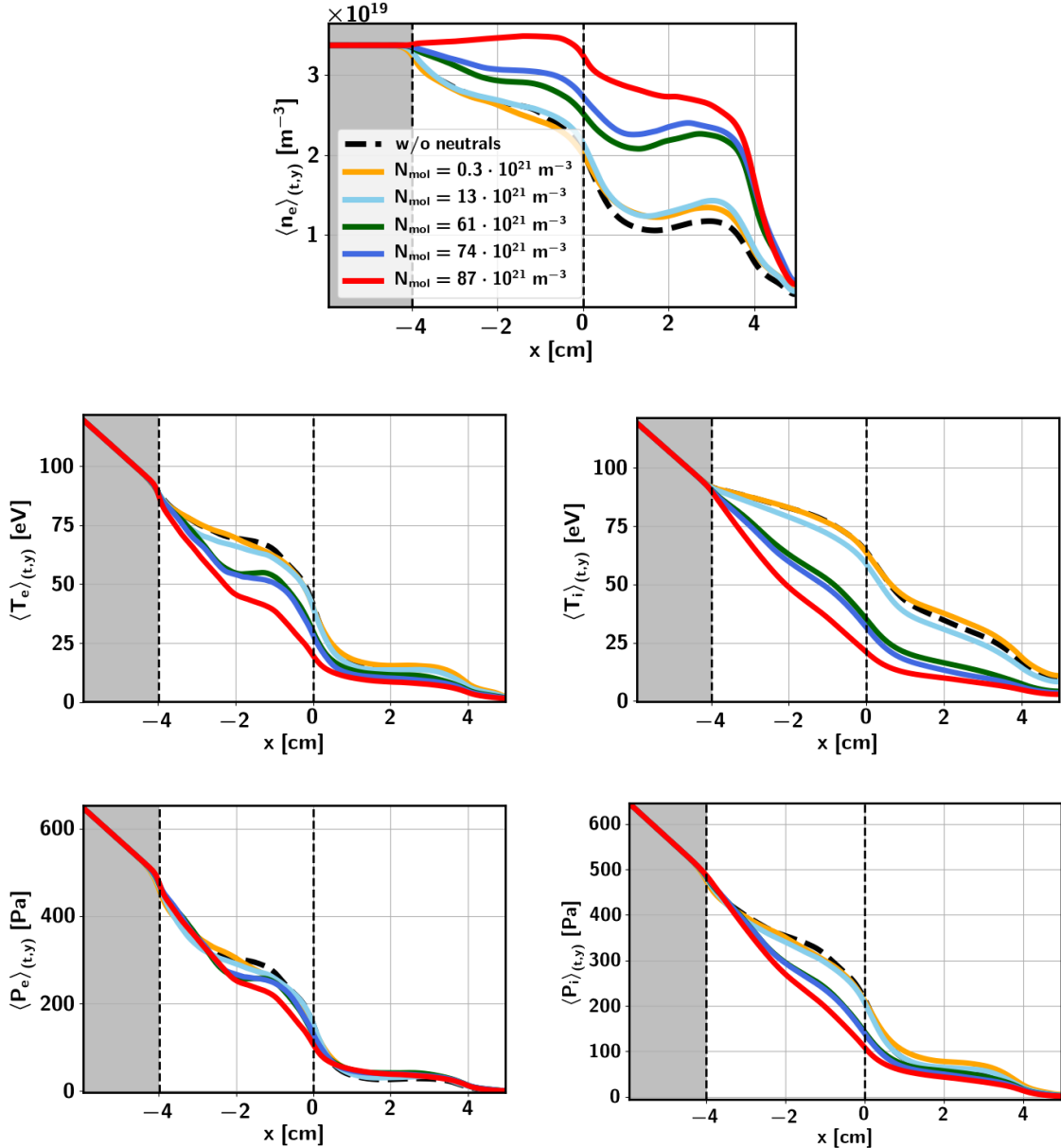


Figure 5.33: Poloidally and temporally averaged plasma profiles for different neutral injection rates. Initial simulation parameters correspond to the cases I1-I7 in Table 5.1

The influence on the pressure is defined by the ratio of density increment and temperature decrease. As can be seen from Fig. 5.33 the electron plasma pressure decreased after SMBI in the edge and increased in the SOL. With the higher neutral injection rate the electron plasma pressure decreased by 20 % in the edge and by increased by 40% in the SOL. With the same neutral injection rate the ion pressure decreased by 40 % in the SOL and decreased by 30% in the edge.

2D plots of the temporally averaged electron temperature in the SOL region show the decrease of plasma temperature on the neutral beam penetration front (Fig. ??). This effect does not observed for the beams with intensity smaller than $N_{mol} = 61 \cdot 10^{21} m^{-3}$. This indicates that the neutral density should be high enough to provide the "stable" decrease of the plasma temperature in the SOL region. In other words the energy required for ionization and dissociation of neutral particles should exceed

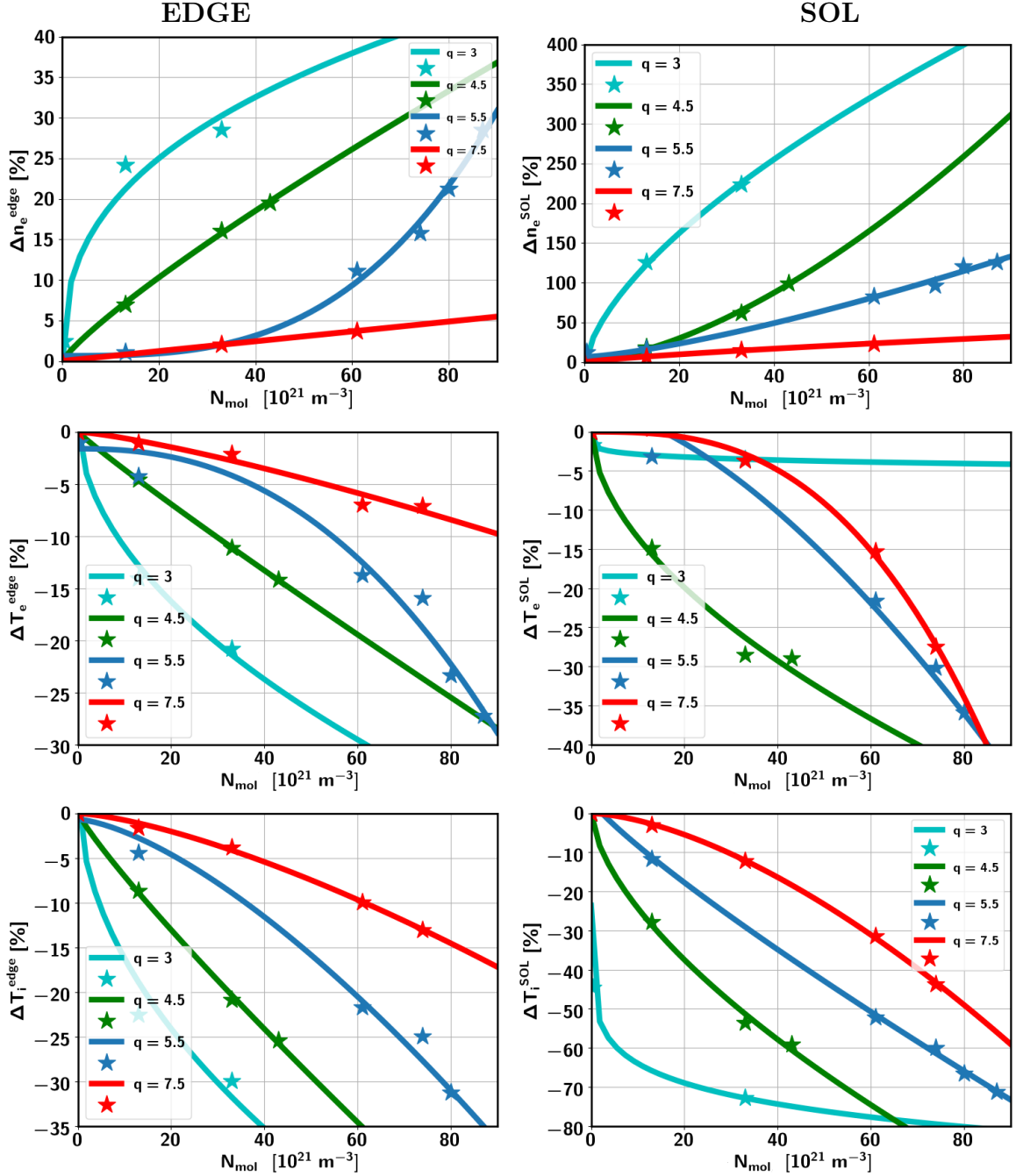


Figure 5.34: Plasma density increment and plasma temperature decrease as functions of the neutral beam intensity. Initial simulation parameters correspond to the cases *I1-I2-B-q3* in Table 5.1

the plasma energy flux from the edge region. The "hole" in the plasma temperature field is observed only in the SOL region, however the averaged decrease of the plasma temperature in the edge region takes place with neutral beam injection higher of $N_{mol} = 61 \cdot 10^{21} m^{-3}$. With higher neutral injection rate and stronger density source at the edge the poloidally localized decrease of temperature in the edge region can be expected. The plots of temporally averaged electron density demonstrate the homogeneous increase of plasma density without pronounced density peaks, except the increase of the plasma density in the poloidal center of the domain in few cm inside the edge in case of the

higher neutral injection rate.

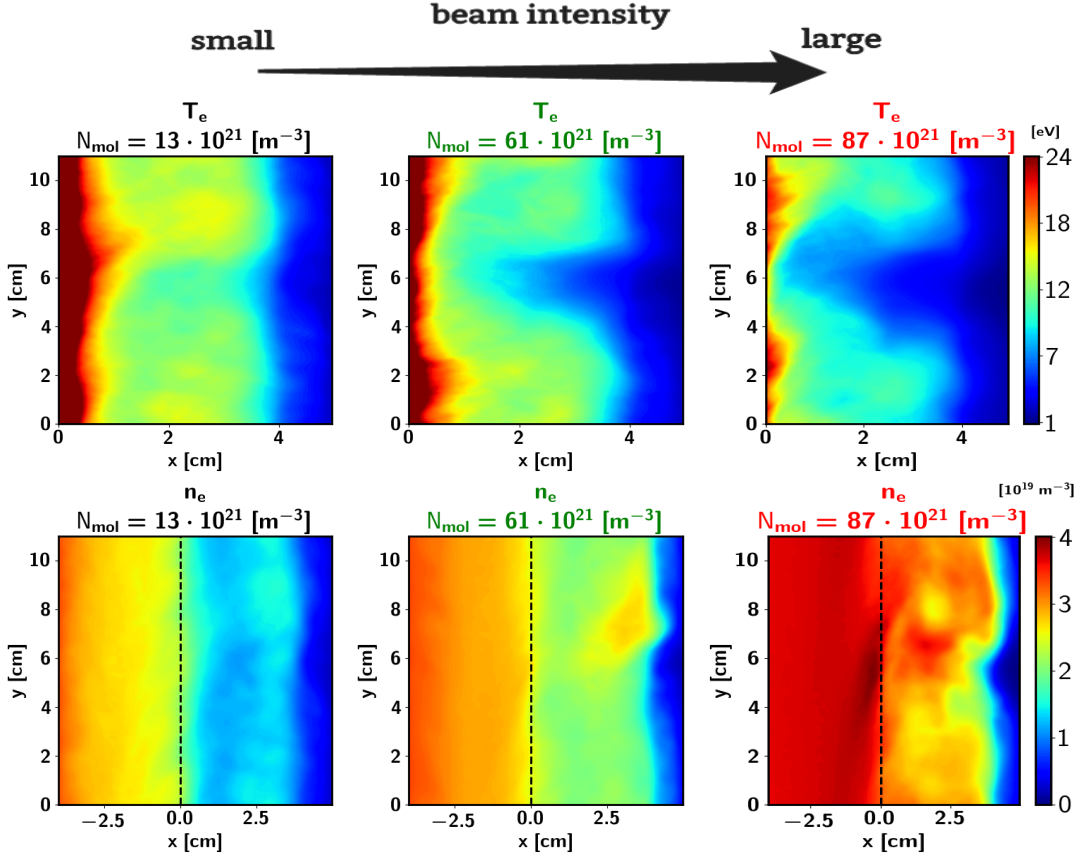


Figure 5.35: First row: temporally averaged electron temperature in the SOL region. Second row: temporally averaged plasma density. Initial simulation parameters correspond to the cases *I2*, *I3* and *I6* in Table 5.1.

Neutral penetration and density source

Density source S_n (Eq.4.14) is a good indication of the neutral penetration, as it demonstrates the location of creation of new ions, i.e. location of a fuelling. In order to estimate the penetration depth of neutral particles depends on the injection density, the 2D plots of the time averaged molecular density, atomic density and the density source are shown in Fig. 5.36 for different injection rates. For the convenience of comparison of the spatial distributions each field is normalized on its maximum. As can be seen the molecules and atoms penetrate deeper with increase of the injection intensity. Over the value " $N_{mol} = 61 \cdot 10^{21} m^{-3}$ " the increase in the penetration depth becomes more pronounced with increase of the molecular density. Density source shifts toward the LCFS with increase of the injection intensity. This is can be explained by the low temperature of plasma (Fig. 5.35) and consequently smaller ionization rates.

The density source profiles averaged in time and poloidal direction are presented in Fig.5.37. The amplitude of the density source and the amount of ionization happening in the edge region grows with the beam intensity. This result is similar to observed in simulations of GP injection in [49]. As was explained in Section 5.1.2 the density source is produced by ionization of molecules and atoms. The profiles of the density sources produced by molecules and atoms are shown in Fig. 5.37. For all injection

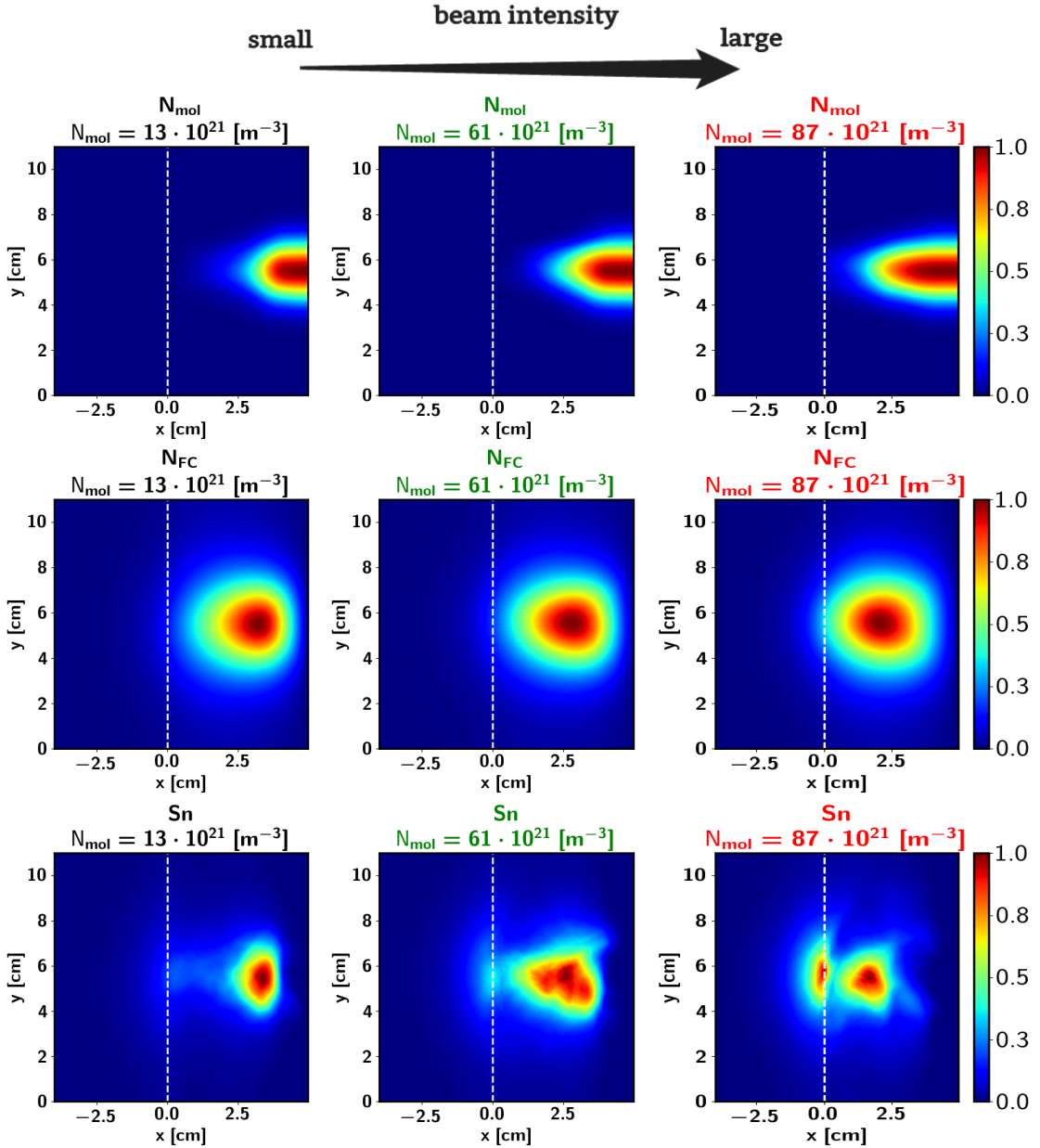


Figure 5.36: Time averaged molecular density (N_{mol}), density of atoms (N_{FC}) and density source(Sn). Each field is normalized on its maximum. Initial simulation parameters correspond to the cases *I2*, *I3* and *I6* in Table 5.1.

rates the density source in the edge region is created mostly by the atoms rather than by the molecules. However, the ratio of the molecules to atoms at the edge region is not a constant and increases with the intensity of the beam. The decrease of the plasma temperature reduces reaction rates and more neutral particles, both molecules and atoms, penetrate in the edge region.

To estimate the density source compared to the plasma the following comparisons are performed. First the density source is compared with advection particle losses along the open magnetic field lines in the SOL region. The parallel advection of particles in

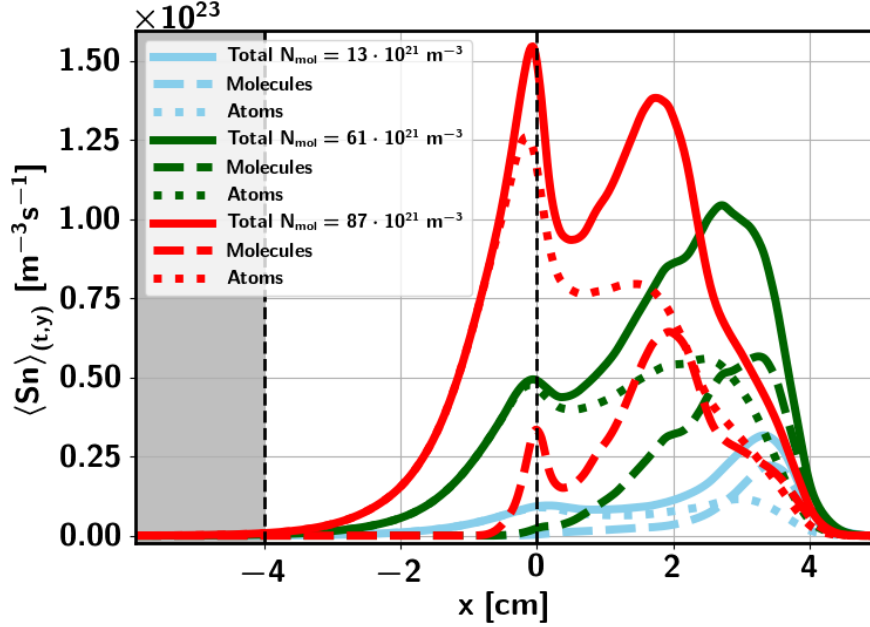


Figure 5.37: Averaged density source profiles for different injection rates. Contributions of the molecules and atoms to the total density source are shown by the dashed and dotted lines respectively. Initial simulation parameters correspond to the cases I2, I3 and I6 in Table 5.1.

the HESEL model is defined by the damping rate

$$\tau_n^{-1} = \frac{2M\sqrt{\frac{T_e+T_i}{m_i}}}{qR}. \quad (5.19)$$

The Mach number $M = u_{||i}/c_s$ is defined through the ion sound speed and ion parallel velocity and is taken as a constant in the model $M = 0.5$. The safety factor q and the major R radius are constant as well, while the electron temperature and ion temperatures are altered by the neutral injection. The reduced temperature after the neutral injection increases a particle life time in the SOL region. The reduction of plasma temperature by 50 % corresponds to decrease of the damping term by approximately 7 %. HESEL model contains three regions (Fig. 4.1), namely the edge, SOL and wall regions. The transition between them is set by the smooth step function

$$\sigma(x) = \frac{\sigma_s}{2} \left[(1 + \tanh(\frac{x - x_s}{\delta_s})) \right], \quad (5.20)$$

where δ_s is the width of the region and σ_s is the numerical factor. The numerical factor is equal to zero in the edge region and is equal to one in the SOL region. To satisfy the boundary conditions and reduce the particle fluxes to the wall, eight times higher damping coefficient is set in the wall region which is the last centimeter of the domain. Therefore particle sink is stronger in the wall region. Particle sink is defined by equation

$$S_{||} = -\sigma(x) \cdot \frac{n_e}{\tau_n}. \quad (5.21)$$

The poloidaly and temporally averaged sink for the reference simulation without neutral source and $q = 5.5$ is shown in Fig. 5.38.

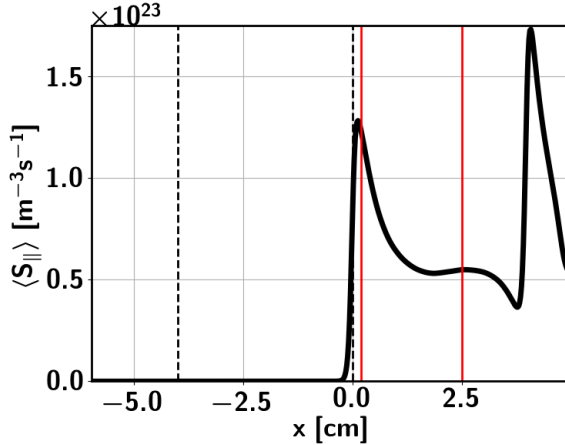


Figure 5.38: Poloidally and time averaged particle sink due to advection motion along the open magnetic field lines. Correspond to the reference simulation without neutral injection and $q=5.5$. The red lines mark the radial positions where the particle sink is compared with the density source in Fig. 5.39

In simulations with neutral injection the plasma density profile in SOL region is determined by the balance of the turbulent particle flux from the plasma edge, parallel particle flux along the open magnetic field lines and by the density source. Therefore even if the density source is smaller than the particle sink the increase of the plasma density in the SOL region will be observed. As seen from comparison of the averaged density source (Fig. 5.37) and particle sink (Fig. 5.38) profiles they are in the same order of magnitude. For more precise analysis the density source and particle sink are compared only in the poloidal center of the domain, where the density source has the maximum value. Comparison is done in two radial positions marked by the red lines in Fig. 5.38. As seen in Fig. 5.39 in the middle of the SOL region ($x = 2.5$ cm) all considered injection rates are higher or in the same order of magnitude with the particle sink. Close to the LCFS only the source produced by the highest neutral injection $N_{mol} = 87 \cdot 10^{21} m^{-3}$ exceeds the particle sink.

Another comparison is the comparison of the integrated density source in the edge region with the density source of the HESEL model. In the HESEL model the plasma density source is set by the forcing in the innermost part of the domain. This source is defined through the fixed density profile (n_{fixed}) and the relaxation time (τ). The forcing is required in the HESEL model to provide the approximation to the core region which acts as the constant source of particles and energy in real experimental situation. The compared quantities are

$$\text{Forcing} = \int_{edge} \frac{(n_{fixed} - n)}{\tau} dx dy, \quad (5.22)$$

$$\text{Fueling} = \int_{edge} S_n dx dy. \quad (5.23)$$

shown in Fig. 5.40. As can be seen the fuelling produced by injection of the neutral beam with density $N_{mol} = 61 \cdot 10^{21} m^{-3}$ is comparable with the forcing. This density is defined as the "**critical density**". Neutral injection below the critical density provides the density source much smaller compared to the plasma source and particle sink in the SOL region. In [60] the possibility of replacement the force profile by the density source

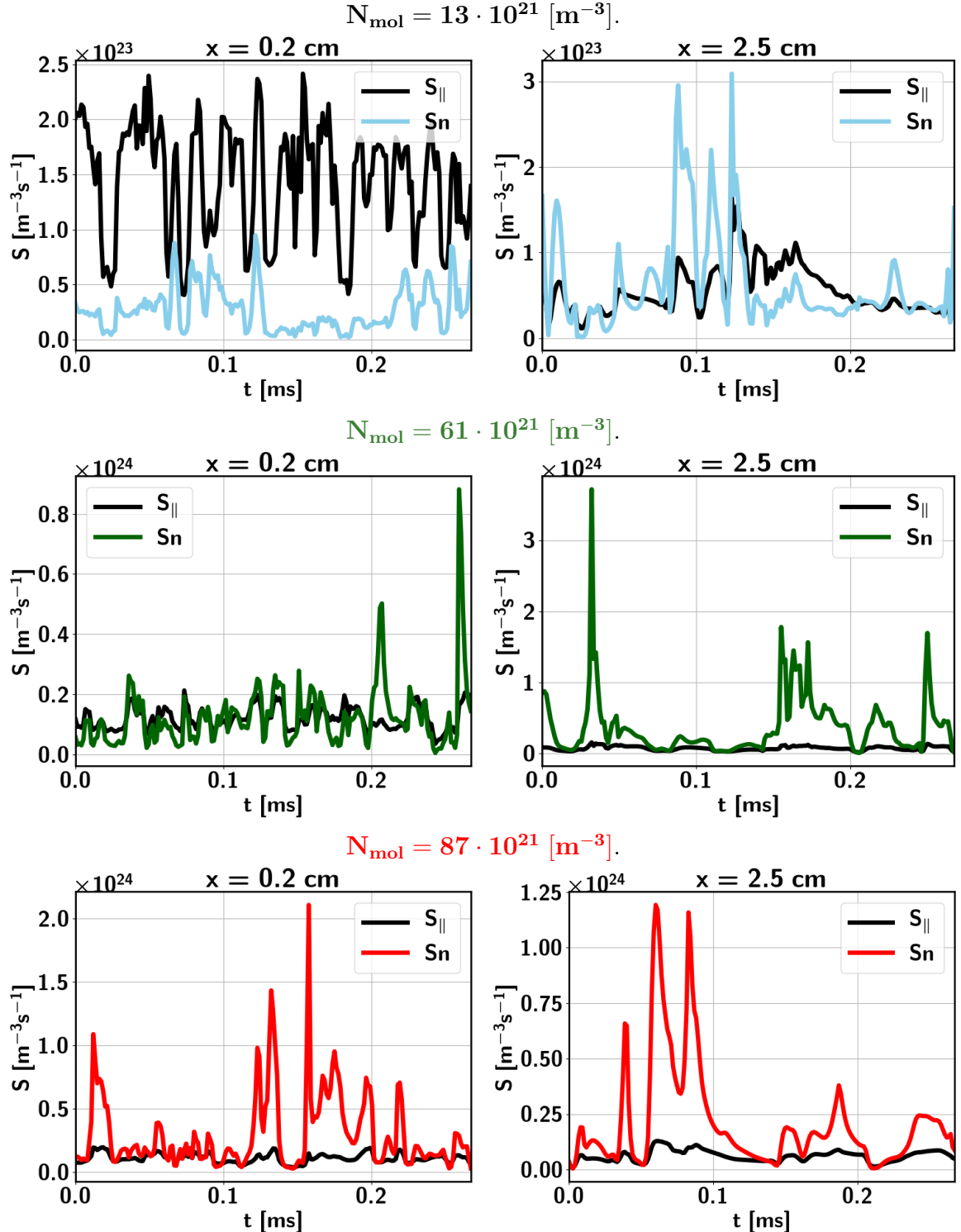


Figure 5.39: Comparison of the density source (Sn) with the particle sink ($S_{||}$) in the SOL region. Initial simulation parameters correspond to the cases $I2$, $I3$ and $I6$ in Table 5.1.

produced by ionization of neutrals was demonstrated. Such simulations are beneficial in terms of the analogy with the real experiments where the plasma density source is caused by the ionization of neutrals. However the removing of forcing is not available for the SMBI simulations as the density source does not evenly distributed across the plasma surface.

The difficulties in making the prediction of the amount of density source in the edge region is due to dependence of the neutral penetration on the SOL conditions. These conditions are defined by the plasma profiles at the edge which are on the other hand is modified by the neutral injection. Therefore the self-consistent simulations are essential for the reliable estimation of the density source in the edge region. As can be seen from Fig. ?? the same injection density produces different ratio of the forcing to fuelling rate in the simulations with different q .

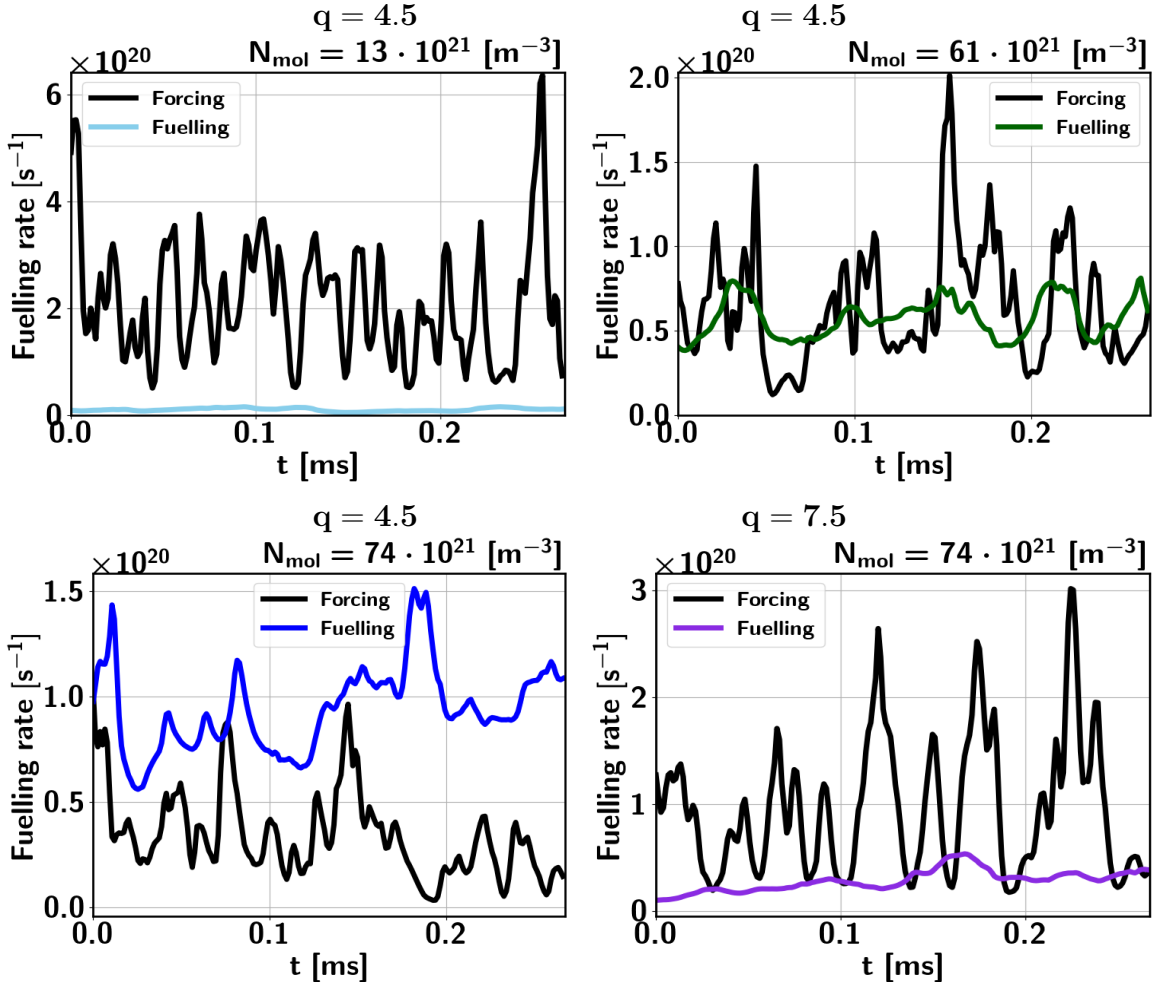


Figure 5.40: Comparison of the forced density source (forcing) and density source produced by ionization neutrals. Initial simulation parameters correspond to the cases *I2* - *I4* and *I4-q2* in Table 5.1.

Approximation of density source as function of the beam intensity

Scaling of the ionization efficiency as a function of a beam intensity is shown in Fig. 5.41. As can be seen there are no universal dependency and the fuelling efficiency varies a lot depends on the plasma conditions. Obtained values are aimed to be approximated by the simplest functions and the numerical coefficients are presented in Table 5.3.

In order to understand the presented relations the density source profiles for simulations with low q should be considered. The simulations with $q = 3$ is characterized by the low initial plasma density and temperature (Fig. 5.32). Injected neutral particles penetrate through the SOL region and ionized mostly in the edge region even in case

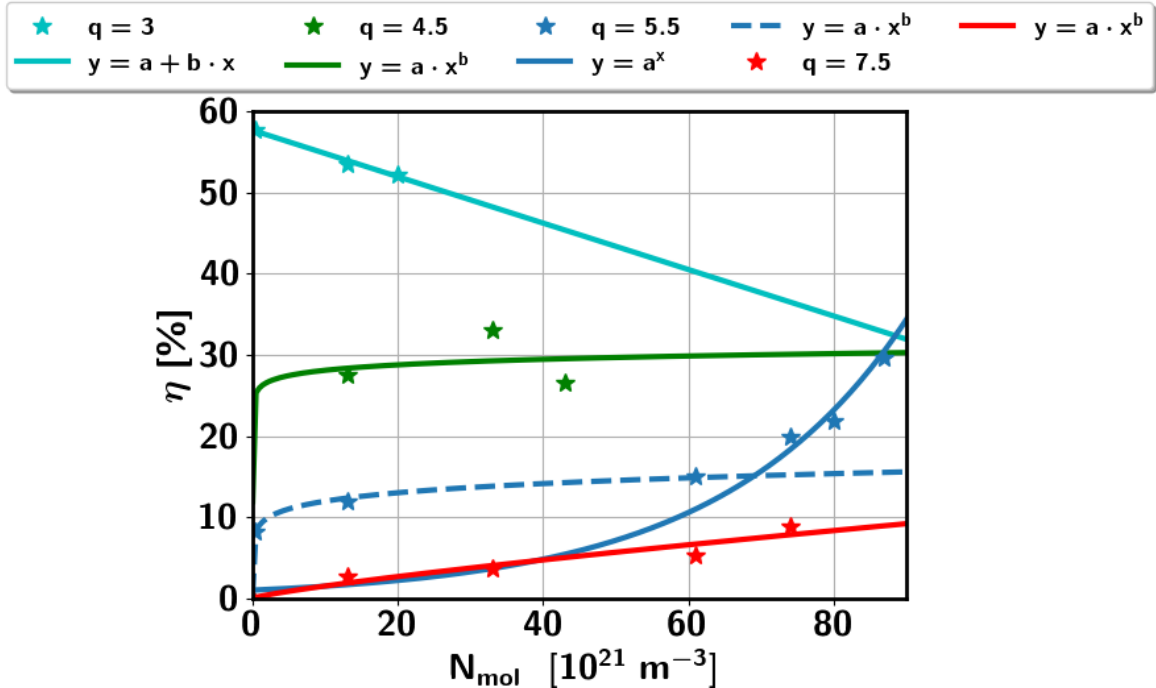


Figure 5.41: The ionization efficiency as functions of the molecular beam intensity

of the small injection densities. The increase of the molecular injection density leads to the increase of the averaged plasma density and enhanced plasma-neutral interaction in the SOL region. The normalized density source profiles for simulations with $q = 3$ are shown in Fig. 5.42. The increase of the molecular beam intensity leads to the slightly deeper penetration of molecules inside the edge region as seen in Area I in Fig. 5.42. At the same time the stronger neutral injection dramatically increases the averaged plasma density in the SOL region while the temperature decreased less than 5 % (Fig. 5.34). For this reason the higher density source in the SOL region is observed with increase of the molecular beam intensity as seen in Area II in Fig. 5.42. Thereby the decrease of the ionization efficiency with increase of the molecular beam intensity in simulations with $q = 3$ is understandable. The density profiles simulations with $q = 4.5$ are shown in Fig. 5.42. The plasma dynamics in the middle of the SOL region plays the essential rule in the radial distribution of the density source. Therefore nearly linear dependency of the ionization efficiency from the beam intensity in simulations with $q = 4.5$ is understandable. There are two approximation curves of the ionization efficiency as function of the molecular beam intensity for simulations with $q = 5.5$. With the density higher the critical value the temperature drop in the SOL region is more pronounced (Fig. 5.35) and the ionization efficiency grows faster with increase of the molecular beam intensity.

Summary

Increase of the beam injection density leads to the deeper penetration of neutrals due to decrease of the plasma temperature and reduction of the reaction rates. The dependency of the fuelling efficiency from the molecular density depends on the plasma conditions and grows weaker with increase of the plasma parameters. Since the dependence of the ionization efficiency on the molecular beam intensity is not so strong

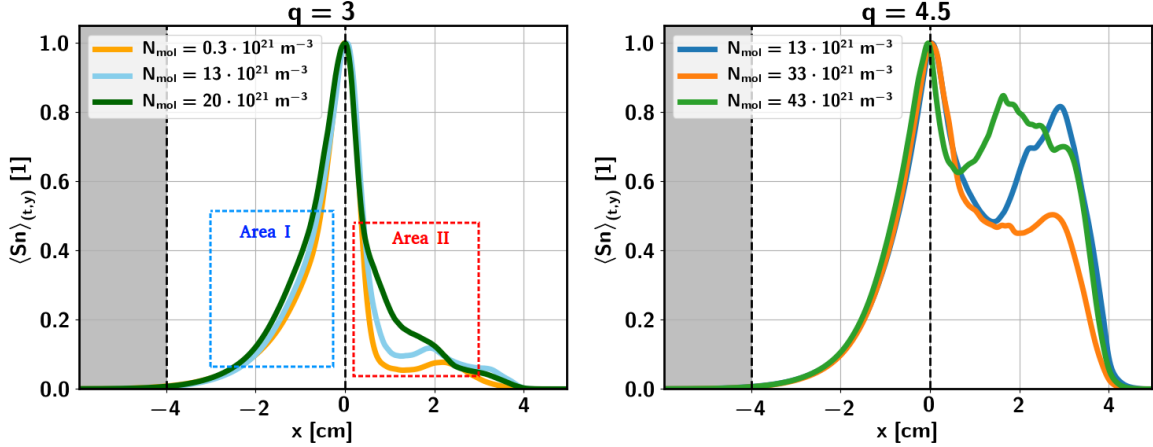


Figure 5.42: Normalized density source profiles for the simulations with $q = 3$ and $q = 4.5$. Area I on the left plot demonstrates the increase of the neutral penetration depth with increase of the molecular intensity. Area II demonstrates the increase of the ionization rate in the SOL region with increase of the molecular density.

	a	b	y
$q = 3$	57	-0.28	$y = a + b \cdot (N_{mol})$
$q = 4.5$	23	0.034	$y = a \cdot (N_{mol})^b$
$q = 5.5$ Small	9	0.1	$y = a \cdot (N_{mol})^b$
$q = 5.5$ Large	1.04		$y = a^{(N_{mol})}$
$q = 7.5$	0.26	0.8	$y = a \cdot (N_{mol})^b$

Table 5.3: Approximation coefficient for the ionization efficiency.

to explain the difference in plasma response on SMBI with the room temperature gas and low temperature gas on KSTAR the clustering effect might took place in those experiments. Another reason can be high ration of the molecular beam density to the plasma density sources on KSTAR and consequently stronger dependence of the efficiency from the molecular density. The critical molecular density was found in the simulations, which is defined as the density providing the density source in the edge region comparable to the forcing density source. Fuelling efficiency grows faster with increase of the molecular density beyond the critical level. More than 90 % of the density source in the edge region is produced by the ionization of Franck-Condon atoms and the rest is produced by ionization of molecules. The contribution of the molecular ionization to the density source grows with increase of the molecular beam intensity.

5.3.2 Scan of the beam velocity

The scan of the molecular beam velocity was carry out to study how the increase of a direct velocity affects on a neutrals penetration depth. As shown in previous Section 5.3.1 the ionization efficiency changes a functional dependence on a beam intensity if the molecular density is over the critical value. For this reason the scan of the beam velocity is performed for the small flux (smaller than the critical density) $\langle \Gamma_{inj} \rangle_{q5.5}^{small} = 13 \cdot 10^{24} \text{ m}^{-2} \text{s}^{-1}$ and for the large flux (larger than the critical density) $\langle \Gamma_{inj} \rangle_{q5.5}^{large} =$

$74 \cdot 10^{24} \text{ m}^{-2}\text{s}^{-1}$ for the simulations with the safety factor $q = 5.5$. In addition the scan for the simulations with low and high safety factors are performed with the fluxes $\langle \Gamma_{\text{inj}} \rangle_{q3}^{\text{large}} = 20 \cdot 10^{24} \text{ m}^{-2}\text{s}^{-1}$ and $\langle \Gamma_{\text{inj}} \rangle_{q7.5}^{\text{small}} = 74 \cdot 10^{24} \text{ m}^{-2}\text{s}^{-1}$ respectively. In these simulations the varying parameter is the injection velocity but the density varied in the according manner to keep the constant value of injected flux. The initial simulation parameters are presented in Table 3.1 and correspond to the cases *I2-V0 - I2-B-q3-V2*.

Influence of SMBI on plasma profiles

The plasma profiles compared for simulations with different injection velocity of molecules are shown in Fig. 5.43 for the simulations with large injection flux and $q = 5.5$.

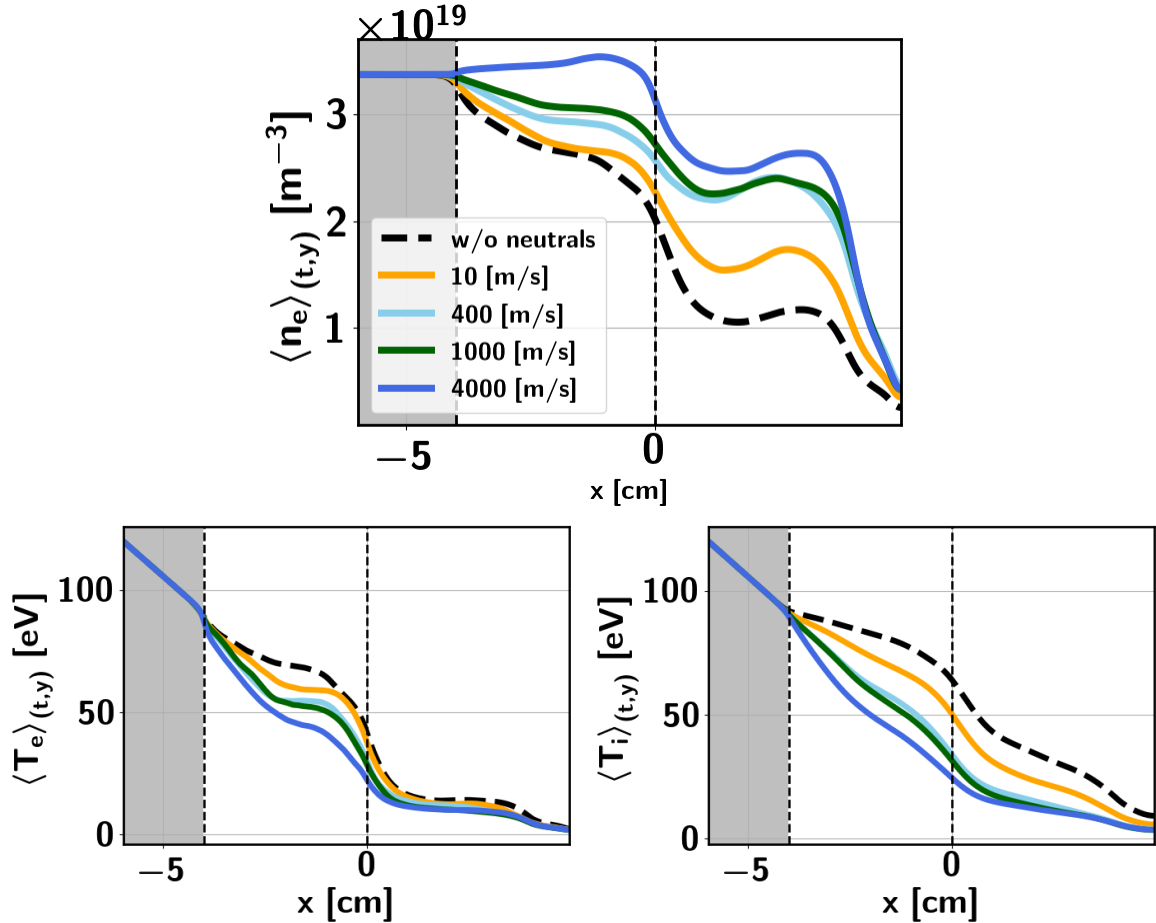


Figure 5.43: The averaged plasma profiles in simulations with different injection velocities of molecular beam. Initial parameters correspond to the cases *I2-V0 - I2-V4* in Table 5.1

The higher averaged plasma density and lower averaged temperature are observed with increase of the molecular beam velocity. Similar as for the beam intensity scan, plasma density grows faster in the edge region with increase of the beam velocity. The averaged increase of the plasma density in the edge region is up to 30 % while in the SOL region the density increase is more than 100 %. The electron temperature decreased by 35% in the SOL and by 25% in the edge. The decrease of the ion temperature in both regions is approximately two times bigger compared to the electron temperature. The deviation of the plasma profiles after injection of the small flux in the same plasma conditions does not exceed 20 % even with the high injection velocity of 10000 m/s.

2D plots of the electron temperature in the SOL region demonstrates decrease of the electron temperature on the beam propagation front. As can be seen from Fig. 5.44, the increase of the beam velocity leads to the propagation of the cold front deeper inside the plasma.

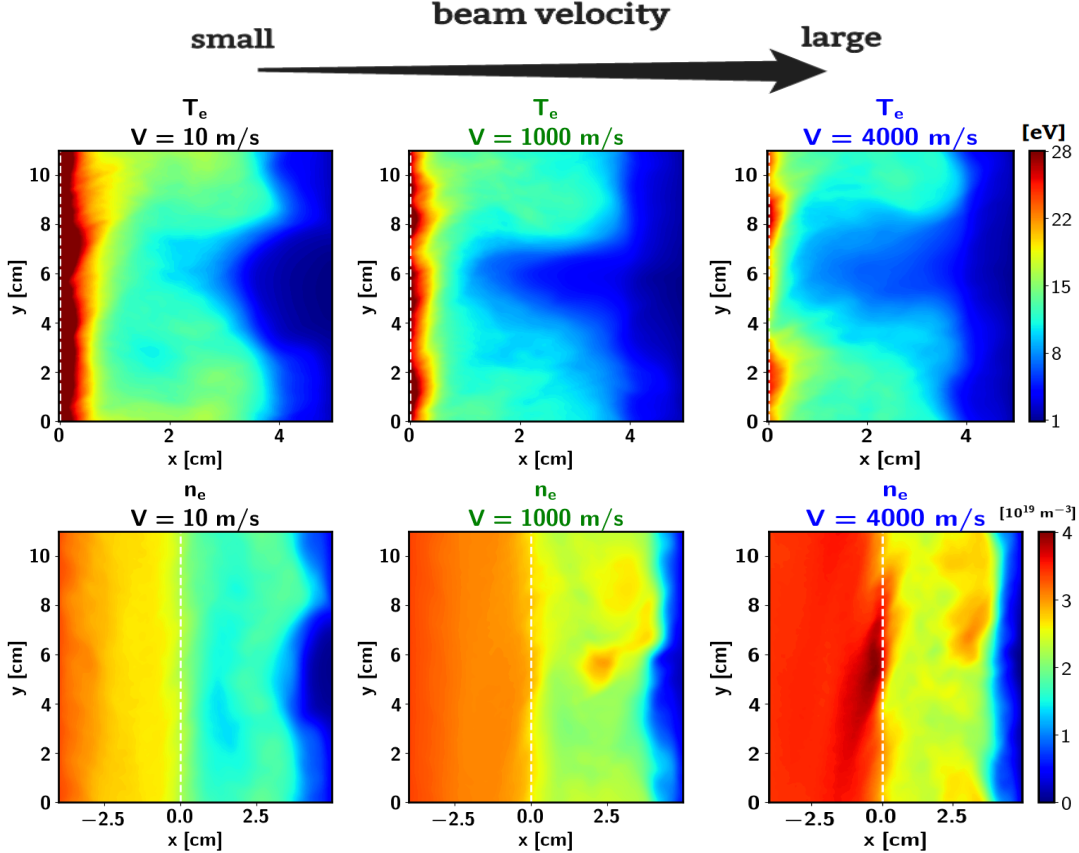


Figure 5.44: Temporally averaged plasma temperature in the SOL region (first row) and temporally averaged plasma density (second row). Initial parameters correspond to the cases $I_4\text{-}V0$, I_4 and $I_4\text{-}V2$ in Table 5.1

Unlike to the beam intensity scan, the amplitude of the density source in the SOL region does not increase with increase of the beam velocity and the maximum decrease of the temperature becomes smaller with high injection velocity. Regarding to the plasma density, the increase of the beam velocity leads to increase of the plasma density and formation of the localized density source inside the edge region. For the small injection flux no visible changes in the averaged plasma fields are observed.

Neutral penetration and density source

2D plots of the neutral fields and the density source in simulations with the large flux and $q=5.5$ are shown in Fig.5.45 for the different injection velocities. Each plot shows the time averaged field normalized on its maximum. The molecules penetrate deeper inside the plasma with increase of the direct velocity as the convection determines their transport. For the atoms convection and diffusion are comparable as was shown in Section 5.1. The thermal energy of 2 eV corresponds to the velocity approximately 14000 m/s. Radial extent of the atomic density distribution demonstrates the influence of the injection velocity on the penetration of atoms even with the amplitude of the direct

velocity lower than the thermal velocity of atoms. The density source moves forward inside the plasma with increase of the injection velocity. The narrow localization of the density source produced by the beam with the low injection velocity (Fig. 5.45g) is understandable as the plasma density and temperature are low in the far SOL region. Therefore the ionization frequency is relatively small and the density source is created mostly due to the high molecular injection density. With increase of the injection velocity neutrals penetrate deeper inside the plasma where plasma fluctuations enhance the ionization reaction rate and the broad distribution of the density source is seen on the time averaged plot (Fig. 5.45h). The reduction of the density source in the SOL region compared to the edge region is observed with further increase of the beam velocity (Fig. 5.45i). This likely relates with lower plasma density and temperature in the SOL region.

The poloidally and time averaged density source profiles for the scans with the small injection flux and large injection fluxes in simulations with $q = 5.5$ are shown in Fig. 5.46. The tendency of the deeper neutral penetration with increase of the velocity is observed for both injected fluxes. However, the molecular beam with small intensity can not provide the noticeable increase of the plasma density even when ionization happens in the SOL region.

Regarding to the comparison of the particle sink and the density source in the SOL region, the same procedure as for the beam intensity scan have been carry out for the scan of the molecular velocity. The comparison for the large injection flux $\langle \Gamma_{\text{inj}} \rangle_{q=5.5}^{\text{large}} = 74 \cdot 10^{24} \text{ m}^{-2}\text{s}^{-1}$ is shown in Fig. 5.47. As can be seen, in case of the low injection velocity the volume particle sink exceeds the density source near the LCFS (Fig. 5.47a), while in the far SOL region they are comparable (Fig. 5.47b). For the high injection velocity the density source is higher than the parallel losses over the whole SOL region (Fig. 5.47c and Fig. 5.47d).

The similar analysis for the small injection flux is shown in Fig. 5.48. As can be seen in this case the density source is comparable with the particle sink while in the simulations with the same injection velocity and large injection flux the density source significantly exceeds the particle losses (Fig. 5.47).

Comparison of the density source in the edge region with the plasma forcing is shown in Fig. 5.49. As can be seen although the injection flux is higher than the critical value, the molecular beam with low injection velocity can not provide the density source at the edge region comparable to the plasma forcing.

Approximation of density source as function of the beam velocity

The ionization efficiency as function of the molecular beam velocity is shown in Fig. 5.50. In case of the $q=3$ simulations the temperature and density are low and the difference between density source profiles is negligible for the velocities of 400 and 1000 m/s as shown in Fig. 5.51. Unlike the beam intensity scan the dependency of the ionization efficiency on the molecular beam velocity can be described by the same simple function dependency in all considered plasma conditions and injection densities. The approximation coefficients are summarized in Table 5.4.

Summary

Ionization efficiency grows with increase of the velocity of injected molecules. The dependency of the ionization efficiency on the injection velocity grows weaker with

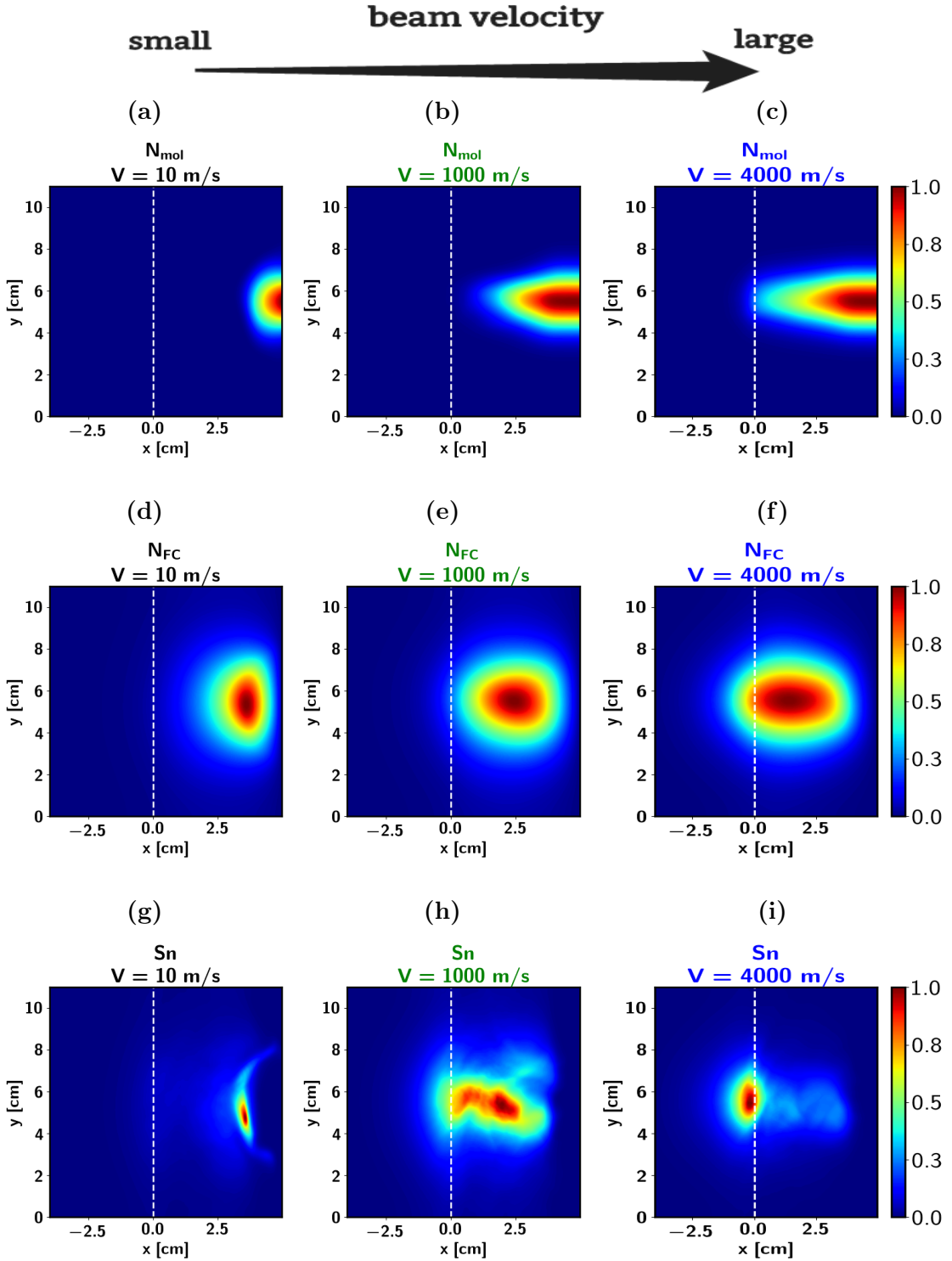


Figure 5.45: Temporally averaged neutral fields and the density source. Each field is normalized on its maximum. Initial parameters correspond to the cases $I_4\text{-}V0$, I_4 and $I_4\text{-}V2$ in Table 5.1

increase of the plasma conditions. Independently on the molecular beam intensity the increase of the direct velocity leads to the deeper penetration of neutrals and enhance of the fuelling efficiency.

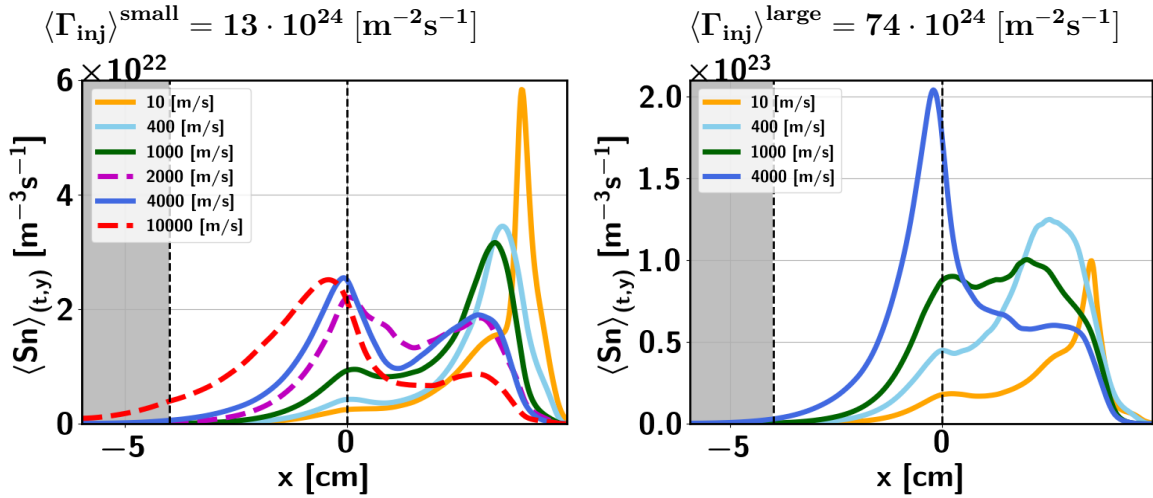


Figure 5.46: The averaged density source profiles for simulations with different injection velocities. Initial parameters correspond to the cases *I2-V0-I2-V4* and *I4-V0-I4-V2* in Table 5.1

	a	b	y
q = 3	7.74	0.28	$y = a \cdot (V_{smbi})^b$
q = 5.5 Small	3.14	0.12	$y = a \cdot (V_{smbi})^b$
q = 5.5 Large	0.36	0.58	$y = a \cdot (V_{smbi})^b$
q = 7.5	0.094	0.66	$y = a \cdot (V_{smbi})^b$

Table 5.4: Approximation coefficients for the ionization efficiency as function of the molecular beam velocity.

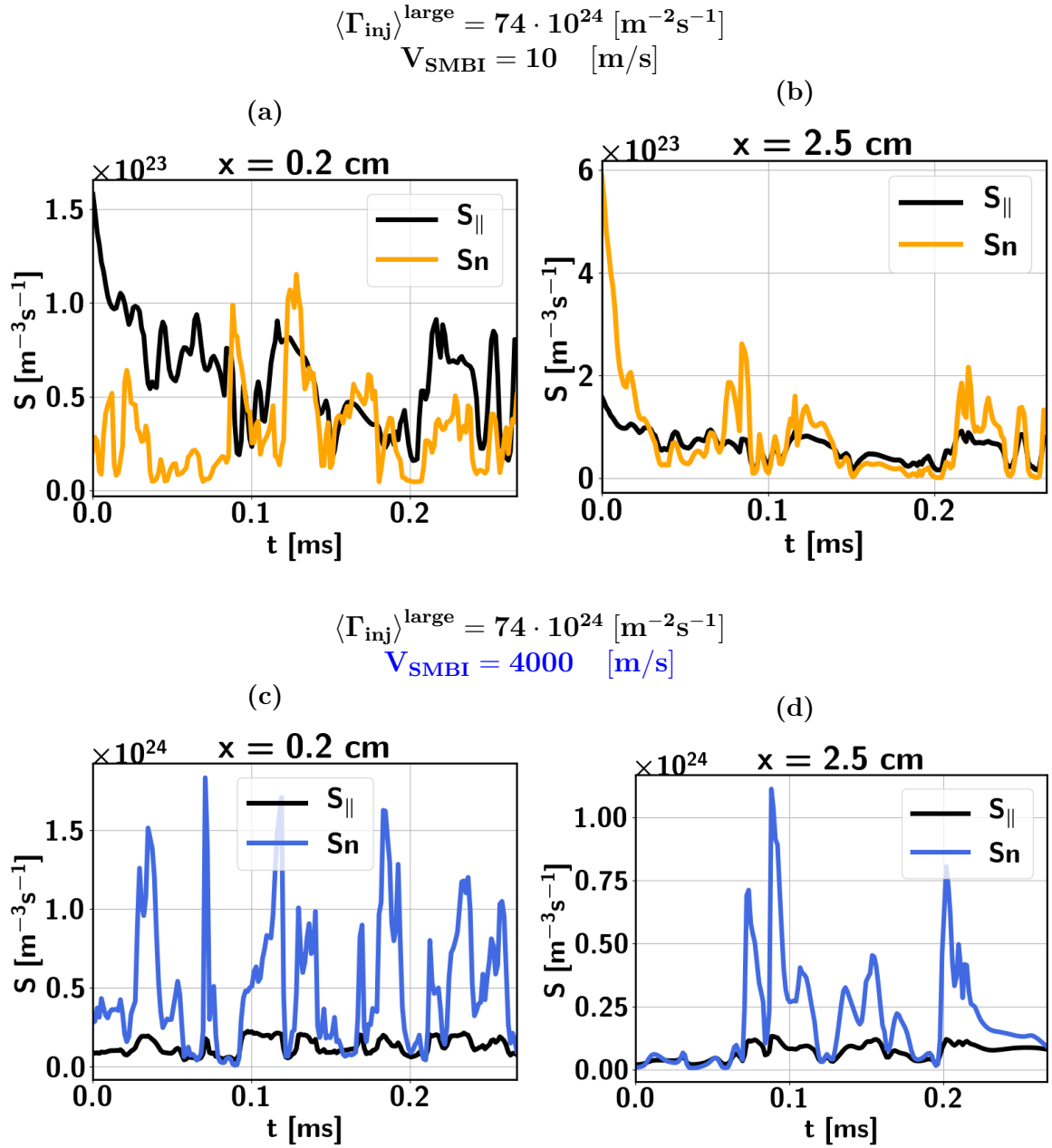


Figure 5.47: Comparison of the density source (Sn) with the particle sink ($S_{||}$) in the SOL region. Initial parameters correspond to the cases $I4\text{-}V0$ and $I4\text{-}V2$ in Table 5.1

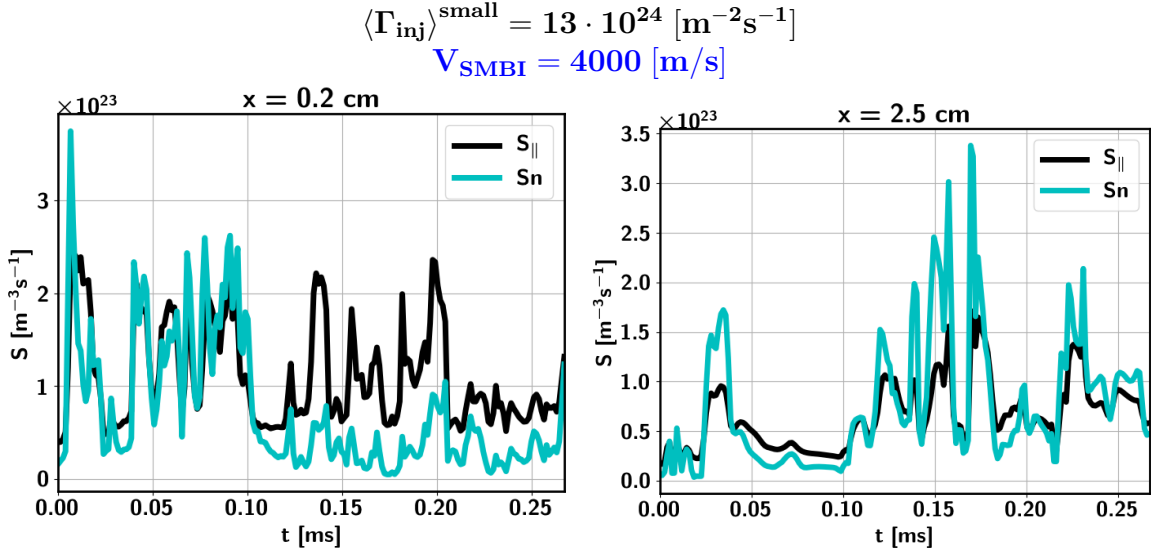


Figure 5.48: Comparison of the density source (S_n) with the particle sink ($S_{||}$) in the SOL region. Initial parameters correspond to the cases $I2-V3$ in Table 5.1

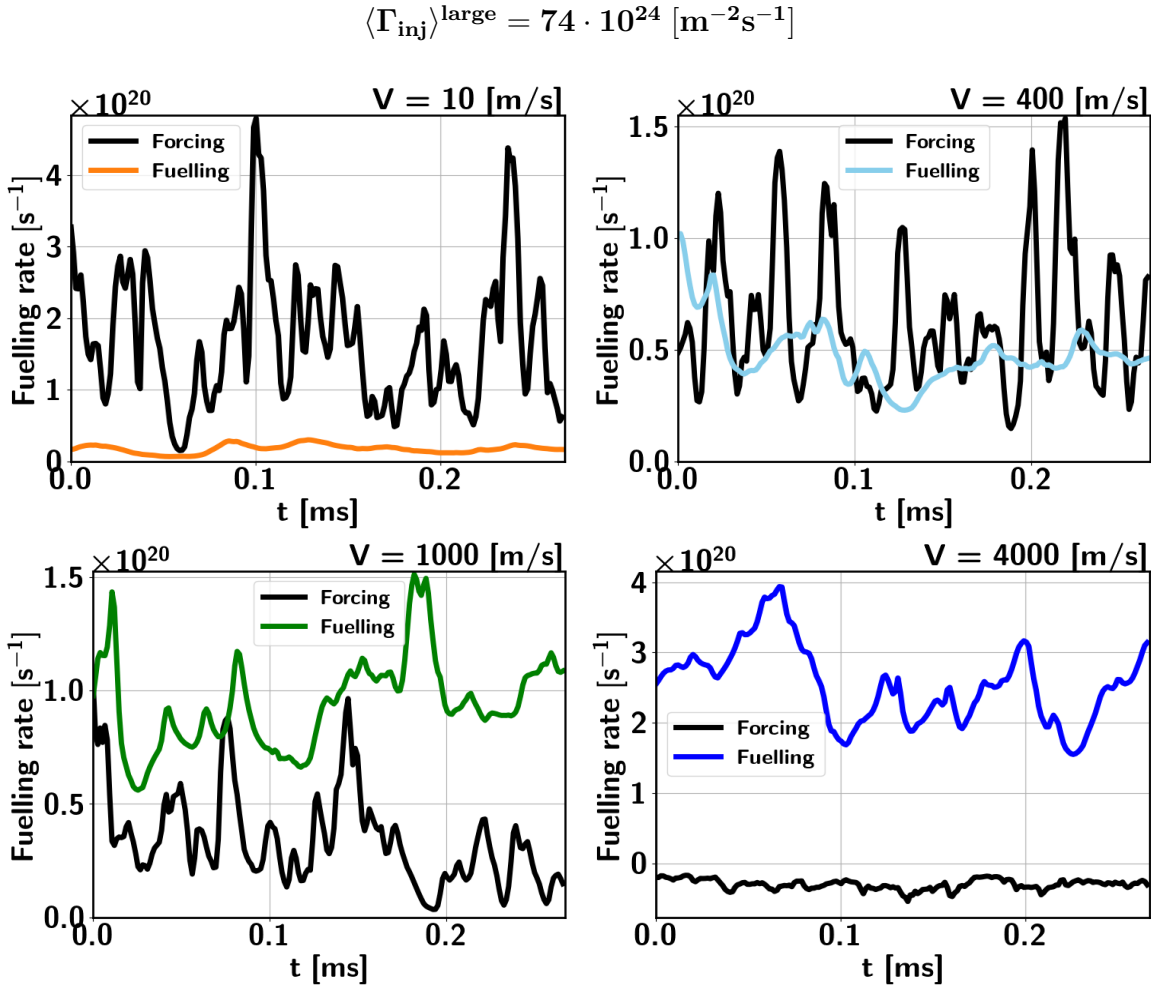


Figure 5.49: Comparison of the forced density source (forcing) and density source produced by ionization neutrals. Initial simulation parameters correspond to the cases $I4-V0$ - $I4-V2$ in Table 5.1

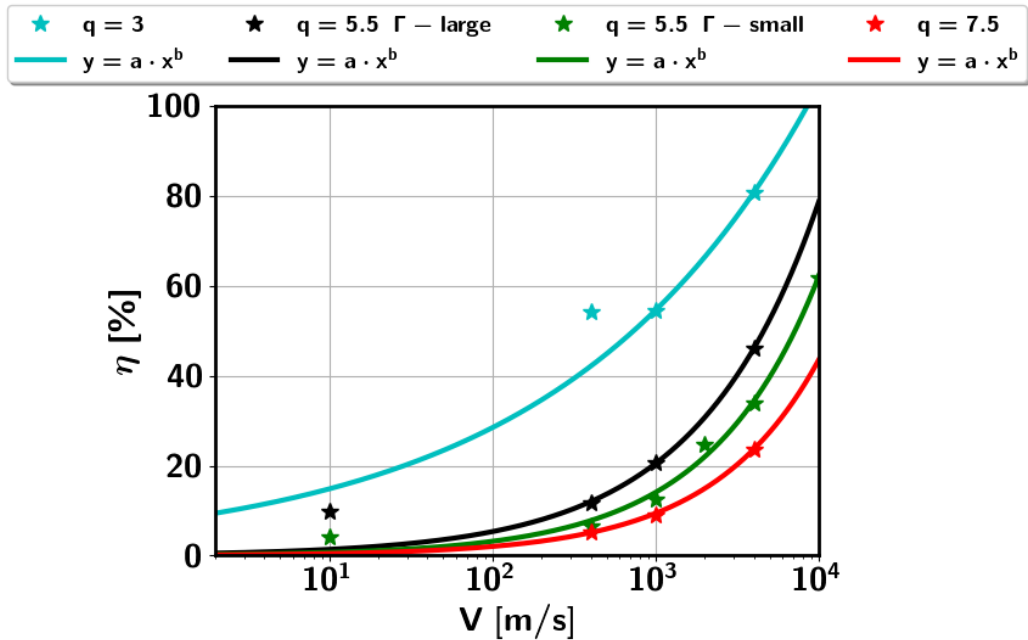


Figure 5.50: Ionization efficiency as functions of the molecular beam velocity.

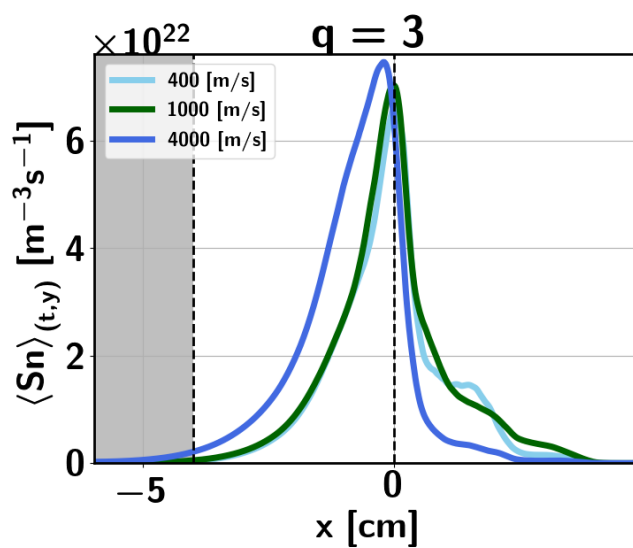


Figure 5.51: Averaged density source profiles in simulations with $q = 3$. Initial parameters correspond to the cases $I2\text{-}B\text{-}q3\text{-}V1$ and $I2\text{-}B\text{-}q3\text{-}V2$ in Table 5.1.

5.3.3 Scan of the beam width

The scan of the beam width was performed to investigate if the beam has a local effect on the plasma and how fuelling efficiency scales with the beam width. Similar to the velocity scan the scan of the beam width was made for the small $\langle \Gamma_{\text{inj}} \rangle_{q5.5}^{\text{small}} = 13 \cdot 10^{24} \text{ m}^{-2}\text{s}^{-1}$ and large flux $\langle \Gamma_{\text{inj}} \rangle_{q5.5}^{\text{large}} = 74 \cdot 10^{24} \text{ m}^{-2}\text{s}^{-1}$. In addition the scan for the simulations with low safety factor and high safety factor are performed with the fluxes $\langle \Gamma_{\text{inj}} \rangle_{q3}^{\text{large}} = 20 \cdot 10^{24} \text{ m}^{-2}\text{s}^{-1}$ and $\langle \Gamma_{\text{inj}} \rangle_{q7.5}^{\text{small}} = 74 \cdot 10^{24} \text{ m}^{-2}\text{s}^{-1}$ respectively. The total density and velocity of the beam are keep the same in this scan. The initial profiles of the injected beams are shown in Fig. 5.52. The beam width of 11 cm in reality represents the uniform density level over the domain and in principle can be considered as the beam with an infinity width.

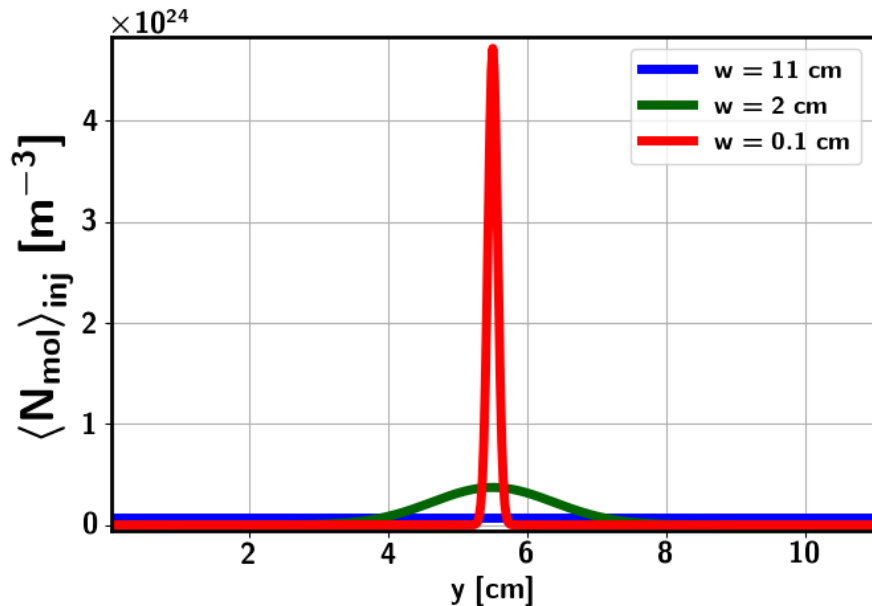


Figure 5.52: The initial profiles of the injected beams. Initial simulations parameters correspond to the cases *I4-NB - I4-F* in Table 5.2. The beam width of 11 cm in reality represents the uniform density level over the domain

Influence of SMBI on plasma profiles

As for the velocity scan there are no difference in plasma profiles in the scan of the small injection flux. The plasma profiles in the scan with the large injection flux are shown in Fig. 5.53. The difference in plasma profiles are not very pronounced however the stronger influence of the narrow beam in the edge region is distinguishes.

2D plots of the time averaged plasma temperature and density are shown in Fig. 5.54. The localized density source is observed inside the edge region only in case of the narrow beam injection. Comparison of the plasma temperature in SOL region (Fig. 5.54) shows the hole in plasma temperature, created by the narrow beam. This effect likely relates with significantly higher density of the narrow beam compared to the other cases (Fig. ??).

The poloidal variations of the time averaged plasma density and plasma temperature are compared in different radial positions. The peak of the plasma density is

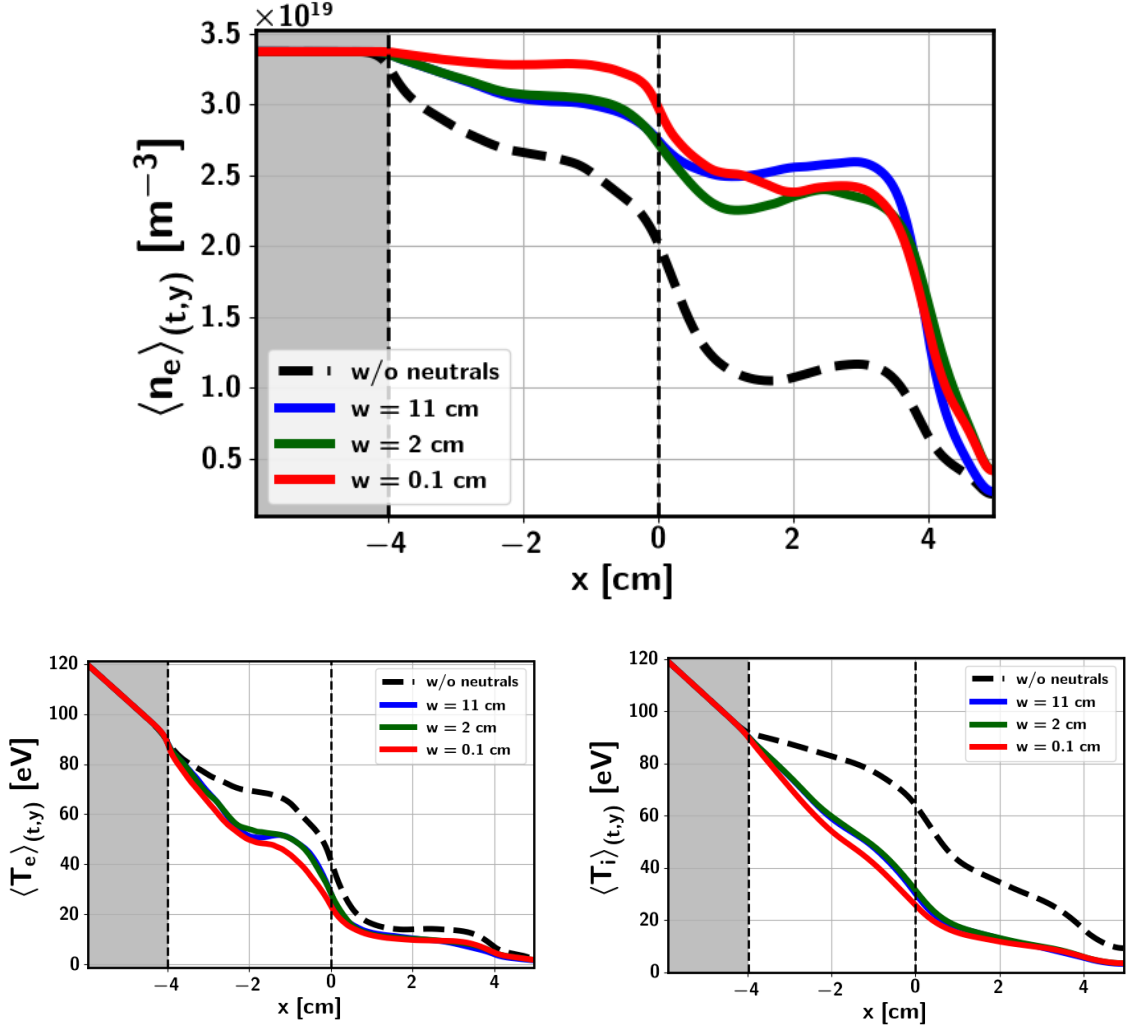


Figure 5.53: The averaged plasma profiles from the simulations with the large injection flux $\langle \Gamma_{inj} \rangle^{large} = 74 \cdot 10^{24} [m^{-2}s^{-1}]$. Initial parameters correspond to the cases I_4-NB , I_4 , I_4-F in Table 5.2.

observed inside the edge region $x = 0.45\text{ cm}$ from LCFS (Fig. 5.55). Inside the SOL region the difference between various neutral injections becomes weaker. As can be noticed in Fig. 5.55, the position of the density peak shifts downwards with the distance from the edge to SOL region, that is caused by the plasma motion. Poloidal variation of the plasma temperature (Fig. 5.56) shows pronounce decrease of the plasma temperature in case of the injection of the narrow beam. The position of the minimum of plasma temperature corresponds to the poloidal center of the domain in all radial positions in the SOL region. No local effect on the plasma temperature in the edge region is observed, although the averaged plasma temperature is lower in the case of narrow beam injection.

Neutral penetration and density source

The temporally averaged and normalized neutral fields corresponding to simulations with large neutral flux $\langle \Gamma_{inj} \rangle^{large} = 74 \cdot 10^{24} m^{-2}s^{-1}$ are shown in Fig. 5.57. As seen from the figure the shape of the molecular beam is defined by the initial width. Despite

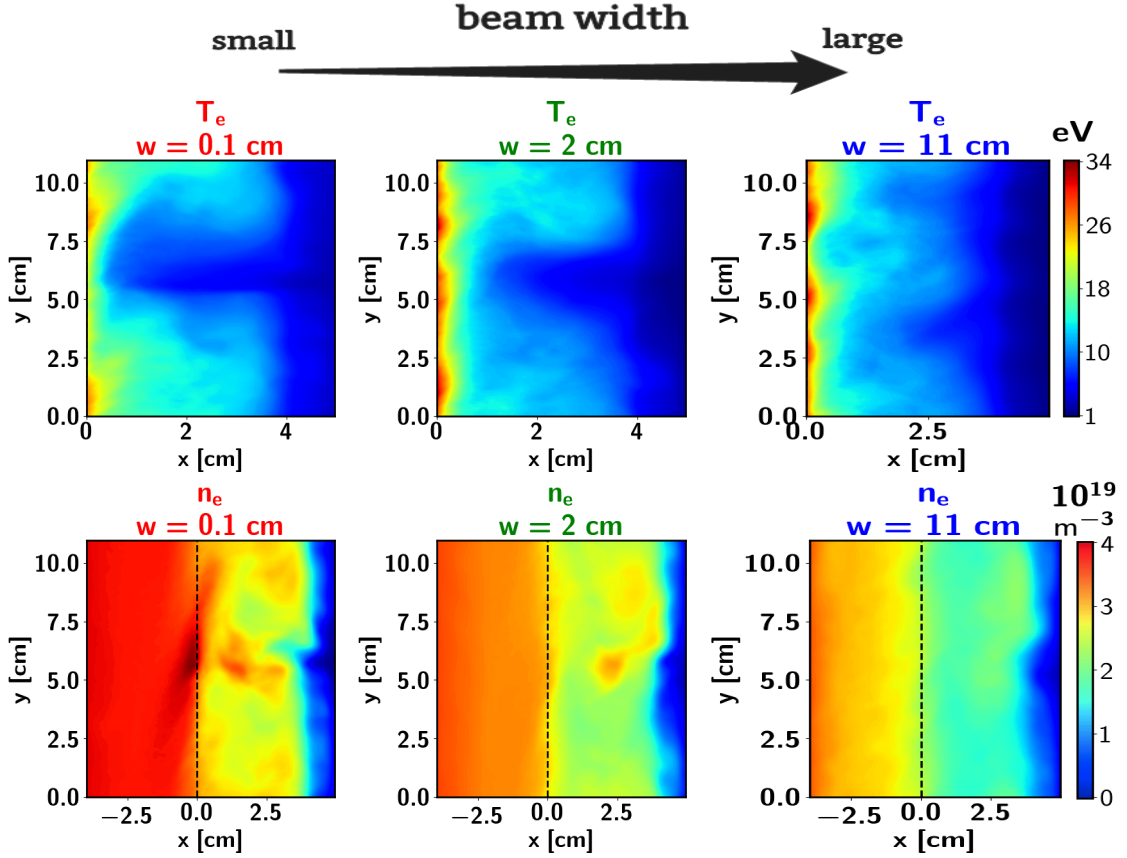


Figure 5.54: Temporally averaged plasma temperature in the SOL region (first row) and temporally averaged plasma density (second row). Initial parameters correspond to cases $I_4\text{-NB}$, I_4 and $I_4\text{-F}$ in Table 5.2.

the diffusion spreading of atoms the density source produced by the narrow beam keep the narrow localization. The density source profiles compared in different simulations are shown in Fig. 5.58. As can be seen the variation of the beam width in simulations with low safety factor or low injection flux almost do not affect on the penetration of neutrals.

Comparison of the fuelling at the edge by the forced density source and neutral source resulted in ionization of injected particles Fig. 5.59 shows that increase of the beam width decrease the ratio of the neutral density source to the plasma particle source in the edge region.

Approximation of the density source as function of beam width

The ionization efficiency as a function of the beam width is shown in Fig. 5.60. As was already noticed the ionization efficiency does not depends on the beam width in simulations with low q or low injection neutral flux. Approximation coefficients are summarized in Table 5.5.

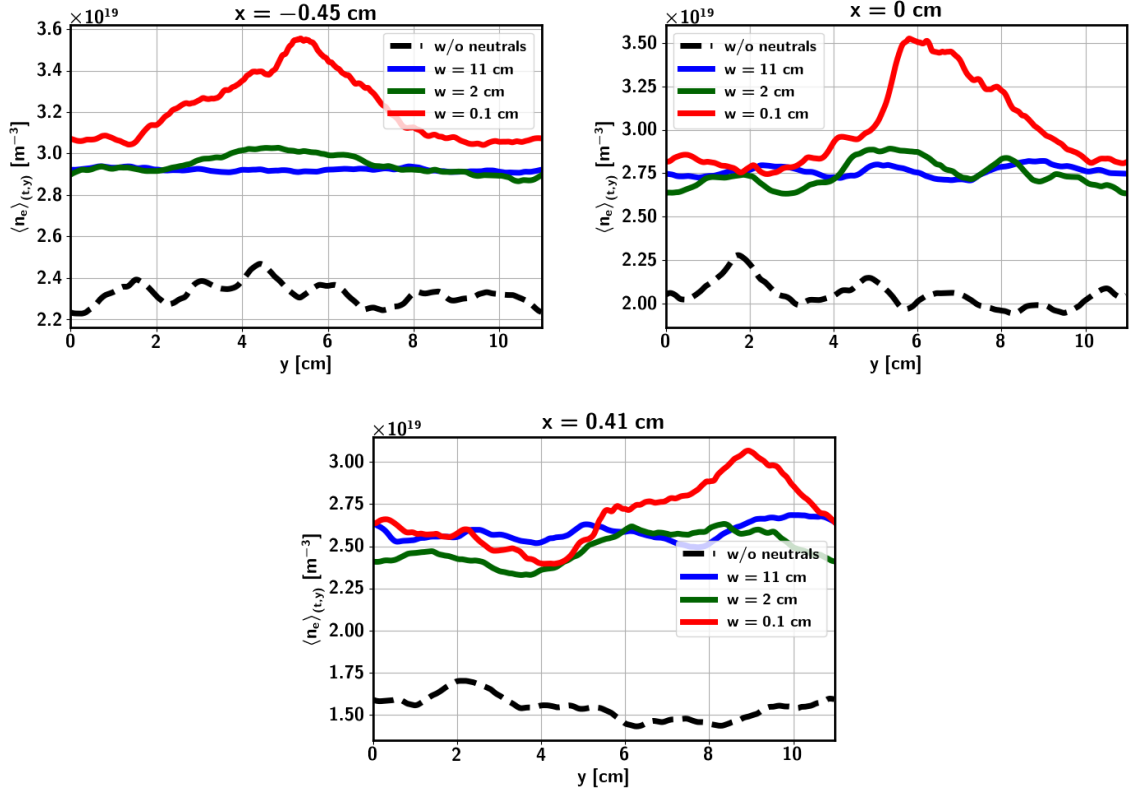


Figure 5.55: The poloidal variations of the time averaged plasma density in different radial positions. Initial parameters correspond to cases $I_4\text{-NB}, I_4$ and $I_4\text{-F}$ in Table 5.1.

	a	b	c	y
$q = 3$	-1.5e+04	6.3e-05	1.5e+04	$y = a \cdot (w_{smbi})^b + c$
$q = 5.5$ Small	-50.6	0.08	74.44	$y = a \cdot (w_{smbi})^b + c$
$q = 5.5$ Large	4.8e+03	-6.5e-05	-4.84e+03	$y = a \cdot (w_{smbi})^b + c$
$q = 7.5$	-2.2	0.57	12	$y = a \cdot (w_{smbi})^b + c$

Table 5.5: Approximation coefficients for the ionization efficiency as function of the molecular beam width.

Summary Influence of the beam width on the neutral penetration and ionization efficiency is not observed in simulations with low q or low injection neutral flux. If the injection flux is higher the critical value or plasma parameters are increased the ionization efficiency is higher in case of injection of the narrow dense beam.

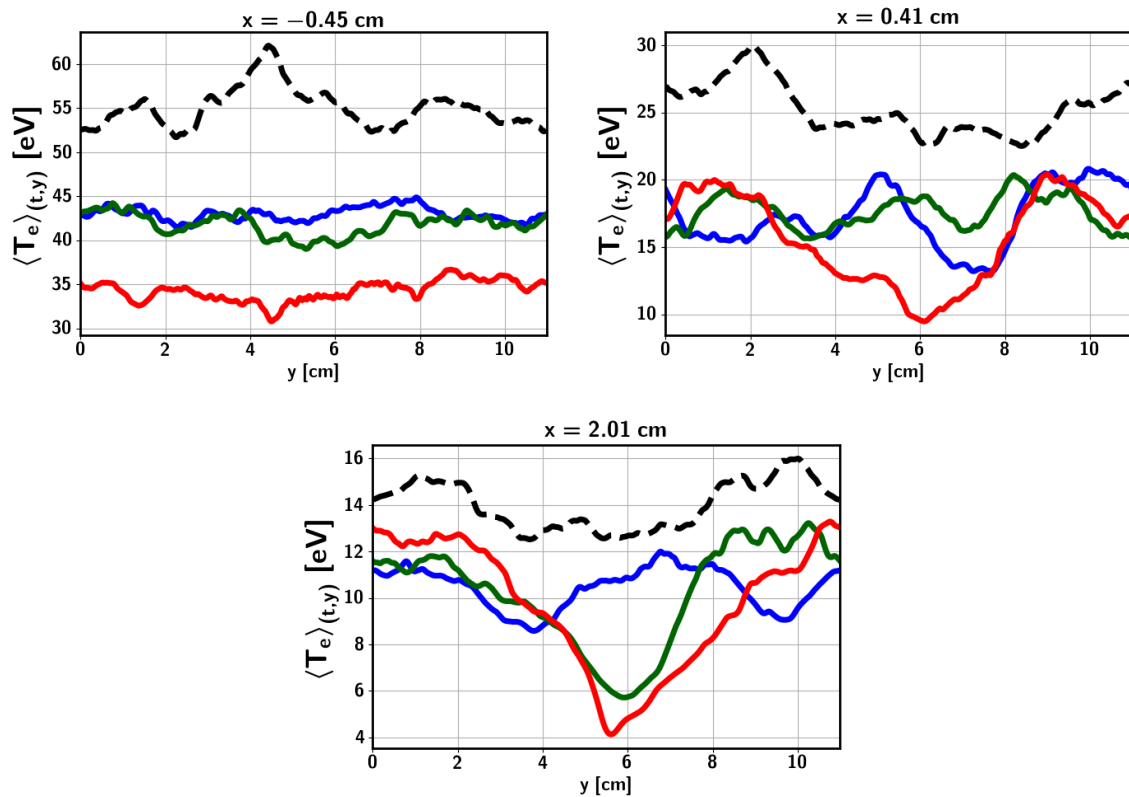


Figure 5.56: The poloidal variations of the time averaged plasma temperature in different radial positions. Initial parameters correspond to the cases I_4 -NB, I_4 , I_4 -F in Table 5.1.

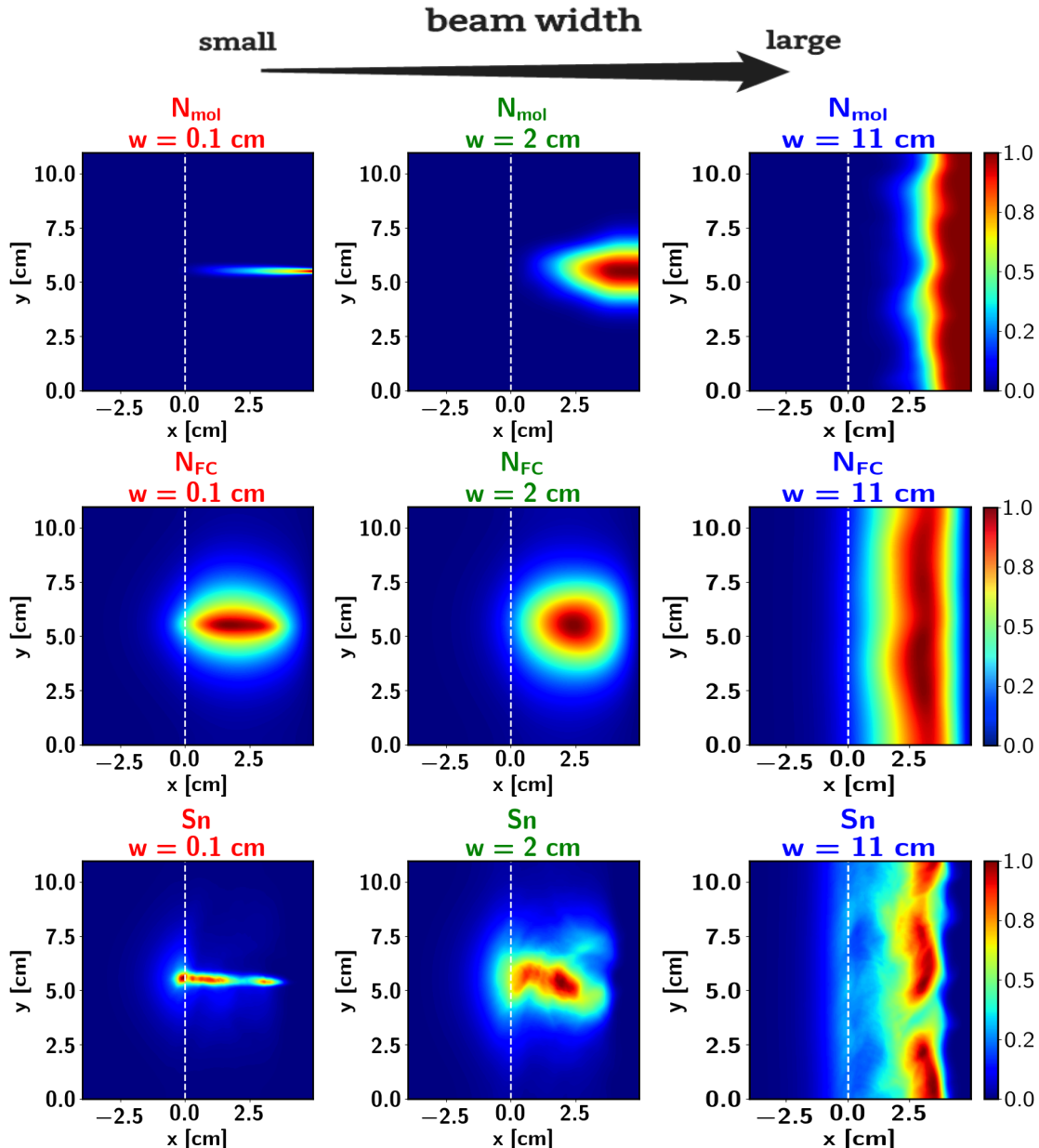


Figure 5.57: Time averaged molecular density (N_{mol}), density of atoms (N_{FC}) and density source(Sn). Each field is normalized on its maximum. Initial parameters correspond to the cases $I_4\text{-NB}$, I_4 , $I_4\text{-F}$ in Table 5.2.

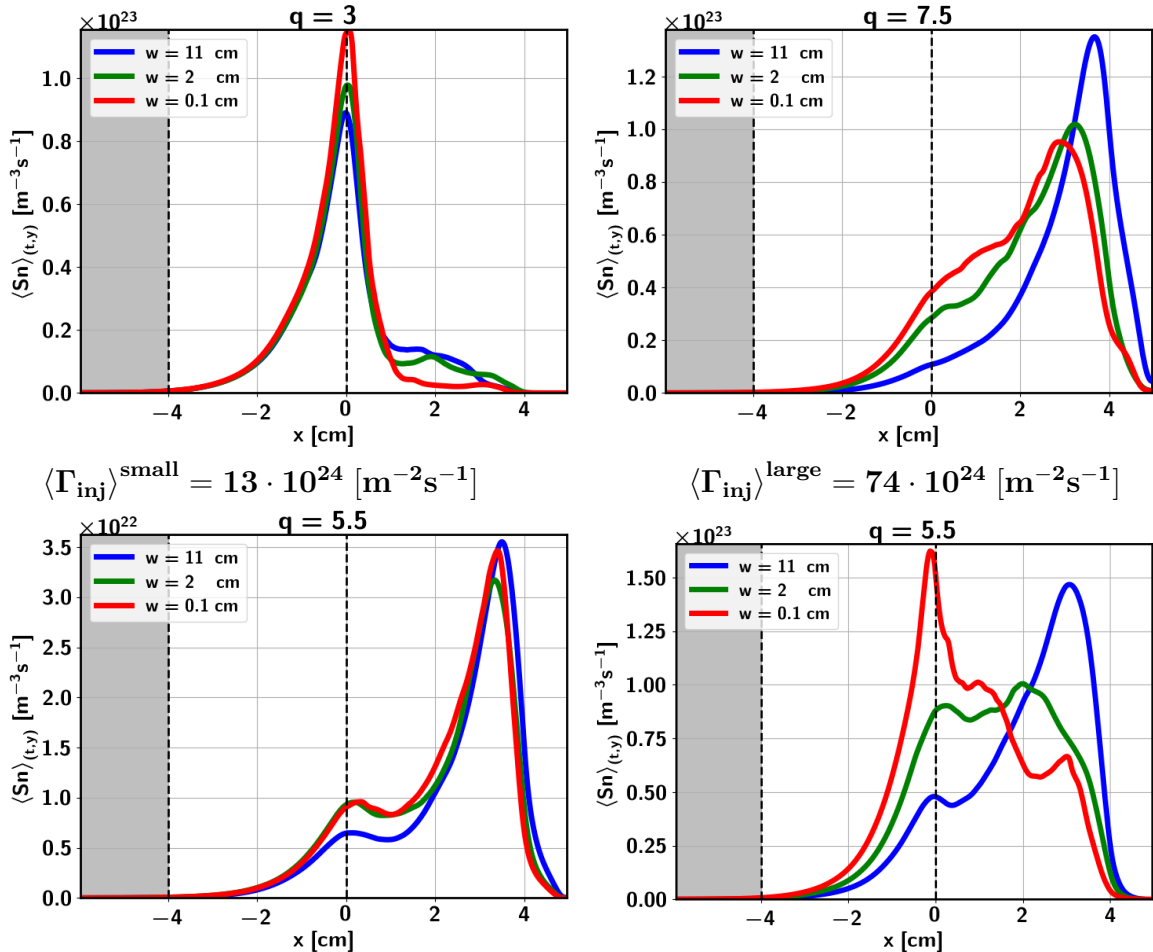


Figure 5.58: Averaged density source profiles in simulations with different plasma conditions and injection fluxes. Initial parameters correspond to the cases $I_4\text{-NB}$ - $I_4\text{-q2-F}$ in Table 5.2

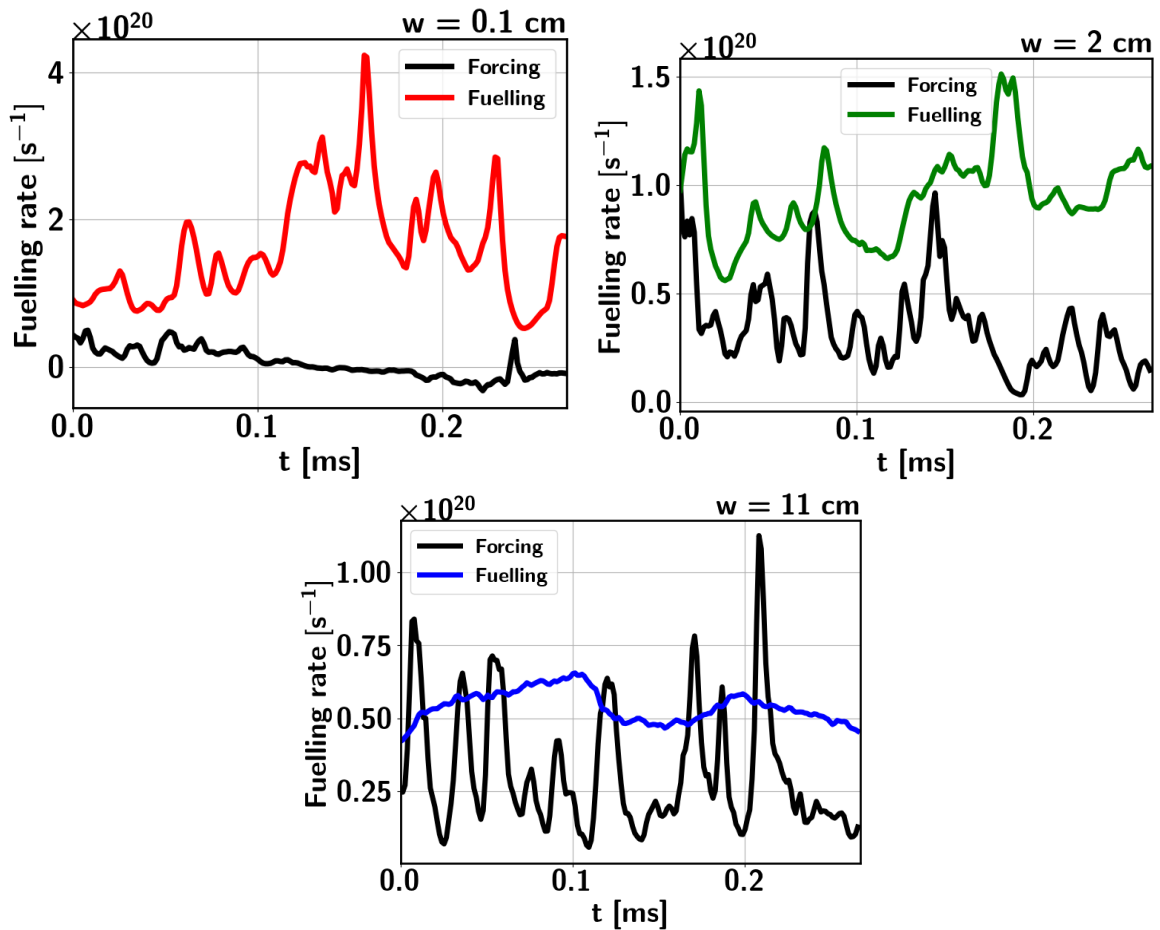


Figure 5.59: Comparison of the fuelling at the edge by the forced density source and neutral source resulted in ionization of injected particles. Initial parameters correspond to the cases $I_4\text{-}NB$, I_4 , $I_4\text{-}F$

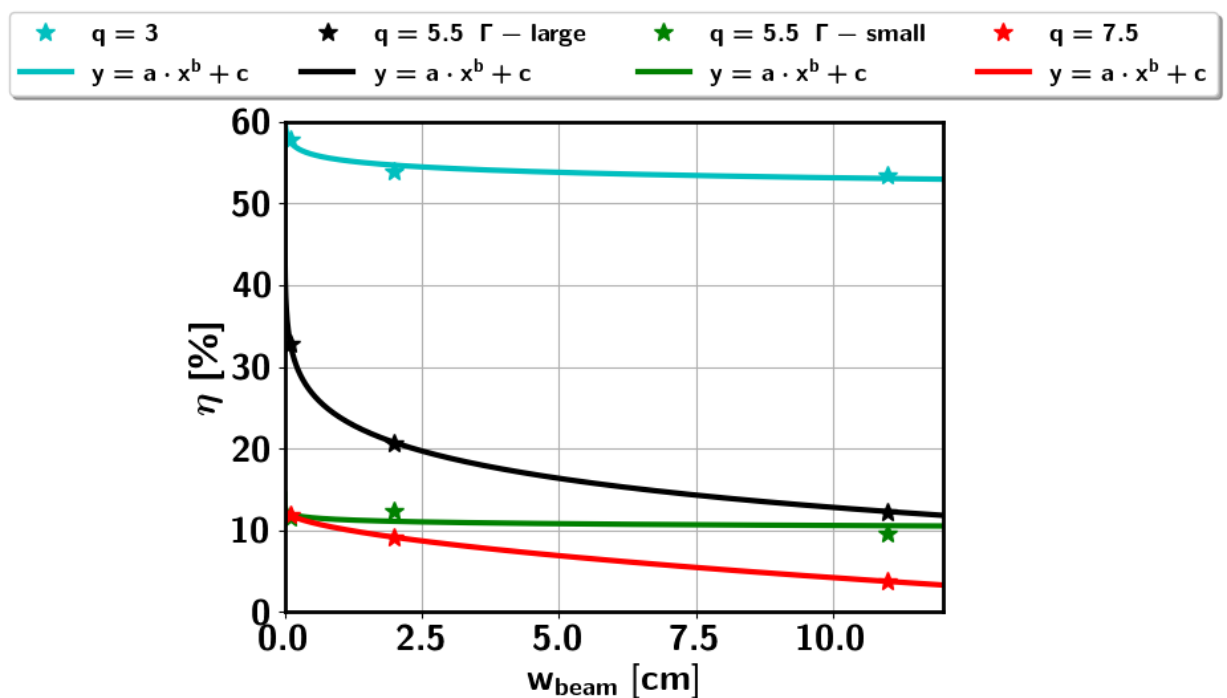


Figure 5.60: The ionization efficiency as a function of beam width

5.4 Influence of SMBI on a plasma turbulence transport

The HESEL model provides good opportunity to investigate the influence of SMBI on plasma fluctuations. As mentioned in Section 2.1 the mitigation of ELMs and reduction of the large amplitude plasma fluctuations were observed on HL-2A and KSTAR tokamaks. Analysis of the microwave imagine reflectometer data on KSTAR reveals the changes in the density fluctuation specter during SMBI. The underlying physical mechanism of the influence of SMBI on plasma fluctuations is not fully understood yet. The reduction of the gradient in the density profiles caused by SMBI might be a reason of the decrease of the low frequency content of the density fluctuations and increase of the high frequency fluctuations [29]. According to the results of the simple phenomenological model the degradation of the plasma pedestal caused by SMBI results in the developing of the large amplitude fluctuations instead of the small one. The experiments on ASDEX Upgrade [28] demonstrated that ionization of neutrals should happen inside the edge region to affect on ELMs and perturb the plasma pedestal. In experiments on ASDEX Upgrade the supersonic molecular beam penetrated only until the separatrix and no prompt effect on the ELM frequency was observed. Comparison of the experiments on ASDEX Upgrade, HL-2A and KSTAR tokamaks indicates that the critical molecular beam density exists when the SMBI start to affect on the plasma ELM frequency. Although the HESEL model allows investigation of the plasma dynamics only in the L-mode the HESEL-SMBI simulations can shadow the light on the mechanism of influence of SMBI on plasma dynamics fluctuations.

To investigate the influence of SMBI on plasma fluctuations, statistical properties of plasma are analysed based on the data from the beam parameter scan. As was noticed in the beam intensity scan the SMBI injection into the low temperature and density plasma leads to enhanced of plasma-neutral interactions in the SOL. Therefore statistical properties of plasma in simulations with initial parameters corresponding to the cases $I1-q3$ and $I2-q3-B$ in Table 5.1 are compared with the corresponding reference case without neutral injection. As the increase of the safety factor modifies the plasma dynamics, two simulations with the beam intensity lower the critical value ($I2$) and higher the critical density ($I4$) are compared with corresponding reference simulations. To investigate the effect of the beam size on the fluctuation transport the simulations with parameters $I4 - NB$ and $I4 - F$ are compared with the corresponding reference case. The same procedure is performed for the velocity effect and simulations $I2 - V0, I2 - V4, I4 - V0, I4 - V2$.

5.4.1 Dependence on a beam intensity

Firs the fluctuation level for plasma density and temperature is analysed. The fluctuation level is defined by the equation

$$\zeta_f = \frac{\sqrt{\langle (f - \langle f \rangle_{(y,t)})^2 \rangle_{(y,t)}}}{\langle f \rangle}. \quad (5.24)$$

The fluctuation level for the plasma density and plasma temperature is show in Fig. 5.61. As can be seen the neutral injection leads to decrease of the fluctuation level for the plasma density. In the simulations with the low safety factor $q = 3$ the higher neutral injection $N_{\text{mol}} = 20 \cdot 10^{21} \text{ m}^{-3}$ results in nearly zero fluctuation level in the

edge and reduction of the fluctuation level by 16% in the SOL. In the simulations with $q = 5.5$ the small intensity injection $N_{\text{mol}} = 13 \cdot 10^{21} \text{ m}^{-3}$ results in decrease of the fluctuation level for plasma density in roughly 20 % in both SOL and edge regions. The decrease of the fluctuation level with higher molecular injection $N_{\text{mol}} = 84 \cdot 10^{21} \text{ m}^{-3}$ is more than 50% over the whole domain except the wall region. This result is similar to observed in [63], where the neutral gas injection reduced the fluctuation level of plasma density due to increase of the average density. As can be seen from Fig. 5.61 the fluctuation level for the electron temperature does not changed except the small increase in case of neutral injection $N_{\text{mol}} = 20 \cdot 10^{21} \text{ m}^{-3}$ in the low q plasma. The fluctuation level for ion temperature increased up to 80% in the edge region and up to 25% in the SOL in both cases with high neutral injection. It should be emphasise that the fluctuation level reflects the ratio amplitude of the fluctuations to the mean value rather the amplitude of fluctuations. The simulations with $q = 3$ in reality describes the less fluctuation activity than the simulations with $q = 5.5$ although the fluctuation level is higher in the former case. To look in the mechanism of influence of SMBI on plasma transport in more details the other statistical properties are investigated.

Intermittent plasma transport are commonly analysed through a probability density function(PDF) and statistical moments of fluctuating signals [64–66]. The common observation from various devices is that PDFs of the density fluctuations are non-Gaussian and usually can be described by a Gamma-distribution function. Modifications of PDFs caused by the neutral injection indicate changes in plasma turbulent transport. The PDF functions of the plasma density fluctuations (in normalized units) are compared in three radial positions in Fig. 5.62. In both scans only the higher neutral injection noticeably modifies the PDF that indicates the existence of the critical density when neutrals start to affect on the fluctuations. If the neutral source is comparable with the forcing rate when the difference in plasma statistics is observed. Even when the density source is smaller than the forcing fuelling rate ($N_{\text{mol}} = 13 \times 10^{21}$) but already at the same order (Fig. 5.40) the small influence in plasma statistics is already observed. In case of the smaller neutral density ($N_{\text{mol}} = 0.3 \times 10^{21}$) no influence on plasma statistics is observed. It might seems that the forcing is just a numerical feature of the HESEL model. However forcing is just an approximation to the core region. Comparing the density source with the forcing fuelling is equivalent to comparison with the plasma sources coming from the core region. Obviously the critical molecular density level depends on the plasma conditions.

In the edge region PDFs of the signals without neutral injection or with low injection is close to the normal distribution with the small tails to the positive part in simulations with $q = 3$ and to the negative part in simulations with $q = 5.5$. The positive tails of the Gamma distribution indicates a high probability of the large fluctuations. This is in agreement with observations in different numerical experiments [65]. High neutral injection results in reshape of the PDF to much narrower distribution with small positive tails. On the LCFS PDF of the plasma density is asymmetric due to comparable probability of the large and small fluctuations. Neutral injection tends to make the distribution more symmetric. In the low q simulations it happens by the increase of the width of PDF while for the higher q case effect is opposite and the distribution function after neutral injection is has higher amplitude and lower width. Width of the distribution function of the signal is characterised by the second statistical moment, which is called the variance (σ).

$$\sigma = \sqrt{\langle (n - \langle n \rangle)^2 \rangle} \quad (5.25)$$

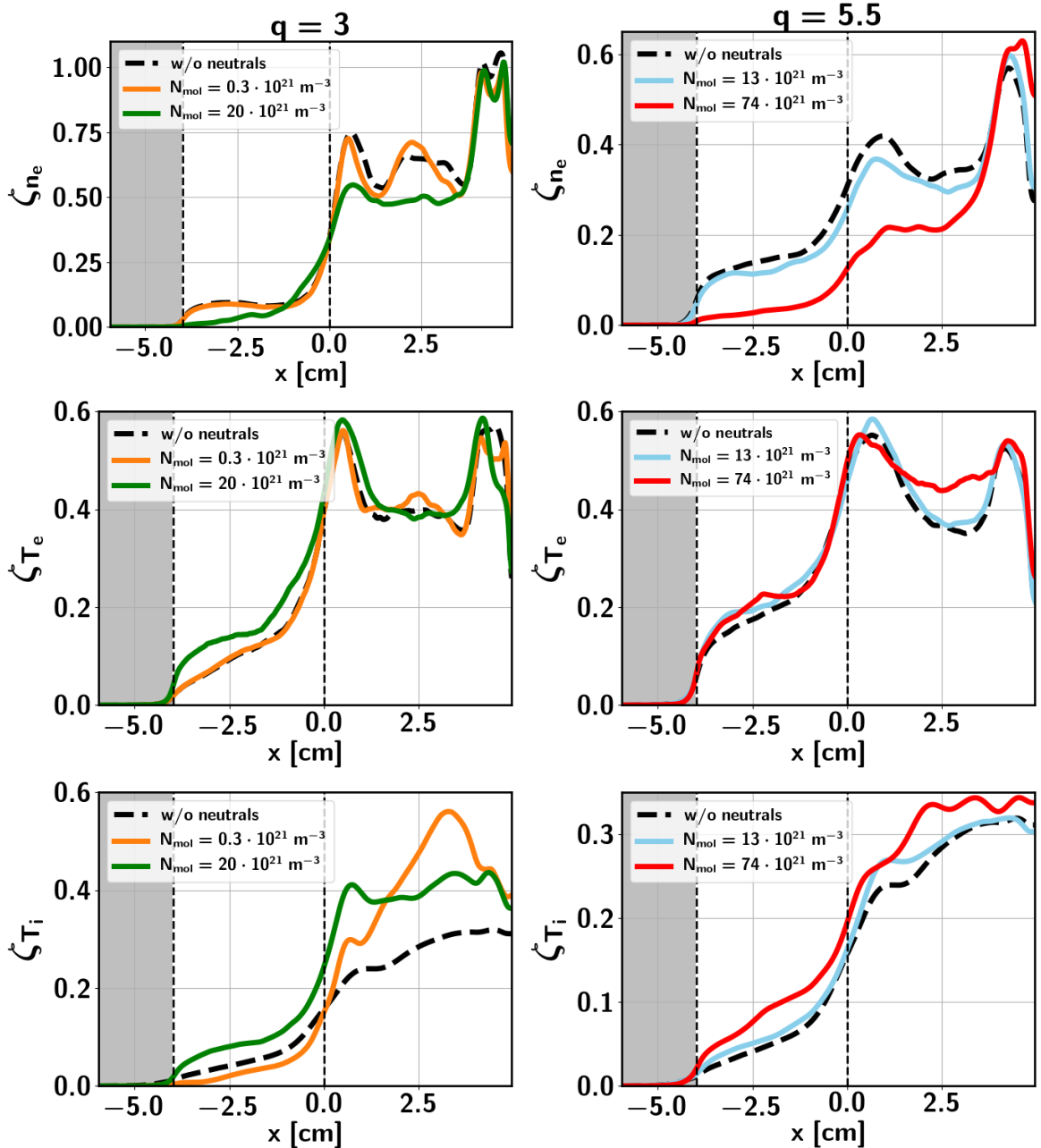


Figure 5.61: Fluctuation level radial profiles for the plasma density, electron and ion temperature. Initial simulations parameters correspond to the cases *I1-q3*, *I2-B-q3* and *I2* and *I4* in Table 5.1

Variance describes the deviation of the signal from the mean value. Smaller variance indicates more homogeneous distribution. Radial distributions of variance of the plasma density is shown in Fig. 5.63. Although, Fig. ?? shows the decrease of the fluctuation level in the SOL when high intensity neutral beam is injected, but the variance in SOL at the same time is higher (Fig.5.63) this is stands together. Together with the variance the mean value of plasma density increased that might be resulted in lower fluctuation level of plasma density fluctuations.

Third statistical moment gives the skewness (S) which describes the symmetry of

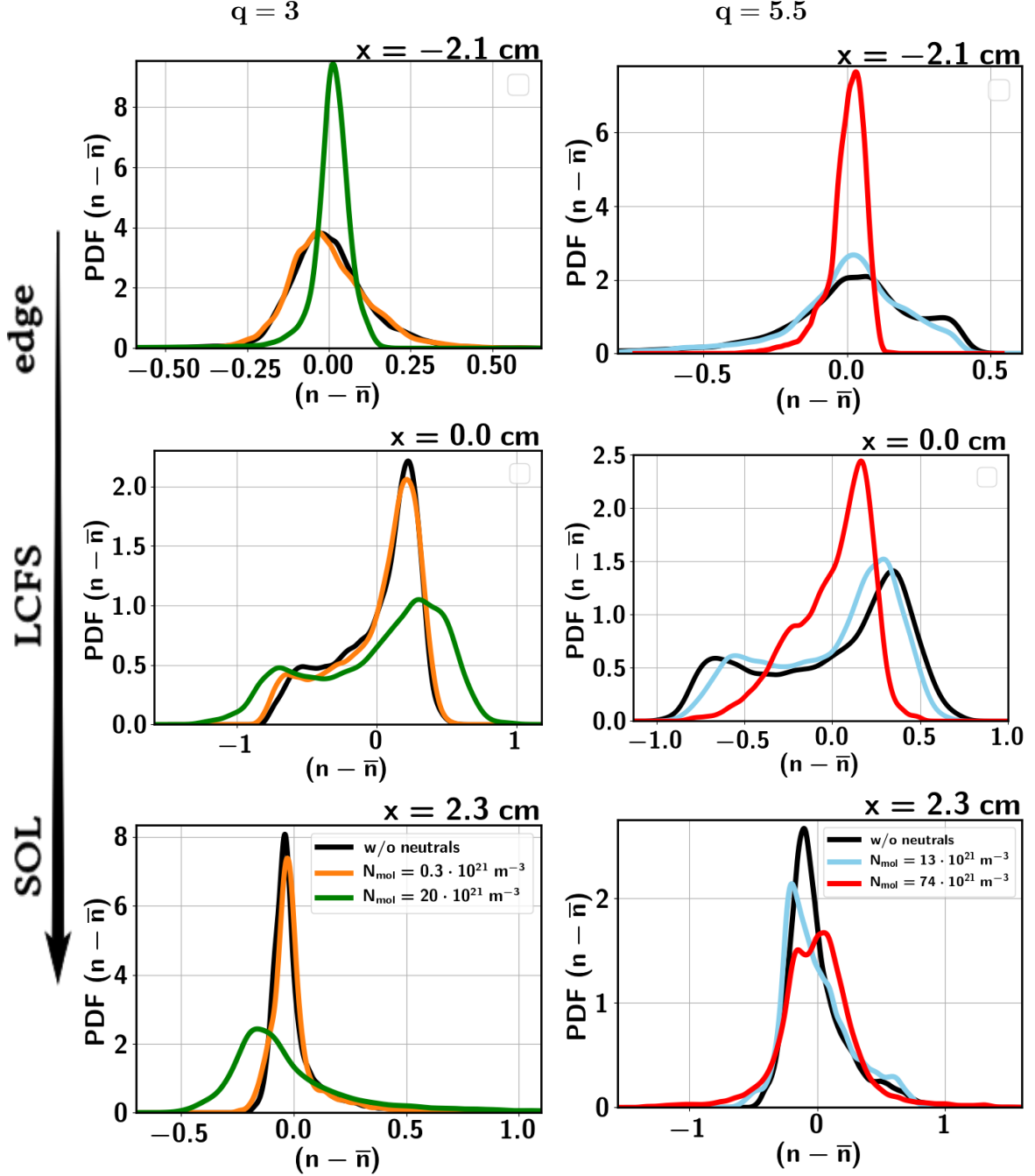


Figure 5.62: PDF functions of the normalized plasma density. Initial simulations parameters correspond to the cases *I1-q3*, *I2-B-q3* and *I2* and *I4* in Table 5.1

the distribution

$$S = \frac{\langle (n - \langle n \rangle)^3 \rangle}{\sigma^3}. \quad (5.26)$$

The positive skewness indicates the dominance of the positive blob events, while the negative skewness indicates the higher probability of holes. Skewness of the Gaussian distribution is equal to zero. The region of zero skewness is believed to be close to the birth-zone of the blobs and holes [67]. In simulations without neutral injection or with a small amount of injected particles the birth-zone in the vicinity of LCFS as seen in

Fig. 5.63. The high neutral injection in simulations with $q = 5.5$ gives the skewness equals to zero in the SOL region. This indicates the plasma density is described by the Gaussian distribution function in the SOL region. In simulations with $q = 3$ skewness decreased after high intensity neutral injection. This is likely caused by the increase of the averaged density in the SOL during SMBI.

The forth moment of the distribution function is a kurtosis (K), which describes the "peakedness" of the distribution function.

$$K = \frac{\langle (n - \langle n \rangle)^4 \rangle}{\sigma^4} \quad (5.27)$$

However, it is more convenient to use a flatness instead of kurtosis, which is equal to $F = K - 3$. For the Gaussian function flatness is equal to 0. Positive flatness indicates the higher probability of the big events, while the negative flatness characterises the signal with less frequent and smaller fluctuations. The radial distribution of the flatness (Fig. 5.63) shows the tendency of the distribution function of plasma density in the SOL region to approach the Gaussian distribution with increase of the intensity of injected neutrals. The scatter plot of the plasma density fluctuations over temperature fluctuations (Fig. 5.64) reveals the change in the relation between them. Temperature and density fluctuations becomes uncorrelated after the SMBI, while the strong correlation was observed before the injection.

Analysis of the particle flux across the LCFS shows the decrease of the particle flux with increase of the neutral injection rate (Fig. 5.65). The PDF function of the particle flux has the positive tail in case without neutral injection, while the strong neutral injection leads to the nearly symmetric Gaussian distribution as seen in Fig. 5.65.

Decrease of the poloidal velocity is observed in case of the strong neutral injection as seen in Fig. 5.66. The turbulence flux is driven by the pressure gradient. As seen from the skewness radial profile (Fig. 5.63) the birth zone of blobs and holes locates at the LCFS. The decrease of the pressure gradient (5.67.), in particular ion pressure at LCFS is the reason of observed decrease of the particle flux across the LCFS.

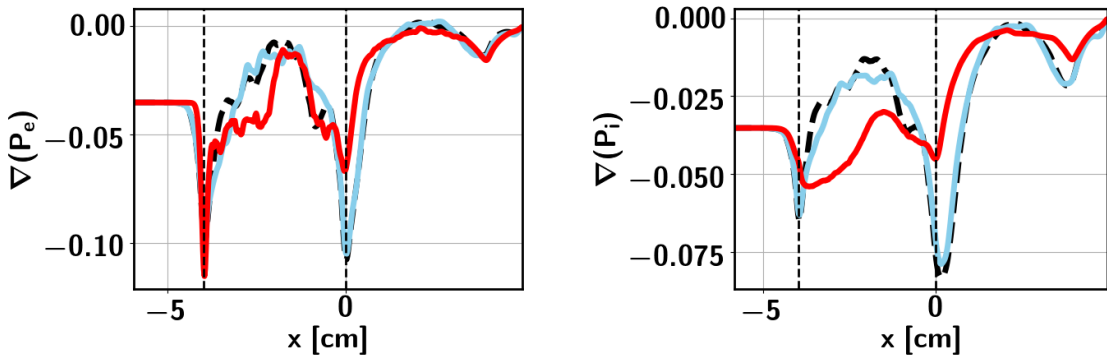


Figure 5.67: Gradients of the ion and electron pressure. Initial simulations parameters correspond to the cases $I2$ and $I4$ in Table 5.1

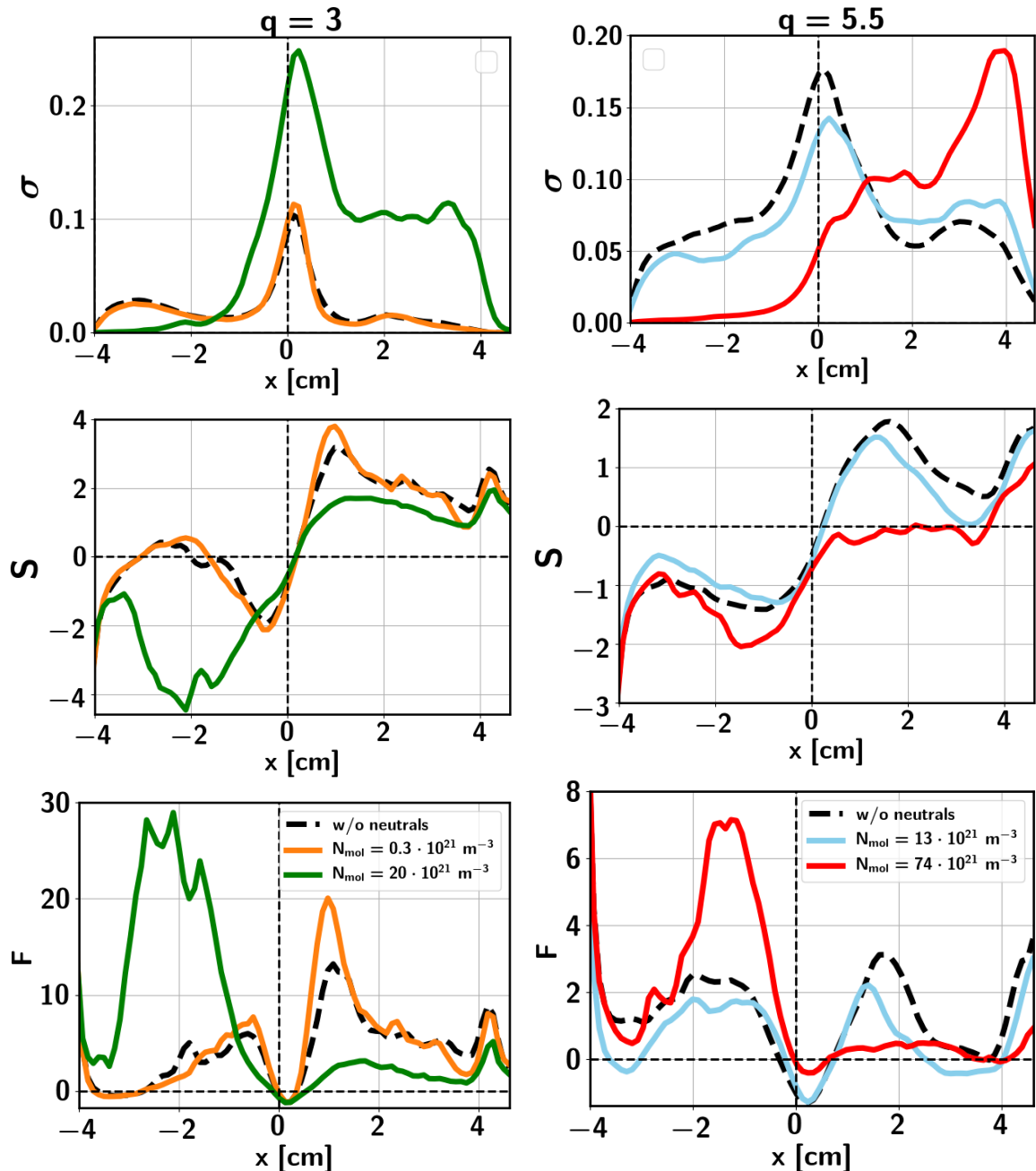


Figure 5.63: Radial distributions of the statistical moments for the normalized plasma density. Initial simulations parameters correspond to the cases I1-q3, I2-B-q3 and I2 and I4 in Table 5.1.

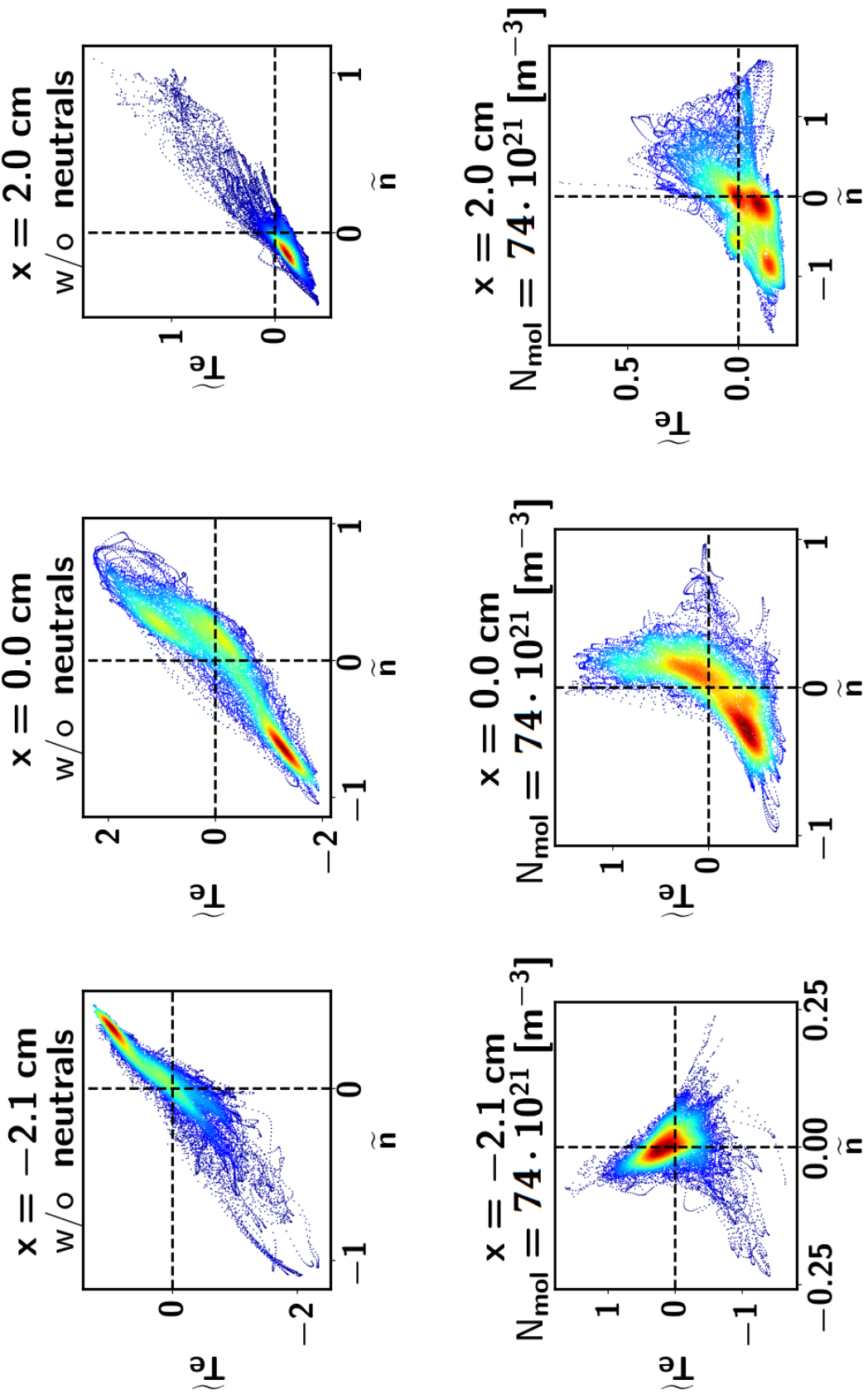


Figure 5.64: Scatter plot of the plasma density fluctuations over the temperature fluctuations. Initial simulations parameters correspond to the case I_4 in Table 5.1

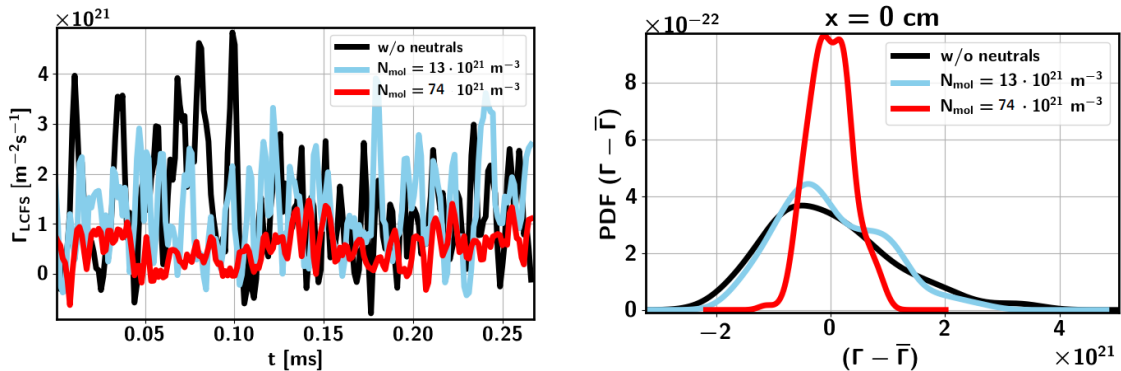


Figure 5.65: Radial particle flux across the LCFS (left) and probability density function of the particle flux (right).

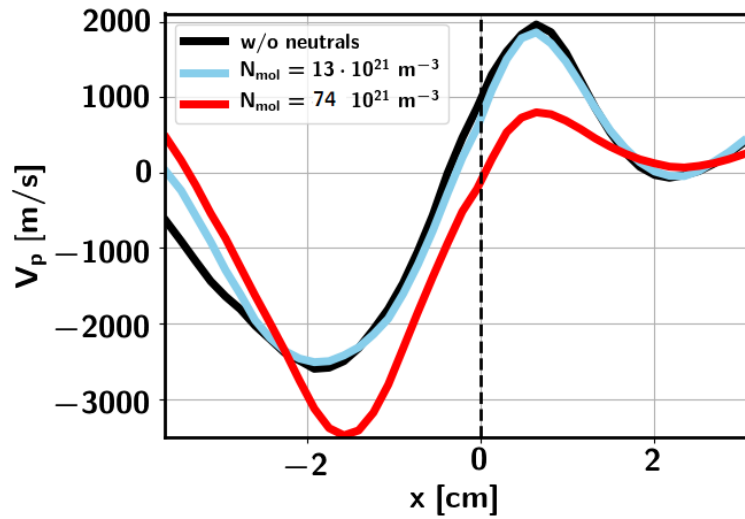


Figure 5.66: Poloidal velocity profiles. Initial simulations parameters correspond to the cases I2 and I4 in Table 5.1

5.4.2 Dependence on the beam width

The similar statistical analysis was performed for the data from the beam width scan with the large injection flux $\langle \Gamma_{inj} \rangle^{large} = 74 \cdot 10^{24} m^{-2}s^{-1}$. The similar trend of the decrease of the plasma density fluctuation level without changes in electron temperature fluctuation level is observed. The wide beam decreases the plasma density fluctuation level more compared to the narrow beam Fig. 5.68. The decrease of the radial flux is

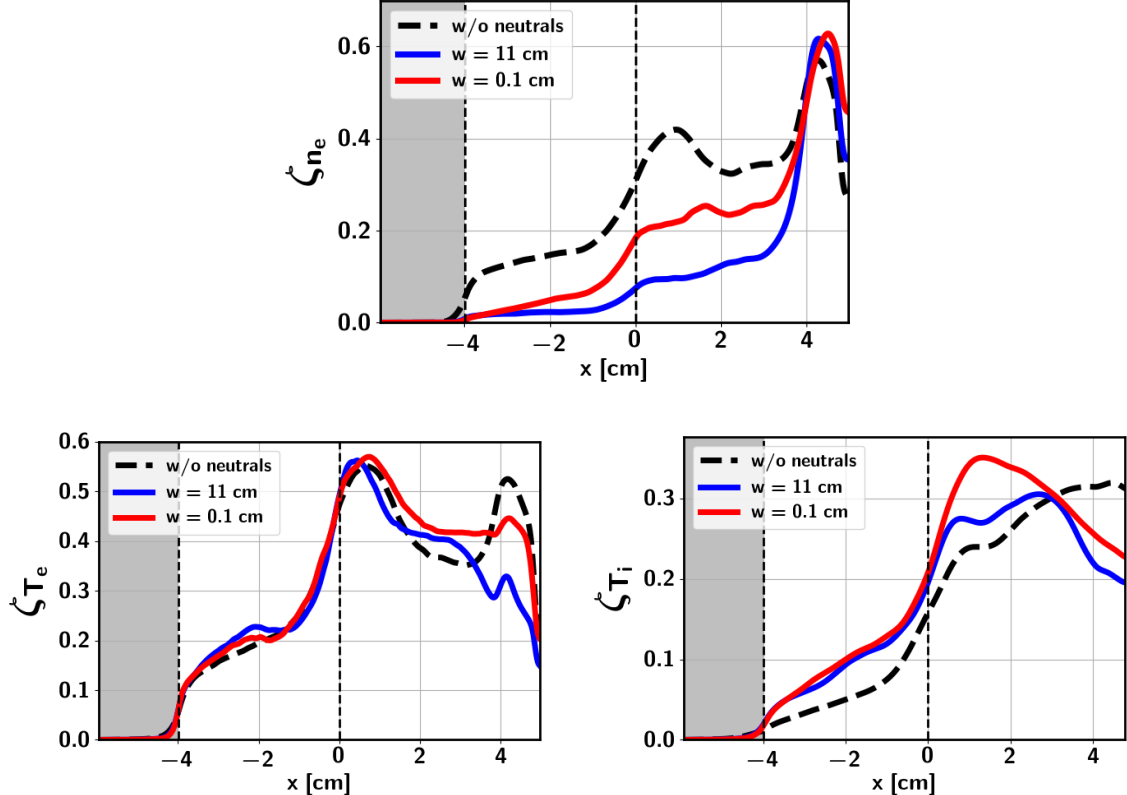


Figure 5.68: Fluctuation level radial profiles for the plasma density, electron and ion temperature

observed in both cases of neutral injection (Fig. 5.69) . The variance, skewness and flatness of PDFs of the particle flux across the LCFS for different injection scenarios are summarized in Table 5.6. Skewness decreases with increase of injected neutral density and indicates the tendency of the distribution function of the particle flux to approach the Gaussian distribution function.

statistical moment	w/o neutrals	$w = 11\text{ cm}$	$w = 0.1\text{ cm}$
F	0.46	0.69	0.41
S	0.74	0.55	0.39
$\sigma [m^{-2}s^{-1}]$	$1.12 \cdot 10^{21}$	$2.3 \cdot 10^{20}$	$5.2 \cdot 10^{20}$

Table 5.6: Statistical moments of the radial particle flux across the LCFS

The plasma velocity profiles and velocity shear are shown in Fig. 5.70 and the gradients of the electron and ion pressure in Fig. 5.71. The higher velocity shear in

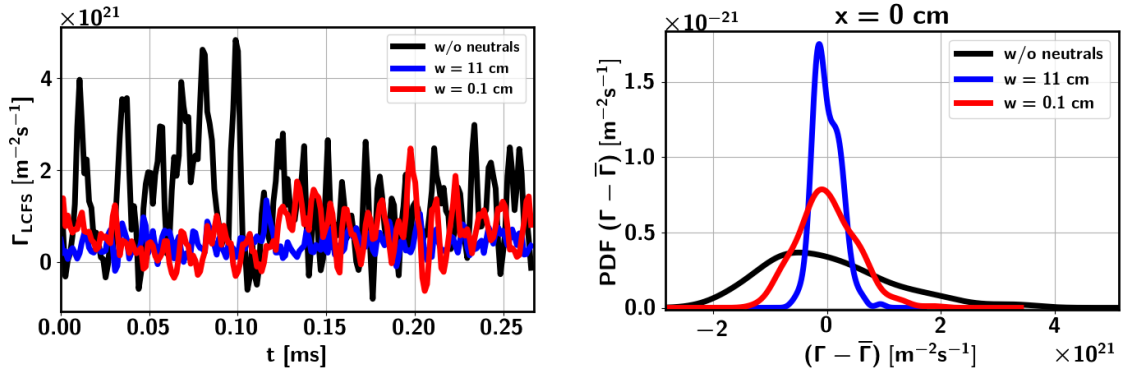


Figure 5.69: Radial particle flux across the LCFS (left) and probability density function of the particle flux (right).

case of the wide neutral beam might be a reason of the lower fluctuation level observed in this simulations, since the decrease of pressure gradients caused by the neutral injection are similar in both cases.

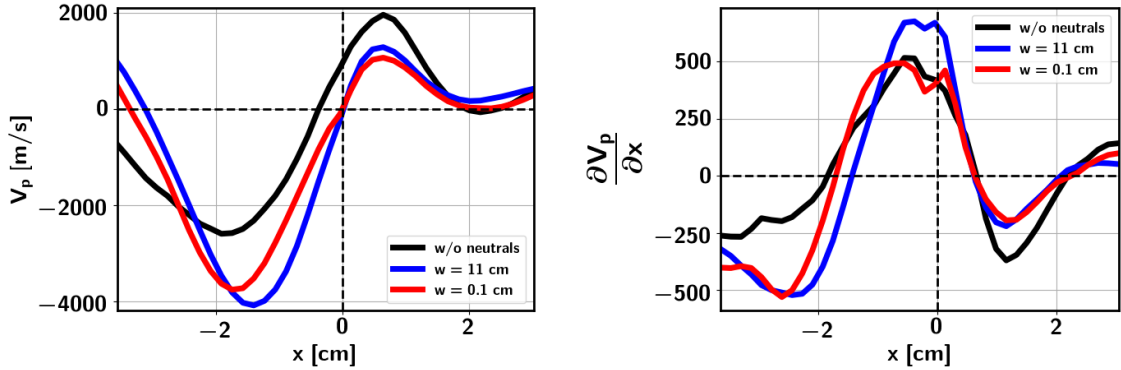


Figure 5.70: Poloidal velocity and the velocity shear

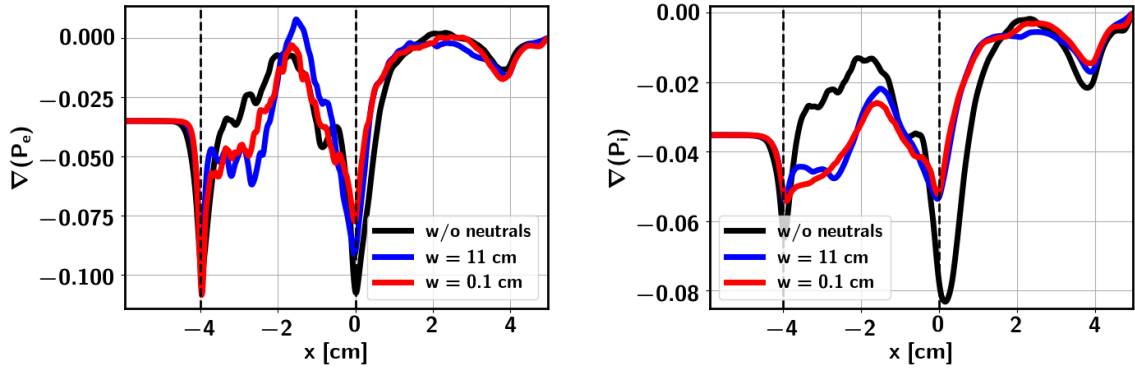


Figure 5.71: Gradients of the ion and electron pressure

5.4.3 Dependence on the beam velocity

The similar analysis for the velocity scan indicates that the decrease of the plasma density fluctuation level depends on the injection density rather the velocity. The PDFs of the particle flux across the LCFS in simulations with low injection flux shows the difference in case of the neutrals with high injection velocity. This is due to deeper penetration of the neutral and higher source in plasma edge. For the high injection flux the decrease of the fluctuation level is observed, but no difference between the low and high speed injections (Fig. 5.72), although the pressure gradient is smaller in simulations with the high velocity (Fig. 5.73).

Summary

SMBI affects on the plasma fluctuations if the neutral density is higher the critical density. The influence of SMBI on plasma transport results in reduction of the fluctuation level for the plasma density and modification PDFs for the plasma density fluctuations approaches the Gaussian functions with increase of the neutral injection rate. Plasma density and temperature fluctuations do not correlate after SMBI although the strong correlation was observed before. Reduction of the turbulent particle flux after SMBI is explained by the decrease of the plasma gradients. Effect of the beam size appears through the the higher density of the narrow beam. The decrease of the plasma gradients is bigger with the dense narrow beam but at the same time this beam creates local dense source and hereby enhances the fluctuation level for the plasma density. No effect of the beam velocity on the plasma fluctuations was observed.

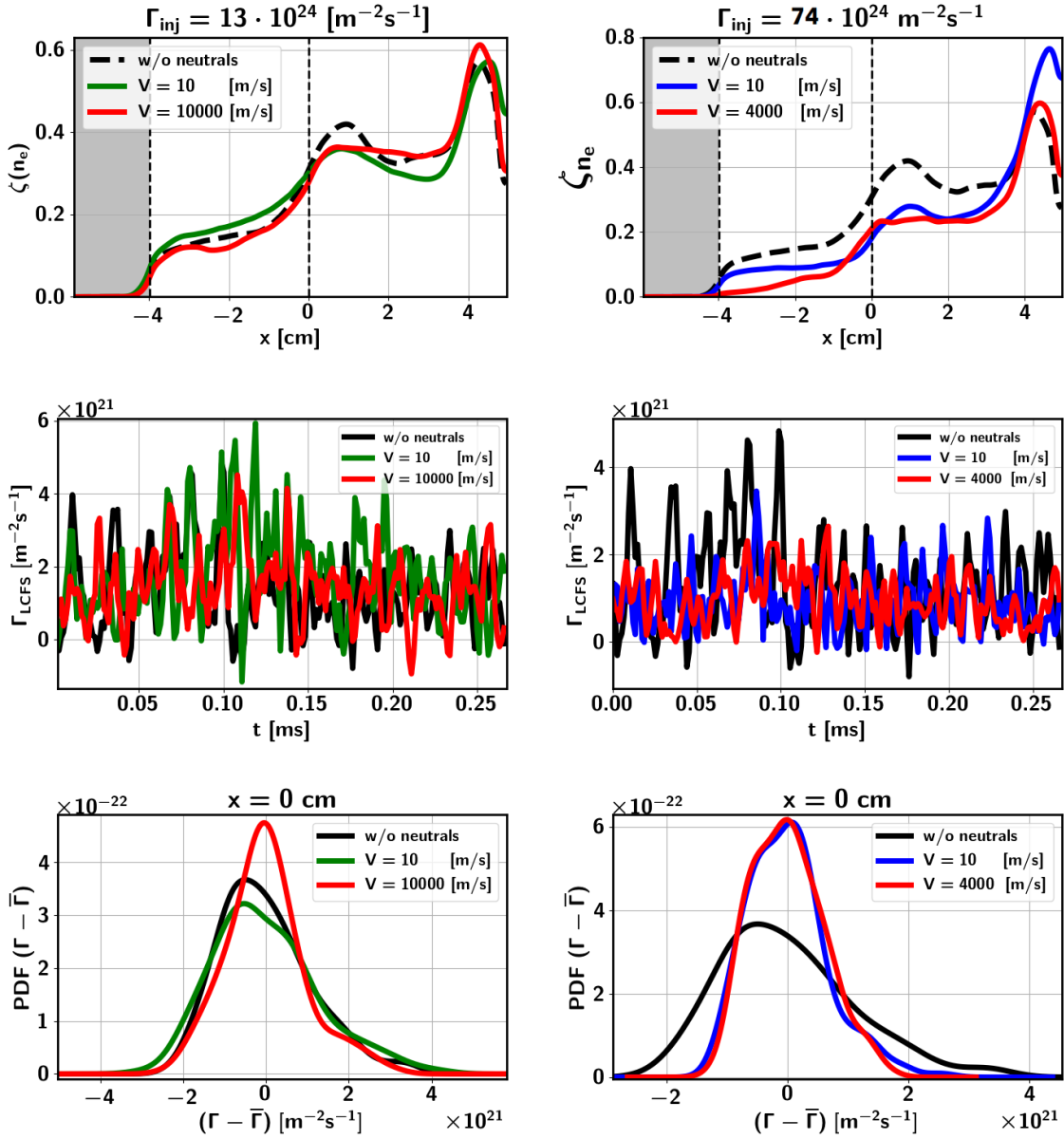


Figure 5.72: Fluctuation level for plasma density (first row), particle flux across the LCFS (second row) and PDFs of the particle flux across LCFS (third row).

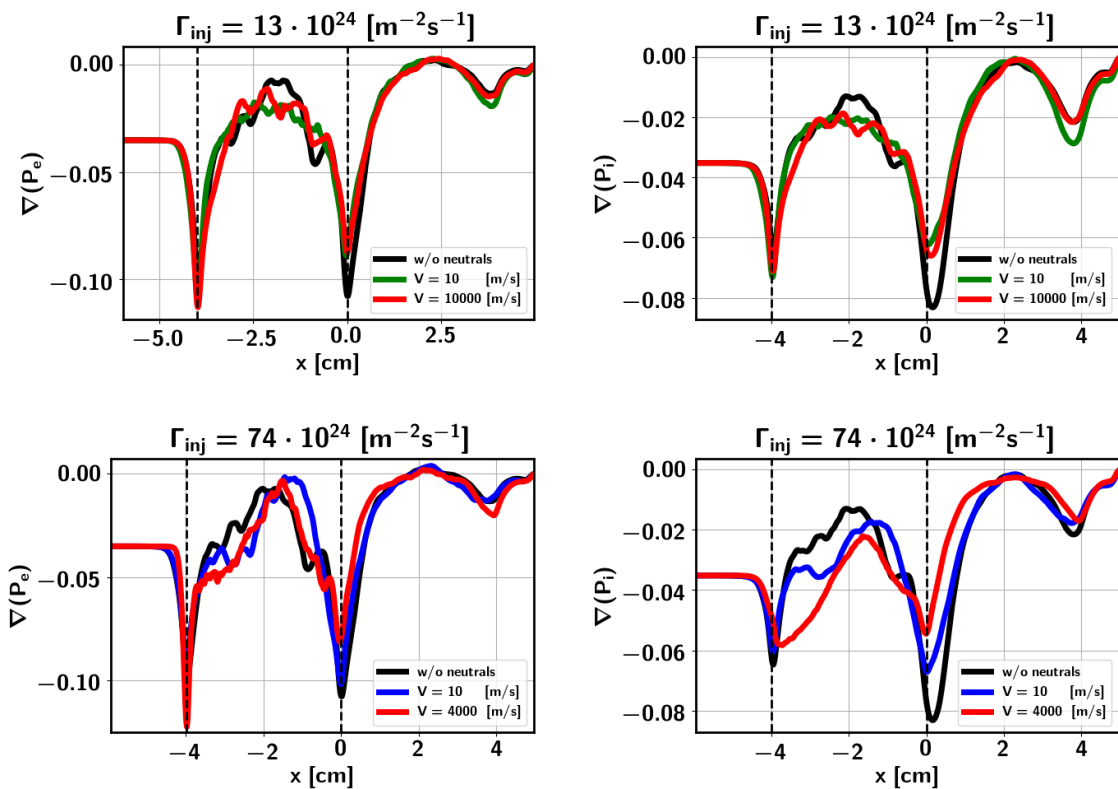


Figure 5.73: Gradients of the ion and electron pressure.

5.5 Influence of plasma fluctuations on SMB penetration

As known the transport in SOL region is intermittent and characterized by the density and temperature fluctuation with amplitude up to 100% [65, 66]. This affects on the neutral propagation through the SOL region. The investigation of the influence on plasma turbulence on the neutrals in SOL region was performed in several works [63, 68–70] and the importance of the inclusion of the turbulent plasma transport in an analysis of the neutral particle penetration through the SOL was mentioned. However, no analogical research was performed for the supersonic molecular beam, which has some essential differences from the thermal neutrals governed by diffusion equation. First, this is the high direct velocity, which makes the mean free part of injected molecules much longer. The smaller effect of the turbulence on the neutrals with a long mean free path is expected [70], [69]. Another essential difference is the narrow localization of the beam. Only filaments on the beam penetration front will affect the supersonic molecular beam. This can be analogy of the comparison of 1D dynamical model with a 2D as was done in [68], where the smaller discrepancy between the dynamical model and mean-field approximation was observed in 2D simulation compared to 1D. That was explained by the smaller size of blobs in 2D simulations compared to the size of domain.

In order to study the influence of plasma fluctuations on the penetration of the supersonic molecular beam the comparison of the simulations with the full dynamic model "plasma dynamic" with the simulations using the mean-field approximation ("plasma steady") where the dynamics plasma profiles are replaced by the time averaged fields was done. The initial parameters of simulations correspond to the cases *I3-W* in the Table 5.1, and cases *I4-BN* and *I4-F* in the Table 5.2. As was shown in section 5.4 the neutral injection modifies the fluctuation level of plasma turbulence, therefore the case "without neutral source" in the model is considered first. Comparison of the density source profiles is shown in Fig. 5.74. As seen from the picture, the discrepancy between profiles obtained by dynamic model and by the mean field approximation is not pronounced although the fluctuations of the density source in the SOL region is observed in Fig. 5.74. The difference between mean values of ionization source in the SOL region calculated in dynamical model and by the mean field approximation is 2.4 %.

Then the similar comparison was done for the simulations with a wide injection beam and narrow injection beam. The results are shown in Fig. 5.75. The deviations between mean values calculated by different models is 0.6 % and 1.8 % for the wide beam and narrow beam respectively. Comparing all of this results we can conclude that the effect of the plasma fluctuations on the density source produced by the supersonic molecular beam is not significant. The level of the density source fluctuation is proportional to the amplitude of density source. Fluctuation level of the density source is shown in Fig. 5.76. The left column shows the fluctuations of the density source around the poloidally and time averaged value. The right column shows the fluctuations of the density source around time averaged value in the poloidal center of the domain. Only range of $\pm 20\%$ from the mean value is shown. Different spatial distribution of fluctuations is visible. The less frequent but higher amplitude fluctuations of the is observed in case of the narrow beam injection. Fluctuations of the density source in case of the width beam injection have less amplitude and distribute

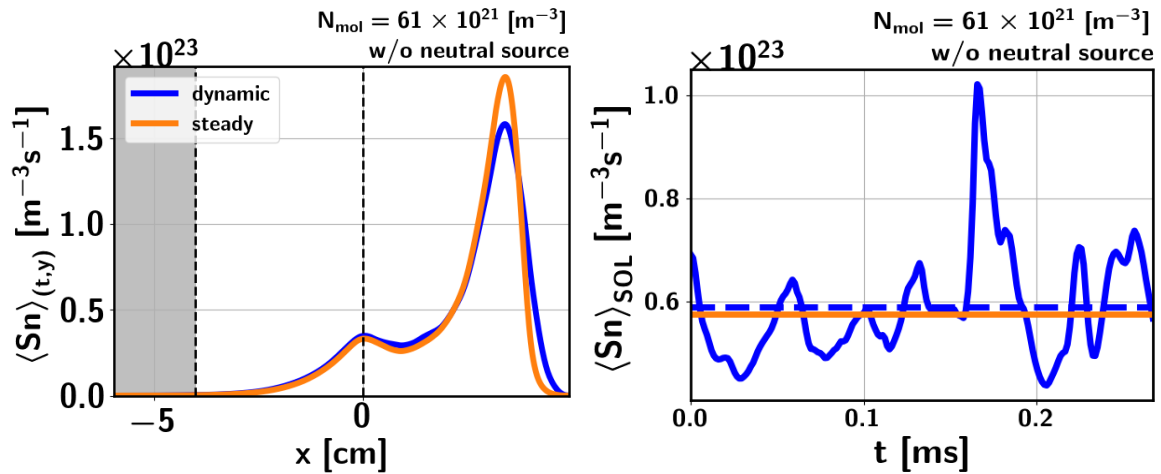


Figure 5.74: Comparison of the density source in the fill dynamic model and in the simulations with the mean-field approximation. The initial parameters of simulations correspond to the cases *I3-W* in the Table 5.1.

more homogeneous. This indicates that the fluctuation level for the density source is proportional to the density of the injected neutrals.

Summary

Fluctuations of the density source are proportional to the intensity of the injected molecular beam. The mean-field approximation provided radial profiles of the density in a good agreement with dynamical model.

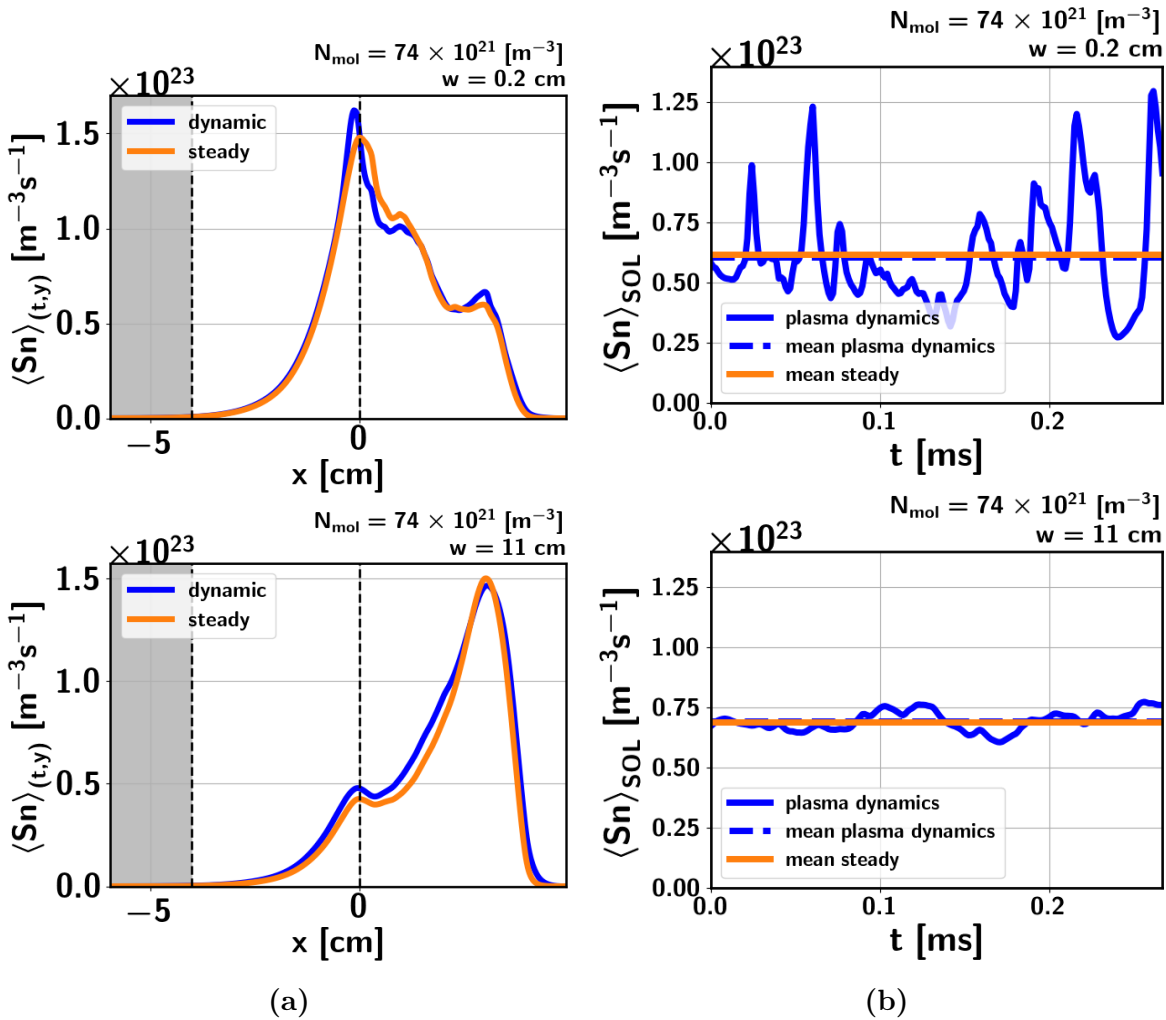


Figure 5.75: Comparison of the density source in the fill dynamic model and in the simulations with the mean-field approximation. The initial parameters of simulations correspond to the cases *I4-NB* and *I4-F* in the Table 5.1.

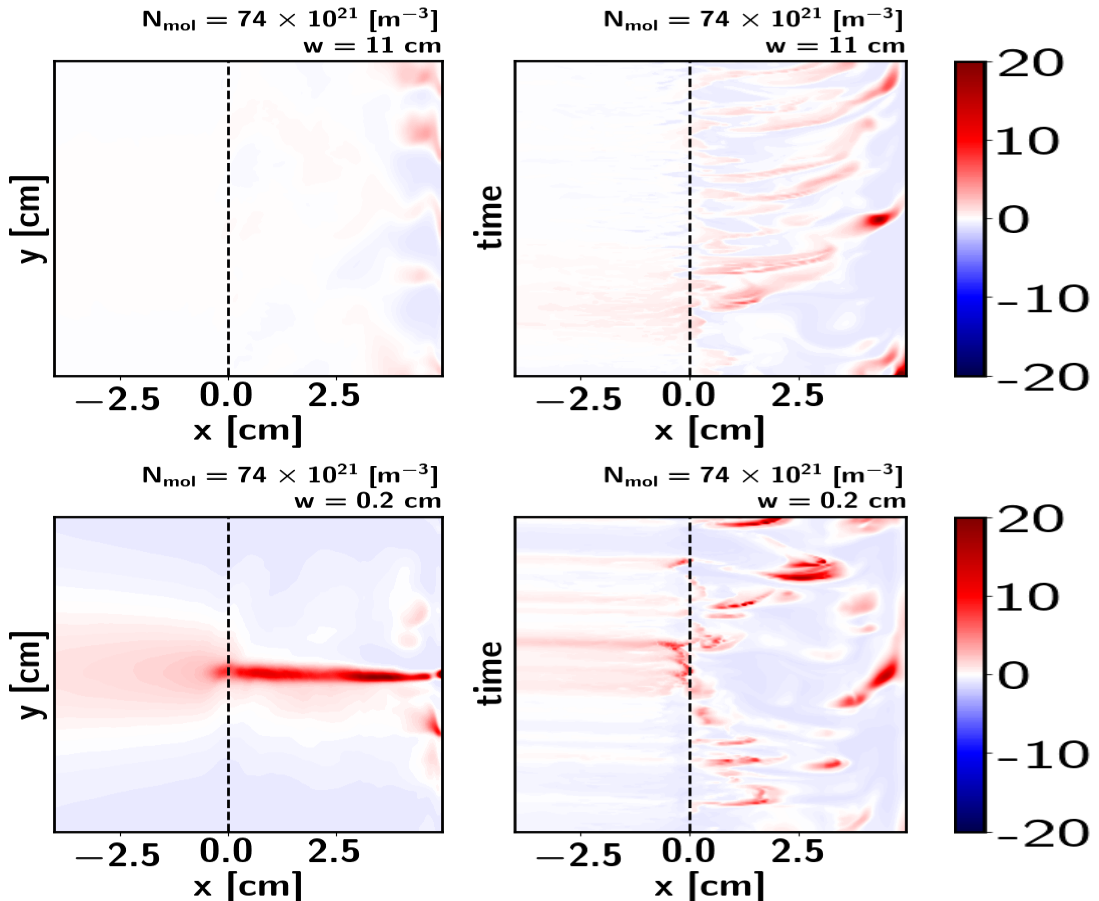


Figure 5.76: Fluctuation level of the density source. The left column shows the fluctuations of the density source around the poloidally and time averaged value. The right column shows the fluctuations of the density source around time averaged value in the poloidal center of the domain. The initial parameters of simulations correspond to the cases *I4-NB* and *I4-F* in the Table 5.2.

Chapter 6

Conclusions

The importance of the plasma refuelling during the tokamak operations ensues from the radial transport which leads to particle and energy losses. Efficient fuelling method should provide the penetration of the neutral particle in confine region and minimize the amount of neutrals ionized in the SOL. SMBI is the fuelling method which is not more complicated as a gas puffing system but demonstrates the higher efficiency. The fuelling properties as well as impact of this method on plasma depending on the beam parameters was investigated in this thesis.

The investigation started from the literature review to highlight the main features of SMBI observed in experiments and level of understanding of physics behind the supersonic beam - plasma interactions. The possibility of using SMBI for mitigation of ELMs and high amplitude plasma fluctuations was demonstrated in experiments, however the mechanisms of the influence of SMBI on plasma transport has not been understood yet and no self-consistent simulations of SMBI -plasma dynamics has been performed. The demand of the investigation of plasma-neutral interactions self consistently with plasma dynamics was revealed from the literature rewire.

In order to simulate SMBI the parameters of the molecular beam are calculated based on the isotropic relations for the nozzle flow. Calculations are performed for SMBI system on KSTAR, which works in two regimes: with working gas at the room temperature and working gas at the low temperature (105 K). Calculations showed that the molecular flux in around two higher in case of the gas at low temperature compared to the working gas at the room temperature. Calculations are in agreement with the calibration data. Comparison of the line integrated density measured on KSTAR in shots with GP and SMBI in different working regimes show the different response of plasma on various fuelling methods. The highest increase of plasma density is observed in short with SMBI working with the gas at low temperature.

The numerical investigation using the drift-fluid model provided the following results. No self-shielding effect was observed in the simulations with plasma dynamics. Increase of the injection neutral density leads to the stronger decrease of the plasma temperature and consequently deeper penetration of neutrals in plasma.

Increase of the beam injection density leads to the deeper penetration of neutrals due to decrease of the plasma temperature and reduction of the reaction rates. The dependency of the fuelling efficiency from the molecular density depends on the plasma conditions and grows weaker with increase of the plasma parameters. Since the dependence of the ionization efficiency on the molecular beam intensity is not so strong to explain the difference in plasma response on SMBI with the room temperature gas

and low temperature gas on KSTAR the clustering effect might took place in those experiments. Another reason can be high ration of the molecular beam density to the plasma density sources on KSTAR and consequently stronger dependence of the efficiency from the molecular density. The critical molecular density was found in the simulations, which is defined as the density providing the density source in the edge region comparable to the forcing density source. Fuelling efficiency grows faster with increase of the molecular density beyond the critical level. More than 90 % of the density source in the edge region is produced by the ionization of Franck-Condon atoms and the rest is produced by ionization of molecules. The contribution of the molecular ionization to the density source grows with increase of the molecular beam intensity.

Ionization efficiency grows with increase of the velocity of injected molecules. The dependency of the ionization efficiency on the injection velocity grows weaker with increase of the plasma conditions. Independently on the molecular beam intensity the increase of the direct velocity leads to the deeper penetration of neutrals and enhance of the fuelling efficiency.

Influence of the beam width on the neutral penetration and ionization efficiency is not observed in simulations with low q or low injection neutral flux. If the injection flux is higher the critical value or plasma parameters are increased the ionization efficiency is higher in case of injection of the narrow dense beam.

SMBI affects on the plasma fluctuations if the neutral density is higher the critical density. The influence of SMBI on plasma transport results in redaction of the fluctuation level for the plasma density and modification PDFs for the plasma density fluctuations approaches the Gaussian functions with increase of the neutral injection rate. Plasma density and temperature fluctuations do not correlate after SMBI although the strong correlation was observed before. Reduction of the turbulent particle flux after SMBI is explained by the decrease of the plasma gradients. Effect of the beam size appears through the the higher density of the narrow beam. The decrease of the plasma gradients is bigger with the dense narrow beam but at the same time this beam creates local dense source and hereby enhances the fluctuation level for the plasma density. No effect of the beam velocity on the plasma fluctuations was observed.

Fluctuations of the density source are proportional to the intensity of the injected molecular beam. The mean-field approximation provided radial profiles of the density in a good agreement with dynamical model.

Bibliography

- [1] J. Wesson and D. Campbell, *Tokamaks*. International series of monographs on physics, Clarendon Press, 2004.
- [2] S. Li, H. Jiang, Z. Ren, and C. Xu, “Optimal tracking for a divergent-type parabolic pde system in current profile control,” *Abstract and Applied Analysis*, vol. 2014, pp. 1–8, 01 2014.
- [3] J. E. Barton, W. P. Wehner, E. Schuster, F. Felici, and O. Sauter, “Simultaneous closed-loop control of the current profile and the electron temperature profile in the tcv tokamak,” in *2015 American Control Conference (ACC)*, pp. 3316–3321, July 2015.
- [4] S. Abdullaev, K. Finken, M. Jakubowski, and M. Lehnhen, “Mappings of stochastic field lines in poloidal divertor tokamaks,” *Nuclear Fusion*, vol. 46, pp. S113–S126, 05 2006.
- [5] X. Gao, Y. Jie, C. Xia, M. Wei, Y. Yang, S. Zhang, J. Zhao, L. Hu, Y. Zhu, J. Luo, Y. Zhao, N. Qiu, J. Li, B. Wan, G. Kuang, X. Zhang, X. Liu, X. Gong, Y. Bao, B. Lin, Z. Wu, Y. Li, Y. Shi, M. Song, P. Fu, X. Zhang, M. Zeng, A. Xie, N. Cui, H. Ruan, L. Wang, B. Sheng, S. Liu, W. Ye, K. Yang, J. Liu, Y. Cheng, H. Fan, S. Liu, X. Tong, J. Mao, X. Gu, J. Xie, and Y. Wan, “High density operation on the HT-7 superconducting tokamak,” *Nucl. Fusion*, vol. 40, no. 11, pp. 1875–1883, 2000.
- [6] L. Yao, Y. Zhou, J. Cao, B. Feng, Z. Feng, J. Luo, J. Dong, L. Yan, W. Hong, K. Li, Z. Cui, Y. Liu, E. Wang, and J. Yan, “Hydrogen cluster-like behaviour during supersonic molecular beam injection on the HL-1M tokamak,” *Nucl. Fusion*, vol. 41, no. 7, pp. 817–826, 2001.
- [7] Y. Kamada, R. Yoshino, M. Nagami, T. Ozeki, T. Hirayama, H. Shirai, H. Nakamura, H. Kimura, T. Fujii, K. Kawasaki, H. Hiratsuka, Y. Miyo, K. Nagashima, H. Yoshida, and T. Nishitani, “Improved confinement characteristics of pellet fuelled discharges on JT-60,” *Nuclear Fusion*, vol. 29, pp. 1785–1798, oct 1989.
- [8] A. Stabler, K. McCormick, V. Mertens, E. Muller, J. Neuhauser, H. Niedermeyer, K.-H. Steuer, H. Zohm, F. Dollinger, A. Eberhagen, G. Fussmann, O. Gehre, J. Gernhardt, T. Hartinger, J. Hofmann, E. Kakoulidis, M. Kaufmann, G. Kyriakis, R. Lang, H. Murmann, W. Poschenrieder, F. Ryter, W. Sandmann, U. Schneider, G. Siller, F. Soldner, N. Tsois, O. Vollmer, and F. Wagner, “Density limit investigations on ASDEX,” *Nuclear Fusion*, vol. 32, pp. 1557–1583, sep 1992.

- [9] T. Eich, R. Goldston, A. Kallenbach, B. Sieglin, H. Sun, and and, “Correlation of the tokamak h-mode density limit with ballooning stability at the separatrix,” *Nuclear Fusion*, vol. 58, p. 034001, jan 2018.
- [10] J. Bucalossi, G. Martin, R. Dejarnac, A. Géraud, C. Gil, R. Guirlet, J. Gunn, T. Loarer, B. Pégourié, E. Tsitrone, A. Euratom-cea, D. D. Recherche, and F. Contrôle, “Plasma Fuelling by Pulsed Supersonic Gas Injection on Tore Supra,” vol. 26, no. June, pp. 2–5, 2002.
- [11] A. Murakami, J. Miyazawa, C. Suzuki, I. Yamada, T. Morisaki, R. Sakamoto, and H. Y. and, “Fueling characteristics of supersonic gas puffing applied to large high-temperature plasmas in the large helical device,” *Plasma Physics and Controlled Fusion*, vol. 54, p. 055006, apr 2012.
- [12] S. L. Milora, W. A. Houlberg, L. L. Lengyel, and V. Mertens, “Review paper: Pellet fuelling,” *Nucl. Fusion*, vol. 35, p. 657, 1995.
- [13] J. Chung, H. Kim, Y. Jeon, J. Kim, M. Choi, J. Ko, K. Lee, H. Lee, S. Yi, J. Kwon, S.-H. Hahn, W. Ko, J. Lee, and S. Yoon, “Formation of the internal transport barrier in KSTAR,” *Nuclear Fusion*, vol. 58, p. 016019, nov 2017.
- [14] L. Yao, “Supersonic molecular beam injection in fusion plasma,” *Nova Science Publishers, Inc*, p. 61, 2006.
- [15] D. Yu, C. Chen, L. Yao, B. Feng, X. Han, L. Yang, W. Zhong, Y. Zhou, K. Zhao, Y. Huang, Y. Liu, L. Yan, Q. Yang, J. Dong, and X. Duan, “Penetration characteristics of supersonic molecular beam injection on HL-2a tokamak,” *Nuclear Fusion*, vol. 50, p. 035009, mar 2010.
- [16] J. Bucalossi, P. T. Lang, G. Martin, V. Mertens, J. Neuhauser, V. Rohde, L. Fattorini, and A. U. Team, “Supersonic Molecular Beam Fuelling at ASDEX Upgrade,” vol. 28G, pp. P—4.115, 2004.
- [17] J. W. Juhn, S. H. Hahn, S. H. Hong, J. I. Song, Y. O. Kim, K. P. Kim, J. S. Kim, and KSTAR Team, “Particle balance study for the fueling efficiency in kstar experiments 2013,” *Journal of the Korean Physical Society*, vol. 65, pp. 1304–1311, Oct 2014.
- [18] B. Pégourié, E. Tsitrone, R. Dejarnac, J. Bucalossi, G. Martin, J. Gunn, D. Frigione, D. Reiter, P. Ghendrih, and C. Clément, “Supersonic gas injection on Tore Supra,” *J. Nucl. Mater.*, vol. 313–316, no. SUPPL., pp. 539–542, 2003.
- [19] P. Lang, G. Conway, T. Eich, L. Fattorini, O. Gruber, S. Günter, L. Horton, S. Kalvin, A. Kallenbach, M. Kaufmann, G. Kocsis, A. Lorenz, M. Manso, M. Maraschek, V. Mertens, J. Neuhauser, I. Nunes, W. Schneider, W. Suttrop, H. Urano, and the ASDEX Upgrade Team, “ELM pace making and mitigation by pellet injection in ASDEX upgrade,” *Nuclear Fusion*, vol. 44, pp. 665–677, apr 2004.
- [20] L. Yao, D. Zhao, B. Feng, C. Chen, Y. Zhou, X. Han, Y. Li, J. Bucalossi, and X. Duan, “Plasma Science and Molecular Beam Injection from Both Low Field Side and High Field Side of HL-2A,” *Plasma Sci. Technol.*, vol. 12, no. 5, p. 529, 2010.

- [21] R. Klingelhöfer and H. O. Moser, “Production of large hydrogen clusters in condensed molecular beams,” *J. Appl. Phys.*, vol. 43, no. 11, pp. 4575–4579, 1972.
- [22] L. H. Yao and et all
- [23] L. Yao, N. Tang, Z. Cui, D. Xu, Z. Deng, X. Ding, J. Luo, J. Dong, G. Guo, S. Yang, C. Cui, Z. Xiao, D. Liu, X. Chen, L. Yan, D. Yan, E. Wang, and X. Deng, “Plasma behaviour with molecular beam injection in the HL-1M tokamak,” *Nucl. Fusion*, vol. 38, no. 4, pp. 631–638, 1998.
- [24] O. F. Hagena and W. Obert, “Cluster formation in expanding supersonic jets: effect of pressure, temperature, nozzle size and test gas,” vol. 56, no. 5, p. 1793, 1972.
- [25] O. F. Hagena, “Nucleation and growth of clusters in expanding nozzle flows,” *North-Holland Publishing Company*, vol. 106, pp. 101 – 116, 1981.
- [26] D. Yu, C. Chen, L. Yao, J. Dong, B. Feng, Y. Zhou, Z. Shi, J. Zhou, X. Han, W. Zhong, C. Cui, Y. Huang, Z. Cao, Y. Liu, L. Yan, Q. Yang, X. Duan, and Y. Liu, “Study of the high fuelling efficiency features of supersonic molecular beam injection,” *Nuclear Fusion*, vol. 52, p. 082001, jul 2012.
- [27] I. Duran, J. P. Gunn, R. Pánek, J. Adámek, J. Bucalossi, T. Loarer, and J. Pascal, “SOL Response to Supersonic Pulsed Gas Injection in Tore Supra,” vol. 27, no. July, pp. 2–5, 2003.
- [28] P. T. Lang, J. Neuhauser, J. Bucalossi, A. Chankin, D. P. Coster, R. Drube, R. Dux, G. Haas, L. D. Horton, S. Kalvin, G. Kocsis, M. Maraschek, V. Mertens, V. Rohde, V. Rozhansky, R. Schneider, I. Senichenkov, I. Veselova, and E. Wolfrum, “Impact of a pulsed supersonic deuterium gas jet on the ELM behaviour in ASDEX Upgrade,” *Plasma Phys. Control. Fusion*, vol. 47, no. 9, pp. 1495–1516, 2005.
- [29] W. W. Xiao, P. H. Diamond, W. C. Kim, L. H. Yao, S. W. Yoon, X. T. Ding, S. H. Hahn, J. Kim, M. Xu, C. Y. Chen, B. B. Feng, J. Cheng, W. L. Zhong, Z. B. Shi, M. Jiang, X. Y. Han, Y. U. Nam, W. H. Ko, S. G. Lee, J. G. Bak, J. W. Ahn, H. K. Kim, H. T. Kim, K. P. Kim, X. L. Zou, S. D. Song, J. I. Song, Y. W. Yu, T. Rhee, J. M. Kwon, X. L. Huang, D. L. Yu, K. D. Lee, S. I. Park, M. Jung, S. Zoletnik, M. Lampert, G. R. Tynan, Y. S. Bae, J. G. Kwak, L. W. Yan, X. R. Duan, Y. K. Oh, and J. Q. Dong, “ELM mitigation by supersonic molecular beam injection: KSTAR and HL-2A experiments and theory,” *Nucl. Fusion*, vol. 54, no. 2, 2014.
- [30] L. Nie, J. Cheng, Y. Huang, L. W. Yan, L. H. Yao, B. B. Feng, J. Q. Dong, M. Xu, K. J. Zhao, D. L. Yu, W. L. Zhong, J. M. Gao, C. C. Yuan, Z. H. Huang, D. F. Kong, Z. Feng, C. H. Liu, K. Yao, J. Shang, Q. W. Yang, X. T. Ding, and X. R. Duan, “Intermittent convective transport suppressed by supersonic molecular beam injection on the HL-2A tokamak,” *Plasma Phys. Control. Fusion*, vol. 56, no. 5, 2014.
- [31] X. Zheng, J. Li, J. Hu, J. Li, B. Cao, and J. Wu, “Comparison between gas puffing and supersonic molecular beam injection in plasma density feedback experiments in east,” *Plasma Physics and Controlled Fusion*, vol. 55, pp. 5010–, 11 2013.

- [32] Z. Wang, X. Xu, T. Xia, and T. Rognlien, “2d simulations of transport dynamics during tokamak fuelling by supersonic molecular beam injection,” *Nuclear Fusion*, vol. 54, p. 043019, mar 2014.
- [33] X. Wu, H. Li, Z. Wang, H. Feng, and Y. Zhou, “Simulations of the effects of density and temperature profile on SMBI penetration depth based on the HL-2A tokamak configuration,” *Chinese Phys. B*, vol. 26, no. 6, 2017.
- [34] Y. F. Shi, Z. H. Wang, Q. L. Ren, A. P. Sun, D. L. Yu, W. F. Guo, and M. Xu, “Simulations of fast component and slow component of SMBI on HL-2A tokamak,” *Chinese Phys. B*, vol. 26, no. 5, 2017.
- [35] D. Yu, C. Chen, L. Yao, B. Feng, X. Han, L. Yang, W. Zhong, Y. Zhou, K. Zhao, Y. Huang, Y. Liu, L. Yan, Q. Yang, J. Dong, and X. Duan, “Penetration characteristics of supersonic molecular beam injection on HL-2a tokamak,” *Nuclear Fusion*, vol. 50, p. 035009, mar 2010.
- [36] Y. L. Zhou, Z. H. Wang, X. Q. Xu, H. D. Li, H. Feng, and W. G. Sun, “Comparisons between tokamak fueling of gas puffing and supersonic molecular beam injection in 2D simulations,” *Phys. Plasmas*, vol. 22, no. 1, 2015.
- [37] Y. L. Zhou, Z. H. Wang, M. Xu, Q. Wang, L. Nie, H. Feng, and W. G. Sun, “Investigation of molecular penetration depth variation with SMBI fluxes,” *Chinese Phys. B*, vol. 25, no. 9, 2016.
- [38] V. Rozhansky, I. Senichenkov, I. Veselova, D. Morozov, and R. Schneider, “Penetration of supersonic gas jets into a tokamak,” *Nuclear Fusion*, vol. 46, pp. 367–382, jan 2006.
- [39] Y. Çengel and M. Boles, *Thermodynamics: An Engineering Approach*. No. v. 1 in McGraw-Hill series in mechanical engineering, McGraw-Hill, 2002.
- [40] H. Park, M. Choi, S. Hong, Y. In, Y. Jeon, J. Ko, W. Ko, J. Kwak, J. Kwon, J. Lee, J. Lee, W. Lee, Y. Nam, Y. Oh, B. Park, J. Park, Y. Park, S. Wang, M. Yoo, S. Yoon, J. Bak, C. Chang, W. Choe, Y. Chu, J. Chung, N. Eidiatis, H. Han, S. Hahn, H. Jhang, J. Juhn, J. Kim, K. Kim, A. Loarte, H. Lee, K. Lee, D. Mueller, Y. Na, Y. Nam, G. Park, K. Park, R. Pitts, S. Sabbagh, and G. Y. and, “Overview of KSTAR research progress and future plans toward ITER and k-DEMO,” *Nuclear Fusion*, vol. 59, p. 112020, jul 2019.
- [41] “Nfri - kstar project.” <https://www.nfri.re.kr/eng/pageView/103>.
- [42] NFRI, “Kstar diagnostics data user guide,” NFRI, National Fusion Research Institute, 2018.
- [43] W.Lee, “Mir analysis for 15841,” KSTAR, 2018.
- [44] W. Lee, J. A. Lee, S. H. Ko, D. J. Lee, J. M. Kwon, G. S. Yun, H. K. Park, and the KSTAR team, “Study of quasi-coherent modes (qcms) in kstar ech and ohmic plasmas,” 2th Asia-Pacific Conference on Plasma Physics, 2018.

- [45] J. A. Lee, W. Lee, J. M. Kwon, S. H. Ko, J. Leem, G. S. Yun, H. K. Park, Y. S. Park, K. W. Kim, N. C. Luhmann, and Kstar Team, “Observation of electron driven quasi-coherent modes and their connection with core intrinsic rotation in KSTAR ECH and ohmic L-mode plasmas,” *Physics of Plasmas*, vol. 25, p. 022513, Feb. 2018.
- [46] G. J. Radford, A. V. Chankin, G. Corrigan, R. Simonini, J. Spence, and A. Taroni, “The particle and heat drift fluxes and their implementation into the EDGE2D transport code,” *Contrib. Plasma Phys.*, vol. 36, pp. 187–191, 1996.
- [47] P. Tamain, P. Ghendrih, E. Tsitrone, V. Gradgirand, X. Garbet, Y. Sarazin, E. Serre, G. Ciraolo, and G. Chivassa, “TOKAM-3D: A 3D fluid code for transport and turbulence in the edge plasma of Tokamaks,” *Journal of computational physics*, vol. 229, pp. 361–378, 2010.
- [48] A. H. Nielsen, J. J. Rasmussen, J. Madsen, G. S. Xu, V. Naulin, J. M. B. Olsen, M. Løiten, S. K. Hansen, N. Yan, L. Tophøj, and B. N. Wan, “Numerical simulations of blobs with ion dynamics,” *Plasma Physics and Controlled Fusion*, vol. 59, p. 025012, dec 2016.
- [49] A. S. Thrysoe, M. Løiten, J. Madsen, V. Naulin, A. H. Nielsen, and J. J. Rasmussen, “Plasma particle sources due to interactions with neutrals in a turbulent scrape-off layer of a toroidally confined plasma,” *Physics of plasma*, vol. 25, no. 2, p. 025012, 2018.
- [50] F. L. Hinton and C. W. H. Jr., “Amplitude Limitation of a Collisional Drift Wave Instability,” *Physics of Fluids*, vol. 14, pp. 116–123, Jan. 1971.
- [51] O. E. Garcia, “Collective motions in non-uniformly magnetized plasmas,” *Eur. J. Phys.*, vol. 24, no. 4, pp. 331–339, 2003.
- [52] F. Militello, P. Tamain, F. W, K. A, V. Naulin, and A. H. Nielsen, “Experimental and numerical characterization of the turbulence in the scrape-off layer of mast,” *Plasma Physics and Controlled Fusion*, vol. 55, no. 2, p. 025005, 2013.
- [53] N. Yan, A. H. Nielsen, G. S. Xu, N. Volker, J. Juul Rasmussen, J. Madsen, H. Q. Wang, S. C. Liu, W. Zhang, L. Wang, and B. N. Wan, “Statistical characterization of turbulence in the boundary plasma of east,” *Plasma Physics and Controlled Fusion*, vol. 55, no. 11, p. 115007, 2013.
- [54] O. E. Garcia, R. A. Pitts, J. Horacek, A. H. Nielsen, W. Fundamenski, J. P. Graves, V. Naulin, and J. Juul Rasmussen, “Turbulent transport in the tcv sol,” *Journal of Nuclear Materials*, vol. 363-365, pp. 575–580, 2007.
- [55] J. Madsen, V. Naulin, A. H. Nielsen, and J. J. Rasmussen, “Collisional transport across the magnetic field in drift-fluid models,” *Physics of Plasmas*, vol. 23, no. 3, p. 032306, 2016.
- [56] B. D. Dudson, A. Allen, G. Breyiannis, E. Brugger, J. Buchanan, L. Easy, S. Farley, I. Joseph, M. Kim, A. D. McGann, and et al., “Bout: Recent and current developments,” *Journal of Plasma Physics*, vol. 81, no. 1, p. 365810104, 2015.

- [57] O. E. Garcia, V. Naulin, A. H. Nielsen, and J. Juul Rasmussen, “Turbulence and intermittent transport at the boundary of magnetized plasmas,” *Physics of Plasmas*, vol. 12, no. 6, p. 062309, 2005.
- [58] S. J. Zweben, B. D. Scott, J. L. Terry, B. LaBombard, J. W. Hughes, and D. P. Stotler, “Comparison of scrape-off layer turbulence in alcator c-mod with three dimensional gyrofluid computations,” *Physics of Plasmas*, vol. 16, 1 2009.
- [59] C. Wersal and P. Ricci, “Impact of neutral density fluctuations on gas puff imaging diagnostics,” *Nuclear Fusion*, vol. 57, p. 116018, aug 2017.
- [60] A. S. Thrysøe, *Influence of neutral particles on edge dynamics of magnetically confined plasmas*. PhD dissertation, Technical university of Denmark, 2018.
- [61] E. T. Meier and U. Shumlak, “A general nonlinear fluid model for reacting plasma-neutral mixtures,” *Physics of Plasmas*, vol. 19, p. 072508, 2012.
- [62] A. S. Thrysøe. Personal communication, 2019-10-03.
- [63] Y. Marandet, P. Tamain, R. Futterack, P. Ghendrih, H. Bufferand, P. Genesio, and A. Mekkaoui, “Influence of neutral particles on scrape-off layer turbulence with application to the interpretation of fast camera data,” *Journal of Nuclear Materials*, vol. 438, pp. S518 – S521, 2013. Proceedings of the 20th International Conference on Plasma-Surface Interactions in Controlled Fusion Devices.
- [64] M. B. Sumer, *Lecture notes on Turbulence*. Technical University of Denmark, 2013.
- [65] O. E. Garcia, V. Naulin, A. H. Nielsen, and J. J. Rasmussen, “Turbulence simulations of blob formation and radial propagation in toroidally magnetized plasmas,” *Physica Scripta*, vol. T122, pp. 89–103, jan 2006.
- [66] B. Labit, I. Furno, A. Fasoli, A. Diallo, S. Müller, G. Plyushchev, M. Podestà, and F. Poli, “Universal statistical properties of drift-interchange turbulence in torpex plasmas,” *Physical review letters*, vol. 98, p. 255002, 07 2007.
- [67] M. Lampert, *Characterizing edge-plasma turbulence on the KSTAR tokamak with beam emission spectroscopy*. PhD dissertation, Wigner research center for physics, 2018.
- [68] A. S. Thrysøe, L. E. H. Tophj, V. Naulin, J. J. Rasmussen, J. Madsen, and A. H. Nielsen, “The influence of blobs on neutral particles in the scrape-off layer,” *Plasma Physics and Controlled Fusion*, vol. 58, no. 4, p. 044010, 2016.
- [69] A. Mekkaoui, Y. Marandet, D. Reiter, P. Genesio, J. Rosato, H. Capes, F. Catoire, L. Godbert-Mouret, M. Koubiti, and R. Stamm, “Transport of neutrals in turbulent scrape-off-layer plasmas,” *Journal of Nuclear Materials*, vol. 415, 08 2011.
- [70] D. Fan, Y. Marandet, P. Tamain, H. Bufferand, G. Cirakolo, P. Ghendrih, and E. Serre, “Effect of turbulent fluctuations on neutral particles transport with the tokam3x-eirene turbulence code,” *Nuclear Materials and Energy*, vol. 18, pp. 105 – 110, 2019.